UNIVERSITY OF CALIFORNIA,
IRVINE

Constraining Dark Matter Physics with Cosmological Simulations

DISSERTATION

submitted in partial satisfaction of the requirements
for the degree of

DOCTOR OF PHILOSOPHY

in Physics

by

Oliver D. Elbert

Dissertation Committee:
Professor James S. Bullock, Chair
Professor Manoj Kaplinghat
Professor Michael Cooper

2017

DEDICATION

To my Grandmother, who first turned my eyes to the stars.

TABLE OF CONTENTS

LIST OF FIGURES

LIST OF TABLES

ACKNOWLEDGMENTS

None of the work in this thesis would have been possible without the help and support of a small army of people. I owe a special thanks to the following.

First, to my advisor James Bullock, thank you for all of your help, encouragement and inspiration. Your passion for astronomy is infectious, and the care you take over your research group is amazing. There were many times I was sure I could never succeed in science, and each time your reassurance and perspective gave me the confidence I needed.

I would like to thank my thesis committee, Manoj Kaplinghat and Michael Cooper, both for their work on my committee and for the amazing collaboration, discussion and teaching they've given me in my time at UCI.

The love and support of my family and friends has been invaluable. To my wife, Amalya, your patience and encouragement have been absolutely incredible, and I'm so lucky to have you as my partner and teammate.

Of course, I would have gotten nowhere without the help of my collaborators, especially Jose Onorbe, Andrew Graus, Mike Boylan-Kolchin, Victor Rocha, Alejandro Gonzalez-Samaniego, Alex Fitts, and Annika Peter. I owe a special thanks to Miguel Rocha, Shea Garrison-Kimmel, and Coral Wheeler, who taught me how to simulate, do research, and enjoy my time at UCI

I owe a tremendous debt to Haverford College, and its Physics and Astronomy department. In particular Beth Willman, for introducing me to simulations not accepting less than full effort and pushing me throughout college to be the best scientist I could. Your belief in me and insistence that I do more than coast through Steve Boughn, whose freshman seminar in astrophysics caused me to fall in love with the subject and pursue it beyond college. The approach and ideas of that class underlie much of the work in chapter 4.

The text of this thesis is a reprint of the material as it appears in Monthly Notices of the Royal Astronomical Society. The co-authors listed in this publication directed and supervised research which forms the basis for the thesis.

This work was made possible by the financial support of the National Science Foundation (grants PHY-1520921, AST-1518291, and AST-1009973) and by NASA through Hubble Space Telescope grants HST-GO-12966.003-A and HST-GO-13343.009-A, awarded by the Space Telescope Science Institute (STScI), which is operated by the Association of Universities for Research in Astronomy (AURA), Inc., under NASA contract NAS5-26555. This work used the Extreme Science and Engineering Discovery Environment (XSEDE), which is supported by National Science Foundation grant number ACI-1053575.

CURRICULUM VITAE

Oliver D. Elbert

EDUCATION

Doctor of Philosophy in Physics **2017**
University of California, Irvine *Irvine, California*

Master of Science in Physics **2017**
University of California, Irvine *Irvine, California*

Bachelor of Science in Astrophysics **2011**
Haverford College *Haverford, Pennsylvania*

RESEARCH EXPERIENCE

Graduate Research Assistant **2011–2017**
University of California, Irvine *Irvine, California*

RESEARCH INTERESTS

Galaxy evolution and theoretical Cosmology

- Numerical simulations of galaxy formation and evolution
- Constraining the particle nature of dark matter
- The reionization history of the universe and its impact on dwarf and ultra-faint galaxies
- AGN feedback and substructure in galaxy clusters
- The diversity of low-surface-brightness galaxy sizes
- Using gravitational wave detections to study star and galaxy formation

TEACHING EXPERIENCE

Teaching Assistant **2011–2015**
University of California, Irvine *Irvine, California*

Math Clinic Tutor **2010**
Haverford College *Haverford, Pennsylvania*

PUBLICATIONS

1. **Elbert, Oliver D.**; Bullock, James S.; Garrison-Kimmel, Shea; Rocha, Miguel; Oñorbe, Jose; Peter, Annika H. G.
   Core formation in dwarf haloes with self-interacting dark matter: no fine-tuning necessary
   MNRAS 453 p. 29-37

2. **Elbert, Oliver D.**; Bullock, James S.; Kaplinghat, Manoj; Garrison-Kimmel, Shea; Graus, Andrew S.; Rocha, Miguel
   A Testable Conspiracy: Simulating Baryonic Effects on Self-Interacting Dark Matter Halos
   Submitted to *ApJ*, arXiv:1609.08626

3. **Elbert, Oliver D.**; Bullock, James S.; Kaplinghat, Manoj
   Counting Black Holes: The Cosmic Stellar Remnant Population and Implications for LIGO
   Submited to *MNRAS*, arXiv: 1703.02551

4. Wheeler, Coral; Oñorbe, Jose; Bullock, James S.; Boylan-Kolchin, Mike; **Elbert, Oliver D.**; Garrison-Kimmel, Shea; Hopkins, Philip F.; Kereš, Dušan
   Sweating the small stuff: simulating dwarf galaxies, ultra-faint dwarf galaxies, and their own tiny satellites
   MNRAS, 453 p.1305-1316

5. Wheeler, Coral; Pace, Andrew B.; Bullock, James S.; Boylan-Kolchin, Mike; Oñorbe, Jose; **Elbert, Oliver D.**; Fitts, Alex; Hopkins, Philip F.; Kereš, Dušan
   The no-spin zone: rotation vs dispersion support in observed and simulated dwarf galaxies
   MNRAS 465 p. 2420-2431

6. Fitts, Alex; Boylan-Kolchin, Mike; **Elbert, Oliver D.**; Bullock, James S.; Hopkins, Philip F.; Oñorbe, Jose; Wetzel, Andrew R.; Wheeler, Coral; Faucher-Giguère, Claude-André; Kereš, Dušan; Quataert, Eliot; Skillman, Evan D.; Weisz, Daniel R.
   `FIRE` in the Field: Simulating the Threshold of Galaxy Formation
   Submitted to *MNRAS*, arXiv:1611.02281

7. Hopkins, Philip F.; Wetzel, Andrew R.; Kereš, Dušan; Faucher-Giguère, Claude-André; Quataert, Eliot; Boylan-Kolchin, Mike; Murray, Norman; Hayward, Christopher C.; Garrison-Kimmel, Shea; Hummels, Cameron; Feldmann, Robert; Torrey, Paul; Ma, Xiangcheng; Anglés-Alcázar, Daniel; Su, Kung-Yi; Orr, Matthew; Schmitz, Denise; Escala, Ivanna; Sanderson, Robyn; Grudić, Michael Y.; Hafen, Zachary; Kim, Ji-Hoon; Fitts, Alex; Bullock, James S.; Wheeler, Coral; Chan, T.K.; **Elbert, Oliver D.**; Narayanan, Desika
   `FIRE`-2 Simulations: Physics versus Numerics in Galaxy Formation Submitted to *MNRAS*, arXiv:1702.06148

8. González-Samaniego, Alejandro; Bullock, James S.; Boylan-Kolchin, Michael; Fitts, Alex; **Elbert, Oliver D.**; Hopkins, Philip F.; Kereš, Dušan; Faucher-Giguère, Claude-André
FIRE-2 Simulations: Physics versus Numerics in Galaxy Formation Submitted to *MNRAS*, arXiv:1706.05383

9. Robles, Victor H.; Bullock, James S.; **Elbert, Oliver D.**; Fitts, Alex; González-Samaniego, Alejandro; Boylan-Kolchin, Michael; Hopkins, Philip F.; Faucher-Giguère, Claude-André; Kereš, Dušan; Hayward, Christopher C.
on textttFIRE: Hydrodynamical Self-Interacting Dark Matter simulations of low-mass dwarf galaxies Submitted to *MNRAS*, arXiv:1706.07514

ABSTRACT OF THE DISSERTATION

Constraining Dark Matter Physics with Cosmological Simulations

By

Oliver D. Elbert

Doctor of Philosophy in Physics

University of California, Irvine, 2017

Professor James S. Bullock, Chair

Dark Matter (DM) accounts for the vast majority of mass in the universe, but the particle identity of dark matter remains a mystery. Uncovering the fundamental nature of DM remains one of the greatest challenges facing modern physics. Because the only information about DM comes from astrophysical observations, these are the best sources to constrain models. Dwarf galaxies present an especially tantalizing regime to investigate dark physics, as they have the highest ratio of dark to luminous matter and therefore will be most affected by differences between DM models. Additionally, this is precisely the scale where generic dark matter theories have the most difficulty reproducing astronomical observations, leading to the missing satellites, core-cusp and too-big-to-fail (TBTF) problems.

A particular class of models with nuclear scale self-interactions (called SIDM) has emerged as a promising candidate. SIDM naturally forms cored halos, which may alleviate both the core-cusp and TBTF problems. However, at larger scales the the interplay between SIDM halos and the galaxies residing in them is poorly understood, complicating this picture greatly. In this thesis I present numerical simulations of SIDM and CDM halos investigating these issues. I show that at dwarf scales SIDM cross sections as small as 0.5 $\mathrm{cm}^2\ \mathrm{g}^{-1}$ solve the TBTF and core-cusp problems, and that cross sections 2 orders of magnitude larger are not ruled out. I have also embedded gravitational potentials that approximate realistic galaxies

in simulations of larger haloes in order to test the impact of galaxy formation on SIDM halos. These simulations show that SIDM is indistinguishable from CDM in systems where the galaxy dominates the central region, but in galaxies with higher mass-to-light ratios or less centrally concentrated baryons it is possible to constrain SIDM cross sections. In the galaxy cluster regime I show that an SIDM cross section of $0.1 - 0.2$ cm^2 g^{-1} is preferred to CDM or other SIDM cross sections.

Chapter 1

Introduction

The standard cosmological paradigm holds that the Universe is dominated by a cosmological constant Λ (dark energy), and Dark Matter (DM), with luminous matter accounting for roughly 6% of the global energy density (Hinshaw et al., 2013; Planck Collaboration et al., 2015). Microsensing studies have shown that the DM cannot be large compact objects such as black holes or Jupiter-like planets (Tisserand et al., 2007; Mediavilla et al., 2017), implying that it is instead comprised of some new particle. In this ΛCDM model DM particles clump into gravitationally bound haloes, which then host galaxies as they form and grow (White & Rees, 1978). Unfortunately, while there have been tantalizing hints about the fundamental nature of dark matter (Boyarsky et al., 2014; Bulbul et al., 2014; Ackermann et al., 2017), we still do not know what it truly is.

Even without this detail, however, the ΛCDM paradigm has been remarkably successful in predicting the large-scale properties of galaxy populations such as their distribution (Springel et al., 2006, see e.g.). However, at smaller scales discrepancies have emerged that challenge this model. Two issues are the Core-Cusp and Too Big to Fail (TBTF) problems. Simulations of dark matter haloes have found that halo densities follow a characteristic radial profile

(Navarro et al., 1997), with a cuspy, $\rho \propto r^{-1}$ center. Observations of dwarf galaxies, on the other hand show a tendency for them to have flat central density profiles instead of the r^{-1} cusps (Flores & Primack, 1994; Kuzio de Naray et al., 2008; Oh et al., 2008; Walker & Peñarrubia, 2011), forming the Core-Cusp problem. Related to this is the fact that the central masses of observed dwarf spheroidal galaxies are well below those predicted for the 10^{10} $M\odot$ haloes expected to host these systems (Boylan-Kolchin et al., 2011, 2012). If the local dwarf spheroidals are in fact hosted by smaller dark matter haloes then there is no that the 10^{10} $M\odot$ haloes expected to be prevalent in the local Universe host any galaxies, hence the TBTF name. If, however, the DM haloes had cored density profiles, the reduced inner halo mass would explain TBTF. Feedback from baryonic processes such as supernovae and gamma-ray heating can in principle solve these issues by forming central cores, (Pontzen & Governato, 2012; Di Cintio et al., 2014; Oñorbe et al., 2015), but it is unclear if enough stars form in these systems to successfully create cores (Garrison-Kimmel et al., 2013; Fitts et al., 2016).

An intriguing resolution to these problems is to allow DM particles to scatter off of each other with cross sections similar to the strong nuclear force. First explored astrophysically by Spergel & Steinhardt (2000), such Self-Interacting DM (SIDM) models form isothermal central cores through energy exchange, independent of star formation. Early work found that SIDM cross sections of order $\sigma/m \sim 1$ cm^2 g^{-1} naturally produced haloes with sizeable cores (Burkert, 2000; Davé et al., 2001; Colín et al., 2002), though these cross sections were ruled in tension with observations at cluster scales (Yoshida et al., 2000; Gnedin & Ostriker, 2001; Miralda-Escudé, 2002, see e.g.). Recent work, however, has revised these limits back to the 1 cm^2 g^{-1} range (Peter et al., 2013; Massey et al., 2015; Kim et al., 2016), and SIDM models with a velocity-dependent cross section have come into favor (Feng et al., 2009; Loeb & Weiner, 2011; Tulin et al., 2013b; Vogelsberger et al., 2012, e.g.), allowing independent constraints to be placed at different halo mass scales. In principle it is completely possible for DM particles to have scattering cross sections of 5 cm^2 g^{-1} at dwarf galaxy scales but for

σ/m to be over an order of magnitude smaller in clusters. While this makes SIDM models more viable when compared to observations, it also makes it more difficult to constrain an actual dark matter scattering cross section.

A separate form of dark matter, meanwhile has led to a revolution in astronomy over the past year. The detection of gravitational waves from merging black hole binary systems (Abbott et al., 2016d,c, 2017) has both strikingly confirmed a fundamental prediction of General Relativity (Einstein, 1916) and hinted at a much larger-than-expected population of massive stellar remnant black holes. Work is ongoing to identify likely host galaxies for these binary black hole (BBH) mergers (Lamberts et al., 2016; Belczynski et al., 2016a; Chatterjee et al., 2017) and possible physical processes to facilitate these mergers (VanLandingham et al., 2016; Kimpson et al., 2016), but understanding the population of these remnants of massive stars could give insights into star formation and galaxy evolution as well. Gravitational wave astrophysics is a brand-new, wide open field with many questions to ask.

This work addresses some of the current gaps in our understanding of DM physics and black hole populations. It is organized as follows. In Chapter 2 we use high resolution simulations of dwarf galaxy haloes in CDM and multiple SIDM cross sections to explore the viability of SIDM models as solutions to the TBTF and Core-cusp problems. Chapter 3 presents a set of dark matter-only simulations with an additional gravitational potential included to represent the central galaxies hosted by these halos. We explore the effects of adiabatic contraction on our SIDM haloes in comparison to the CDM case and use this to constrain SIDM cross sections on galaxy cluster scales. In Chapter 4 we combine the results of modern stellar evolution codes with X to analytically calculate the number and distribution of compact stellar remnants in the Universe, with a particular focus on massive black holes. We then present a simple model to use current merger rate observations from LIGO to constrain binary black hole merger properties. We summarize and conclude in Chapter 5.

Chapter 2

Dwarf halo cores with SIDM

2.1 Chapter Abstract

We investigate the effect of self-interacting dark matter (SIDM) on the density profiles of $V_{\rm max} \simeq 40$ km s^{-1} isolated dwarf dark matter haloes – the scale of relevance for the too big to fail problem (TBTF) – using very high resolution cosmological zoom simulations. Each halo has millions of particles within its virial radius. We find that SIDM models with cross-sections per unit mass spanning the range $\sigma/m = 0.5 - 50$ cm^2 g^{-1} alleviate TBTF and produce constant-density cores of size $300 - 1000$ pc, comparable to the half-light radii of $M_\star \sim 10^{5-7} M\odot$ dwarfs. The largest, lowest density cores develop for cross-sections in the middle of this range, $\sigma/m \sim 5 - 10$ cm^2 g^{-1}. Our largest SIDM cross-section run ($\sigma/m = 50$ cm^2 g^{-1}) develops a slightly denser core owing to mild core-collapse behaviour, but it remains less dense than the cold dark matter case and retains a constant-density core profile. Our work suggests that SIDM cross-sections as large or larger than 50 cm^2 g^{-1} remain viable on velocity scales of dwarf galaxies ($v_{\rm rms} \sim 40$ km s^{-1}). The range of SIDM cross-sections that alleviate TBTF and the cusp/core problem spans at least two orders of

magnitude and therefore need not be particularly fine-tuned.

2.2 Introduction

Cosmological studies of the large-scale universe have provided tremendous evidence in favour of a Universe dominated by dark matter (DM) and dark energy (e.g. Komatsu et al., 2011; Hinshaw et al., 2013; Planck Collaboration et al., 2014), but thus far very little is known about the underlying nature of the DM particle other than that it is long-lived and that it interacts weakly with the standard model. For thermal particles, the DM needs to be fairly massive (or 'cold' – non-relativistic at decoupling) in order to produce a power spectrum consistent with large-scale structure (Reid et al., 2010). Weakly interacting massive particles (WIMPs), for example, provide a compelling and well-motivated class of cold dark matter (CDM) candidates (Steigman & Turner, 1985; Griest, 1988; Jungman et al., 1996). On the scales of concern for galaxy formation, WIMPs behave as collisionless particles and are one of the prime motivations for what has become the standard paradigm for structure formation: collisionless CDM.

There are, however, disagreements between predictions from CDM-only simulations and observations on small scales. For example, some galaxies appear to have flat central density profiles (e.g. Flores & Primack, 1994; Kuzio de Naray et al., 2008; Amorisco et al., 2014; Oh et al., 2008; Walker & Peñarrubia, 2011; Salucci & Burkert, 2000; Gentile et al., 2004, but also see Strigari et al., 2014) with core-like log-slopes ($\alpha \sim 0$) rather than the predicted cusps ($\alpha \sim 1$) seen in CDM simulations (Dubinski & Carlberg, 1991; Navarro et al., 1997). This issue is known as the cusp/core problem. A qualitatively similar anomaly was pointed out by Boylan-Kolchin et al. (2011, 2012), who showed that observations of the dwarf spheroidal (dSph) satellites of the Milky Way (MW) imply central masses well below those of the $V_{\rm max} = 40$ km s^{-1} haloes that appear to be common in ultrahigh resolution simulations of

MW-size hosts (e.g. Diemand et al., 2008; Springel et al., 2008). This issue is known as the 'too big to fail' problem (TBTF). Tollerud et al. (2014) and Garrison-Kimmel et al. (2014b) further showed that the Andromeda (M31) dSph satellites and the field galaxies near the MW and M31, respectively, suffer from the same problem. Studies of larger samples of dwarf galaxies in the field also indicate a similar density problem at a comparable velocity scale $V_{\rm max} \simeq 40$ km s^{-1} (Ferrero et al., 2012; Klypin et al., 2014; Papastergis et al., 2014).

One natural solution to TBTF and other central-density issues is to posit that galaxy haloes have lower core densities than predicted in CDM-only simulations. For example, baryonic processes may act to reduce and flatten the central densities of small galaxies in CDM (e.g. Navarro et al., 1996; Governato et al., 2012; Pontzen & Governato, 2012; Di Cintio et al., 2014). In contrast, Peñarrubia et al. (2012) and Garrison-Kimmel et al. (2013) have argued that the $M_\star \sim 10^6 M\odot$ galaxies of interest for TBTF have not had enough supernovae to alter densities sufficiently (though see Gritschneder & Lin, 2013; Amorisco et al., 2014). Others have suggested environmental effects may increase the efficacy of these internal processes by similarly reducing the central masses of subhaloes (e.g. Zolotov et al., 2012; Del Popolo, 2012; Arraki et al., 2014; Brooks & Zolotov, 2014; Del Popolo et al., 2014). However, these external processes are weak or non-existent in the field, suggesting that non-baryonic solutions may be necessary to solve the discrepancy observed outside the MW and M31 (Garrison-Kimmel et al., 2014b; Papastergis et al., 2014). Similarly, while large TBTF subhaloes become increasingly infrequent as the mass of the MW and M31 host haloes decrease (Purcell & Zentner, 2012; Wang et al., 2012; Rodríguez-Puebla et al., 2013; Cautun et al., 2014), solutions of this kind appear less likely in the face of evidence that TBTF is persistent in the field (Ferrero et al., 2012; Klypin et al., 2014; Garrison-Kimmel et al., 2014b).

Alternatively, the central density issues may be telling us something about cosmology. For example, if the primordial power spectrum is non-standard (Zentner & Bullock, 2002; Polisensky & Ricotti, 2014; Garrison-Kimmel et al., 2014c) or the DM is warm rather than cold (An-

derhalden et al., 2013; Lovell et al., 2014; Horiuchi et al., 2014) then the central densities of DM haloes would decrease. However, neither of these possibilities produce constant-density cores on observable scales; they simply lower the normalization while retaining cuspy slopes.

The focus of this paper is to explore an alternative possibility: that the CDM particles are strongly self-interacting.[1] First discussed in an astrophysical context by Spergel & Steinhardt (2000), self-interacting dark matter (SIDM) with energy-exchange cross-sections per unit mass on the order of $\sigma/m \sim 1$ cm^2 g^{-1} can naturally produce constant-density cores in the hearts of DM haloes on the scales of relevance for galaxy rotation curves and TBTF (Burkert, 2000; Davé et al., 2001; Feng et al., 2009; Vogelsberger et al., 2012; Rocha et al., 2013). Constant-density isothermal cores in SIDM haloes come about because kinetic energy can be transmitted from the hot outer halo inwards (see, e.g., the discussion in Rocha et al., 2013). This effect can only occur if σ/m is large enough for there to be a relatively high probability of scattering over a time $t_{\rm age}$ comparable to the age of the halo: $\Gamma \times t_{\rm age} \sim 1$, where $\Gamma \simeq \rho_{\rm dm}(\sigma/m)v_{\rm rms}$ is the interaction rate, $\rho_{\rm dm}$ is the local DM density and $v_{\rm rms}$ is the rms speed of DM particles. If the cross-section is too large, however, then the high probability of interaction can potentially lead to a negative heat flux, where energy is transmitted from the inside out (Kochanek & White, 2000), leading to a 'core collapse' phenomena, not unlike core collapse in globular clusters, where the central halo density increases to the point that it exacerbates the overdensity problem on small scales. The specific range of cross-sections that are (a) small enough to be observationally allowed, (b) large enough to alleviate the relevant small-scale problems, and (c) small enough to avoid catastrophic core collapse, are all topics of this exploration.

In most particle-physics based models for SIDM, the scattering interactions have a velocity dependence (e.g., Blinnikov & Khlopov, 1983; Feng et al., 2009, 2010b; Khlopov et al., 2010; Loeb & Weiner, 2011; Tulin et al., 2013a; Kaplinghat et al., 2014b; Boddy et al., 2014b,a).

[1] SIDM models with primordial power spectra that deviate from CDM on small scales have been explored by Buckley et al. (2014) but we focus on CDM-type power spectra here.

Astrophysical constraints, on the other hand, tend to rely on specific classes of objects that have a characteristic $v_{\rm rms}$ scale, meaning that they constrain $\sigma(v)/m$ at a specific value of $v \simeq v_{\rm rms}$. The best published limits ($\sigma/m \lesssim 1$ cm^2 g^{-1}) come from galaxy clusters with characteristic rms velocities $v_{\rm rms} \simeq 1000\,{\rm km\ s^{-1}}$ (Yoshida et al., 2000; Gnedin & Ostriker, 2001; Randall et al., 2008; Rocha et al., 2013; Peter et al., 2013). At the same time, the most compelling astrophysical *motivations* for exploring SIDM in the first place occur on the scales of dwarf galaxies where $v_{\rm rms} \simeq 10 - 100\,{\rm km\ s^{-1}}$. These differences in velocity scale are significant. For example, the SIDM cross-section could vary as $\sigma/m \propto v^{-4}$ if the interaction were a dark version of Rutherford scattering, with a massless force carrier (Tulin et al., 2013b). Thus it is not outlandish to consider the possibility that DM self-interactions on the scale of dwarf galaxies are *four orders of magnitude larger* than they are on the scale of galaxy clusters. Clearly we have significant need to derive constraints on as many velocity scales as possible.

The potential for significant velocity scaling in the SIDM energy-exchange cross-section has motivated Vogelsberger et al. (2012) and Zavala et al. (2013) to explicitly run zoom simulations of MW-size hosts using SIDM with velocity-dependent σ/m values tuned to evade bounds on cluster scales and to have large values (~ 10 cm^2 g^{-1}) on the scale of problematic TBTF haloes ($v_{\rm rms} \simeq V_{\rm max} \simeq 40\,{\rm km\ s^{-1}}$). They show that TBTF is resolved for $\sigma/m \simeq$ 1-10 cm^2 g^{-1} on the velocity scale of dwarfs. We note that fig. 8 of Vogelsberger et al. (2012) makes clear that a run with $\sigma/m = 10$ cm^2 g^{-1} provides a particularly good match to the spread in dwarf satellite central densities seen around the MW.

The goal of this paper is to explore more fully a range of cross-sections at the dwarf scales of interest, focusing specifically on isolated haloes rather than subhaloes in order to achieve very high resolution. We run a set of ultrahigh resolution cosmological simulations of isolated dwarf haloes with $v_{\rm rms} \simeq 40\,{\rm km\ s^{-1}}$ using SIDM cross-sections $\sigma/m = 0.1$ – 50 cm^2 g^{-1} in addition to collisionless CDM. The aim is to quantify the range of cross-sections that can

Name	$M_{\rm v}$ ($10^{10} M\odot$)	$R_{\rm v}$ (kpc)	$V_{\rm max}$ (km s^{-1})	$N_{\rm p}(R_{\rm v})$ (10^6)	σ/m (cm^2 g^{-1})
Pippin	0.9	55	37	4.1	$0, 0.1, 0.5,$ $5, 10, 50$
Merry	1.2	59	38	5.4	$0, 0.5, 1, 10$

Table 2.1: Summary of simulated haloes. The first four columns list identifying names and virial-scale properties (virial mass, virial radius, and maximum circular velocity). The fifth column gives number of particles within the virial radius for the high-resolution runs and the last column summarizes the cross-sections each halo was simulated with. The virial-scale properties of the haloes listed are for the CDM cases ($\sigma/m = 0$) but each of these values remains unchanged (within $\sim 5\%$) for all SIDM runs. $M_{\rm v}$ and $R_{\rm v}$ are calculated using the Bryan & Norman (1998) definition of $\rho_{\rm V}$.

alleviate TBTF (in the field) and are expected to produce observable cores in small dwarf galaxies. We also investigate whether a certain range of cross-sections can be ruled out because they would result in catastrophic core collapse.

This work is organized as followed. In §2.3, we describe the simulations and analysis pipeline. We present our results in §2.4, focusing first on the impact of varying σ/m on the density profiles in §2.4.1 and then on the implications for TBTF in §2.4.2. We summarize our results and conclude in §2.5.

2.3 Simulations

As we demonstrate explicitly below, in order to resolve the relevant $\sim 300 - 1000$ pc scales of classical dSph galaxies, very high force and mass resolution are required. We achieve this resolution in cosmological simulations using the zoom technique (Katz & White, 1993; Oñorbe et al., 2014). Our SIDM implementation follows that described in Rocha et al. (2013), using a modified version of `GADGET-2` (Springel, 2005). Halos were identified with the six-dimensional phase-space halo finder `ROCKSTAR` (Behroozi et al., 2013b).

We chose two haloes for our primary simulations using parent cosmological volumes of 7 Mpc

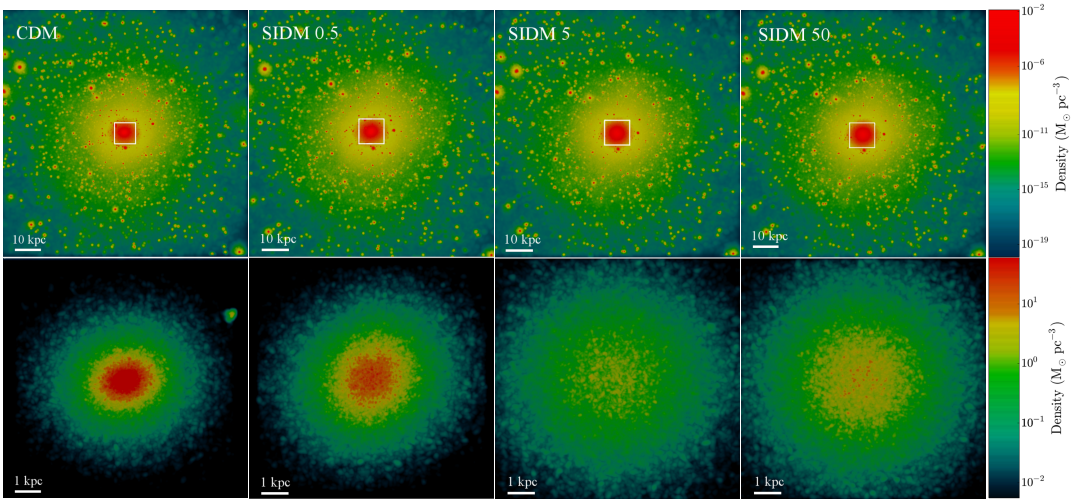

Figure 2.1: DM density of Pippin in CDM (left) and SIDM with σ/m increasing from left to right: 0.5, 5 and 50 cm^2 g^{-1}. Boxes on the top span 100 kpc ($R_{\rm v}$ = 55kpc) and the bottom panel zooms in to span a central 10 kpc box (with modified colour bar). Note that the global properties of the haloes on the scale of the virial radius, including the number and locations of subhaloes, are nearly identical across all runs. The only difference is that the inner core regions become less dense and somewhat puffed out in the SIDM cases. Note that the 50 cm^2 g^{-1} simulation is somewhat denser in the inner core than the 5 cm^2 g^{-1} case; it is undergoing mild core collapse.

on a side. Initial conditions were generated with `MUSIC` (Hahn & Abel, 2011) at $z = 125$ using cosmological parameters derived from the *Wilkinson Microwave Anisotropy Probe*-7 year data (Komatsu et al., 2011): $h = 0.71$, $\Omega_{\rm m} = 0.266$, $\Omega_\Lambda = 0.734$, $n_{\rm s} = 0.963$ and $\sigma_8 = 0.801$. Their global properties are given in Table 2.1. We refer to the slightly smaller of the two dwarfs ($V_{\rm max}$ = 37 km s^{-1}) as Pippin and the larger ($V_{\rm max}$ = 38 km s^{-1}) as Merry. Our high-resolution runs, which we analyse throughout, have particle mass $m_{\rm p} = 1.5 \times 10^3\ M\odot$ and a Plummer equivalent force softening $\epsilon = 28$ pc. We have also checked that various basic parameters of our target haloes (spins, concentrations and formation times) are within one standard deviation of what is expected for dwarf haloes based on a larger simulation box of 35 Mpc on a side (described in Oñorbe et al., 2014).

In addition to $\sigma/m = 0$ (collisionless CDM) runs, we simulate both haloes with $\sigma/m = 0.5, 1, 10$ cm^2 g^{-1}. Additionally we have simulated Pippin with $\sigma/m = 0.1, 5, 50$ cm^2 g^{-1}. In

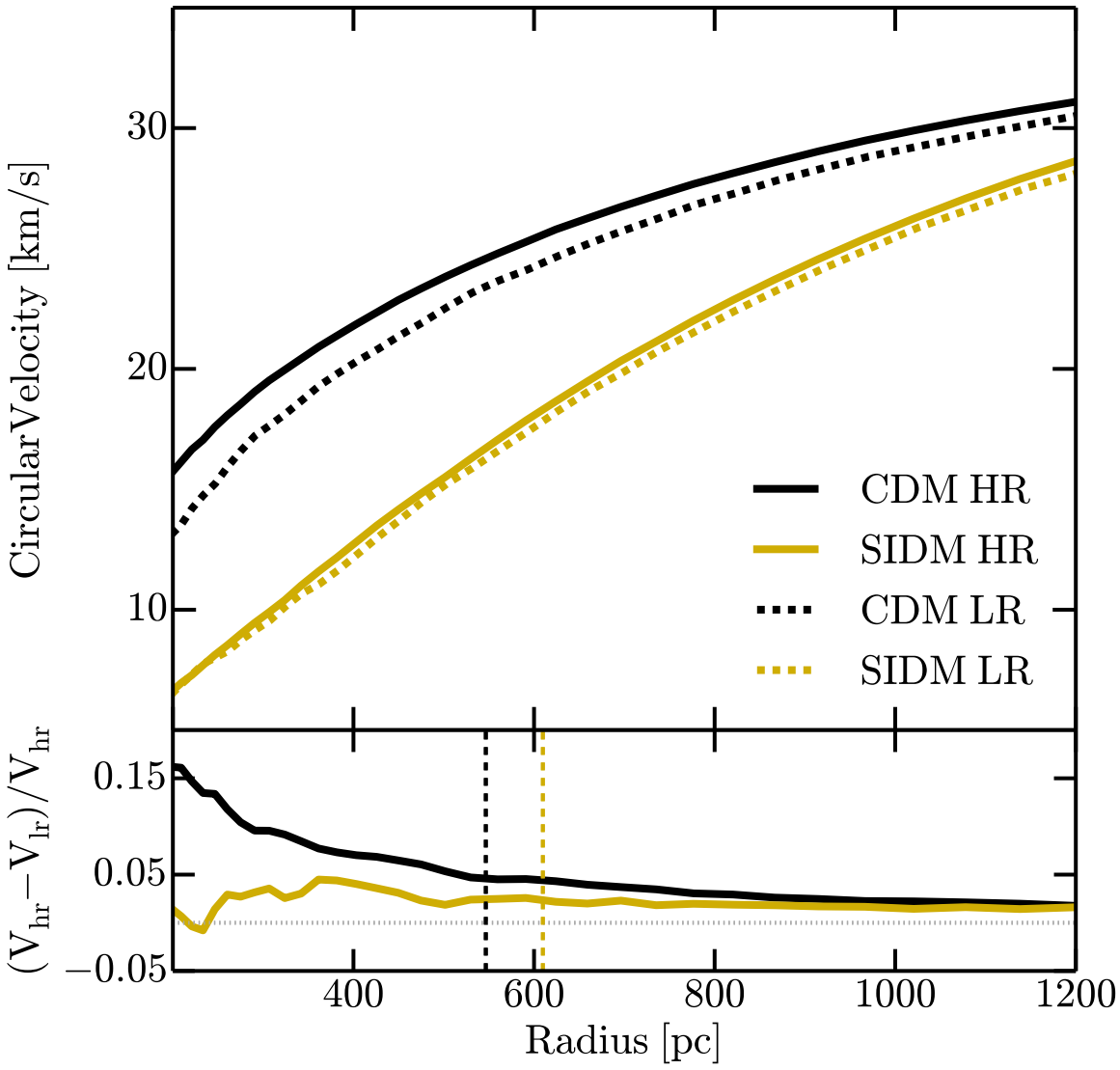

Figure 2.2: Top: circular velocity profiles of Pippin at our fiducial resolution (solid; $m_p = 1.5 \times 10^3\ M\odot$, $\epsilon = 28$ pc) and at low resolution (dotted; $m_p = 1.2 \times 10^4\ M\odot$, $\epsilon = 84$ pc) for both CDM (black) and SIDM (1 cm^2 g^{-1}, yellow). Bottom: the relative difference between high- and low-resolution circular velocity profiles. The dashed vertical lines indicate the Power et al. (2003) radius for the low-resolution haloes. Note that the SIDM haloes are much better converged than the CDM simulations.

all SIDM simulations, the DM self-interactions were calculated using an SIDM smoothing length equal to 0.25ϵ, as described in Rocha et al. (2013).

Fig. 2.1 shows visualizations of Pippin at high resolution, coloured by the local DM density, with collisionless CDM on the far left and SIDM runs of increasing cross-section to the right. The upper panels visualize a box 100 kpc across ($\sim 2R_{\rm v}$) and the lower panels zoom in on the central 10 kpc of the haloes, using a colour bar that has been rescaled to emphasize the highest densities. As these visualizations emphasize, bulk halo properties on the scale of $R_{\rm v}$ are virtually identical in CDM and SIDM; even the locations of subhaloes remain unchanged. The fact that substructure remains very similar in both SIDM and CDM is consistent with the findings of Vogelsberger & Zavala (2013) and Rocha et al. (2013); here, however, we examine mass scales well below those resolved in any previous SIDM study, resolving substructure as small as $V_{\rm max} = 1$ km s^{-1}. The main differences are apparent in the core regions (lower panels), where the SIDM runs are systematically less dense than CDM. Note that the 50 cm^2 g^{-1} run is actually denser in its core than the 5 cm^2 g^{-1} run. As discussed below, this is a result of core collapse.

2.3.1 Resolution Tests

We have designed our high-resolution simulations explicitly to recover the density structure at the ~ 300 pc half-light radius scale of low-mass dwarfs based on the work of Power et al. (2003) for CDM simulations. Power et al. (2003) showed that the differential density profiles of CDM haloes should be converged only outside of a specific radius where the gravitational two-body relaxation time approximates the Hubble time. While this work is perfectly well-designed for CDM runs, the issue of convergence in SIDM is less well explored. In order to remedy this concern, we have simulated Pippin in CDM and SIDM (1 cm^2 g^{-1}) at lower resolution, with eight times worse mass resolution ($m_{\rm p} = 1.2 \times 10^4\ M\odot$) and with greater

force softening ($\epsilon = 84$ pc) than our high-resolution runs. As expected, we confirm that the differential density profile of the CDM halo is convergent down to the classic Power et al. (2003) radius of the low-resolution runs (168 pc for Pippin, 160 pc for Merry); reassuringly, the SIDM run is even more stable. We find convergence in the density profile down to below half the Power radius (see also Vogelsberger et al., 2012, who found similar robustness for SIDM haloes). This is qualitatively reasonable in the limit where physical self-interactions are more important than artificial two-body interactions.

While the differential density is the most natural theoretical quantity to consider in a convergence study, observationally the circular velocity (or cumulative mass) is more relevant. Velocity curves suffer more from numerical convergence issues because they rely on the integrated density. Fig. 2.2 shows the circular velocity profiles of the low- (dashed) and high-resolution (solid) simulations with CDM in black and SIDM in yellow. The lower panel shows the relative difference as a function of radius, with the Power radii of the low-resolution runs marked for comparison as vertical dashed lines. The low-resolution rotation curve in CDM starts to underpredict visibly compared to the higher resolution run at about 1.4 times the Power radius (some 14 times the formal force softening ϵ) and disagrees by more than 5% at $\sim 1.2 \times \mathrm{r_{Power}}$. The SIDM run, however, remains reasonably well converged throughout: the high- and-low resolution simulations do not disagree by more than 4% outside of $\sim 0.6 \times \mathrm{r_{Power}}$, and not by more than 5% outside of 100 pc.

For the remainder of this work, we present high-resolution density profiles of CDM haloes down to the Power radius and to half the Power radius for SIDM profiles. Based on the work presented in this section, we believe that the full regions plotted are converged. For rotation curves, we plot both CDM and SIDM haloes to 200 pc. This is the $1.2\mathrm{r_{Power}}$ limit for the CDM curves, where we expect them to be correct within $\lesssim 5\%$. The SIDM rotation curves are accurate to the last plotted point.

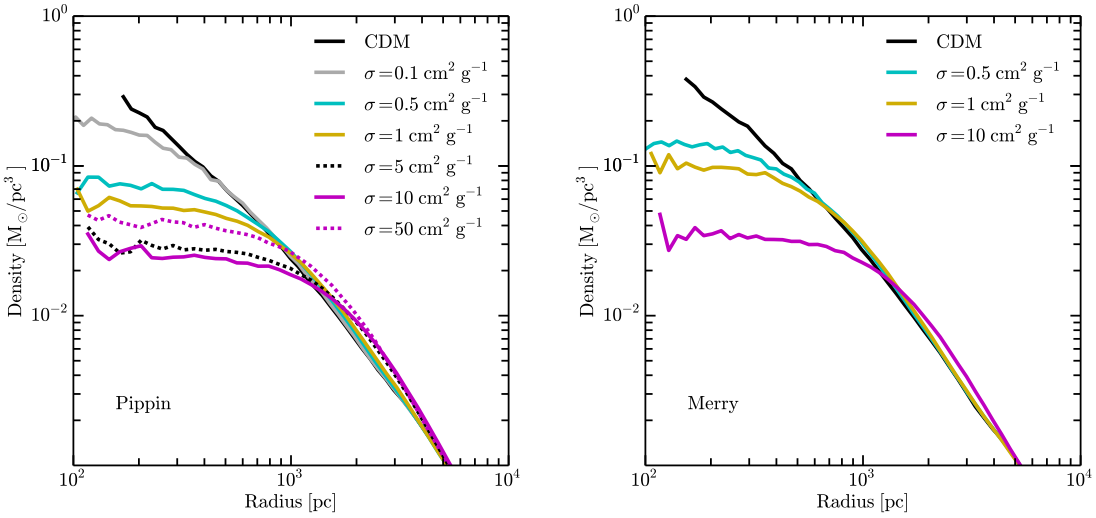

Figure 2.3: Density profiles of Pippin (left) and Merry (right) in collisionless CDM and in SIDM (see legend) at $z = 0$. All SIDM runs with $\sigma/m \geq 0.5$ cm^2 g^{-1} produce central density profiles with well-resolved cores within ~ 500 pc. Core densities are the lowest (and core sizes the largest) for cross-sections in the range $\sigma/m = 5 - 10$ cm^2 g^{-1}. The 50 cm^2 g^{-1} run of Pippin has undergone a mild core collapse, with a resultant central density intermediate between the 10 and 1 cm^2 g^{-1} run. For velocity dispersion profiles of these haloes, see Appendix 2.4.5. NFW fits to the CDM profiles of each halo yield scale radii of ~ 2.7 kpc.

2.4 Results

2.4.1 Halo Profiles

Fig. 2.3 presents the density profiles of our resultant haloes. While the $\sigma/m = 0.1$ cm^2 g^{-1} run of Pippin produces only a modest reduction in core density compared to CDM, all SIDM runs with $\sigma/m \geq 0.5$ cm^2 g^{-1} result in substantial $\sim 500 - 1000$ pc cores, with reduced central densities compared to CDM. As the SIDM cross-section is increased from $\sigma/m = 0.1 \rightarrow 5 - 10$ cm^2 g^{-1} the cores become increasingly extended and have lower central densities. However, the Pippin run with $\sigma/m = 50$ cm^2 g^{-1} has a denser core than the $\sigma/m = 10$ cm^2 g^{-1} case. This is almost certainly due to core-collapse behaviour (e.g. Kochanek & White, 2000; Balberg et al., 2002; Colín et al., 2002; Koda & Shapiro, 2011). As illustrated and discussed in Appendix 2.4.5, the velocity dispersion profile of this run is

noticeably hotter in the core than in the outer regions – a clear indication that a negative heat flux is in action. However, note that even a cross-section as large as 50 $\mathrm{cm}^2\ \mathrm{g}^{-1}$ results in a significantly lower central density than the CDM case, with a clear constant-density core within ~ 500 pc. Evidently, for this particular halo at least, a cross-section as large as 50 $\mathrm{cm}^2\ \mathrm{g}^{-1}$ does not produce runaway core collapse, but rather a mild increase in the central density compared to a run with 10 times weaker self-interaction (5 $\mathrm{cm}^2\ \mathrm{g}^{-1}$).

Our results on core collapse are not significantly different than those reported most recently in the literature. Older simulations of isolated haloes showed core recollapse after a few dynamical times for an equivalent cross-section larger than $\sim 5\ \mathrm{cm}^2\ \mathrm{g}^{-1}$ (scaled appropriately to the mass of Pippin; Kochanek & White, 2000; Balberg et al., 2002; Koda & Shapiro, 2011). However, cosmological haloes only core collapse for higher cross-sections, and not consistently for a fixed halo mass (Yoshida et al., 2000; Colín et al., 2002; Davé et al., 2001; Rocha et al., 2013). There are several reasons why cosmological haloes might produce differences from isolated haloes (Yoshida et al., 2000; Colín et al., 2002). These include the cosmological accretion of new matter into the halo over time as well as velocity dispersion profiles that can deviate from idealized models significantly. Major mergers can also change the heat flux within haloes significantly, thought they do not appear responsible for suppressing core-collapse in our simulations; both Merry and Pippin have quiescent merger histories, with their last major mergers occurring at $z = 1.5$ and 4, respectively. This indicates that even without the stabilizing effect of mergers, a high cross-section ($\sigma \gtrsim 10\ \mathrm{cm}^2\ \mathrm{g}^{-1}$) is required for haloes to core collapse. Similarly, Vogelsberger et al. (2012) studied subhaloes and only found evidence for core collapse in their largest constant cross-section run ($\sigma/m = 10\ \mathrm{cm}^2\ \mathrm{g}^{-1}$). and, even then, only for a single subhalo, even though subhaloes are biased against major mergers.

In summary, even for the two fairly quiescent haloes we simulate (with no major mergers since at least $z = 1.5$), core collapse does not occur except in models with extremely large

($\sigma \gtrsim 10$ cm^2 g^{-1}) cross-sections. Even in these cases, the core collapse is fairly mild, with resultant central densities that remain lower than they would be in CDM. In systems with recent major mergers, we would expect the core collapse to be even less pronounced.

2.4.2 Circular Velocities and TBTF

According to the ELVIS simulations of the Local Group (Garrison-Kimmel et al., 2014a), there should be ~ 10 isolated haloes with $V_{\rm max} \gtrsim 40$ km s^{-1} in the local (~ 1.2 Mpc) field around the MW and M31, excluding satellites of either large system. Of the 14 isolated dwarfs in this volume, only 1 (Tucana) is clearly dense enough to reside in a CDM halo larger than 40 km s^{-1}. Tucana itself is extremely dense, and as discussed in Garrison-Kimmel et al. (2014b), it is difficult to understand, even in the context of CDM. Tucana's density suggests a CDM halo with $V_{\rm max} > 70$ km s^{-1}, similar in size to the halo expected to host the Small Magellanic Cloud. If we force Tucana to reside within one of the typical $V_{\rm max} \simeq 40$ km s^{-1} haloes we expect within ~ 1 Mpc, then this leaves roughly nine isolated, massive haloes unaccounted for. These missing, or overdense, haloes are the systems of concern for TBTF.

Fig. 2.4 illustrates this problem explicitly by comparing the circular velocities of nearby field dwarfs at their half-light radius (data points) to the circular velocity profiles of our simulated haloes (lines), each of which has $V_{\rm max} \simeq 40$ km s^{-1} and is therefore nominally a TBTF halo. The data points indicate local dwarf galaxies ($M_* < 1.7 \times 10^7$) farther than 300 kpc from both the MW and Andromeda that are DM dominated within their half-light radii ($r_{1/2}$), with estimates for their circular velocities at $r_{1/2}$ ($V_{1/2}$). We restrict our observational sample to the local volume because this is where galaxy counts are complete at halo masses around $10^{10} M_\odot$. Note that we do not consider galaxies with rotation curves derived from gas physics (e.g. Oh et al., 2011) as these data are obtained from such large volumes that they are incomplete at this mass scale. $V_{1/2}$ for the purely dispersion galaxies are calculated using the

Wolf et al. (2010) formula, where measurements for stellar velocity dispersion, $\sigma_\star$, are taken from Hoffman et al. (1996), Simon & Geha (2007), Epinat et al. (2008), Fraternali et al. (2009), Collins et al. (2013) and Kirby et al. (2014). However, Tucana, WLM and Pegasus also display evidence of rotational support, indicating that they are poorly described by the Wolf et al. (2010) formalism. For the first two, we use the Leaman et al. (2012) estimate of the mass within the half-light radius, obtained via a detailed dynamical model. The data point for Pegasus is obtained via the method suggested by Weiner et al. (2006), wherein $\sigma_\star^2$ is replaced with $\sigma_\star^2 + \frac{1}{2}(v \sin i)^2$ in the Wolf et al. (2010) formula, where $v \sin i$ is the projected rotation velocity. (also see section 5.2 of Kirby et al., 2014). We plot Tucana as an open point to highlight its extreme density, as discussed above.

As expected, the all of data points save Tucana lie below the CDM curves (black lines), demonstrating explicitly that both Merry and Pippin are TBTF haloes. The SIDM runs, however, provide a much better match, and in fact all of the SIDM runs with $\sigma/m \geq 0.5$ cm^2 g^{-1} alleviate TBTF.

2.4.3 Expectations for the stellar-mass halo-mass relation

A problem related to TBTF, but in principle distinct from it, concerns the relationship between the observed core densities of galaxies and their stellar masses. Specifically, there does not appear to be any correlation between stellar mass and inner DM density inferred from dynamical estimates of dwarf galaxies in the Local Group (Strigari et al., 2008; Boylan-Kolchin et al., 2012; Garrison-Kimmel et al., 2014b). If DM haloes behave as expected in dissipationless ΛCDM simulations, then we would expect more massive galaxies to have higher DM densities at fixed radius. This ultimately stems from the expectation, born out at higher halo masses, that more massive DM haloes tend to host more massive galaxies.

Consider, for example, the two galaxies Pegasus ($r_{1/2} \simeq 1$ kpc) and Leo A ($r_{1/2} \simeq 500$ pc) in

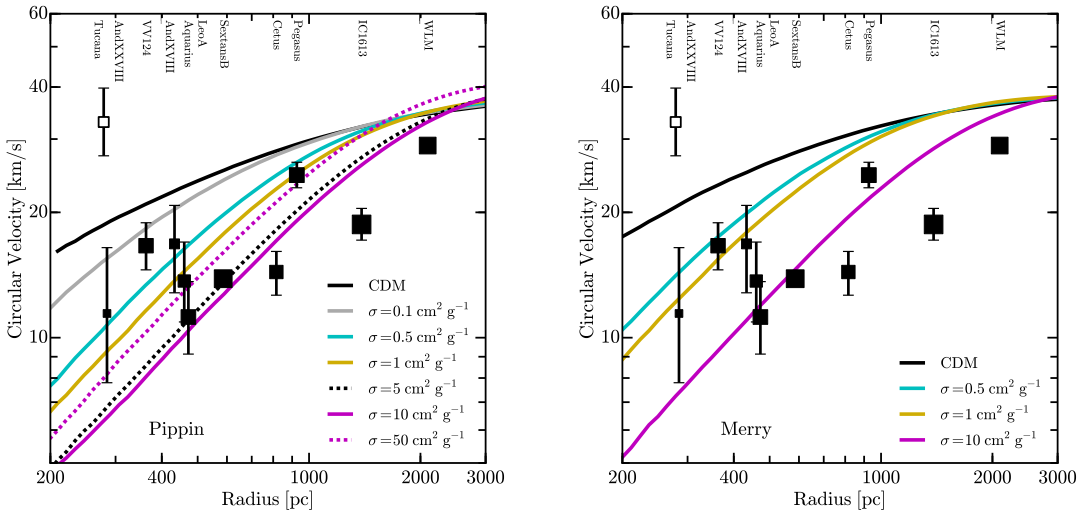

Figure 2.4: Circular velocity profiles of Pippin (left) and Merry (right) simulated with CDM (solid black) and various SIDM cross-sections (see legend). Halos of this mass ($V_{\rm max} \simeq 40$ km s^{-1}) should be fairly common within the ~ 1 Mpc Local Field of the MW. The data points indicate measurements of the circular velocity at the half-light radii of Local Field (as defined in Garrison-Kimmel et al., 2014b) dwarf galaxies (see references in text). The sizes of the points scale with the stellar mass of the galaxy, with the smallest AndXXVIII at $M_\star \simeq 3\times10^5 M\odot$ and the largest IC 1613 at $M_\star \simeq 2\times10^8 M\odot$. While these $V_{\rm max} \simeq 40$ km s^{-1} haloes are too dense in CDM to host any of the plotted Local Field dwarfs, the same haloes in SIDM with $\sigma/m \geq 0.5$ cm^2 g^{-1} are consistent with many of the data points.

Fig. 2.4. Both of these galaxies have about the same stellar mass $M_\star \simeq 10^7 M\odot$. According to the expectations of abundance matching (Garrison-Kimmel et al., 2014b), each of these galaxies should reside within a $V_{\rm max} \simeq 40$ km s^{-1} halo. Instead, their central densities are such that, if their DM structure follows the CDM-inspired NFW form, they need to have drastically different potential well depths: $V_{\rm max} \simeq 30$ and 12 km s^{-1} for Pegasus and Leo A, respectively (see fig. 12 of Garrison-Kimmel et al., 2014b). However, if we instead interpret their densities in the context of SIDM, the results are much more in line with abundance matching expectations.

Abundance matching relations remain unchanged in SIDM because halo mass functions in SIDM are identical to those in CDM (Rocha et al., 2013). That is, in SIDM, just like CDM, we would naively expect both Pegasus and Leo A to reside in haloes with $V_{\rm max} = 40$ km s^{-1}, like Pippin and Merry. In SIDM, unlike in CDM, the predicted density profiles allow this to happen self-consistently. In the right-hand panel of Fig. 2.4 we see that *both* Pegasus and Leo A could be hosted by Merry with $\sigma/m = 10$ cm^2 g^{-1}. In the left-hand panel, both galaxies are consistent with the $\sigma/m = 50$ cm^2 g^{-1} line. Given the obvious halo-to-halo scatter and small number of simulations we have, it is difficult to determine which cross-section would be favoured, but it is clear that for these haloes SIDM predicts central densities much more in line with naive expectations for the stellar mass to halo mass relation at the mass scale of dwarfs.

We extend this analysis to smaller stellar masses in the next subsection, where we also address whether high values of σ/m are forbidden by the dynamics of the Local Group dwarfs.

2.4.4 Are any cross-sections too large to accommodate measured densities?

We would like to be able to rule out some range of cross-sections on the velocity scale of dwarf galaxies by requiring that DM densities at least as high as those observed can be achieved. This is in some sense the inverse of the standard central-density problem: for what SIDM cross-sections are galaxies *too dense*?

Aside from Tucana, the densest Local Field galaxies shown in Fig. 4 are And XVIII ($r_{1/2} \simeq$ 400 pc) and And XXVIII ($r_{1/2} \simeq 300$ pc) with average densities just under 0.1 $M \odot$ pc^{-3}. In practice, the mass uncertainties on these galaxies are so large that it will be difficult to derive stringent constraints. At face value, however, the $\sigma/m = 10$ cm^2 g^{-1} lines do appear to be somewhat underdense (by a factor of $\sim$ 2-3) compared to the central data points.

The difficulty in this comparison is that we expect that the core densities of SIDM haloes will *increase* with decreasing $V_{\rm max}$ (Rocha et al., 2013). We must account for this possibility in any attempt to rule out a given cross-section based on an observed galaxy density.

In order to estimate a $V_{\rm max}$ scale that might be reasonable for these galaxies we can turn to abundance matching. These dense dwarfs have $M_\star \simeq$ 3-8$\times 10^5 M\odot$. According to abundance matching estimates (Garrison-Kimmel et al., 2014a), we expect galaxies in this stellar mass range to reside within $V_{\rm max} \simeq$ 20-30 km s^{-1} haloes.

How much denser is a $V_{\rm max} = 20$ km s^{-1} halo than a $V_{\rm max} = 40$ km s^{-1} halo in SIDM? Fig. 2.5 provides some insight. Plotted are fitted halo core densities (assuming a Burkert 1995 profile), $\rho_{\rm b}$, as a function of $V_{\rm max}$ for SIDM simulations with $\sigma/m = 1$ cm^2 g^{-1}. The black squares show haloes from the simulations of Rocha et al. (2013) while the coloured squares show the two haloes discussed in this paper. The dotted line shows a $\rho_{\rm b} \propto V_{\rm max}^{-1}$ scaling (a power law fit to all the plotted points yields $\rho_{\rm b} \propto V_{\rm max}^{-0.9}$).

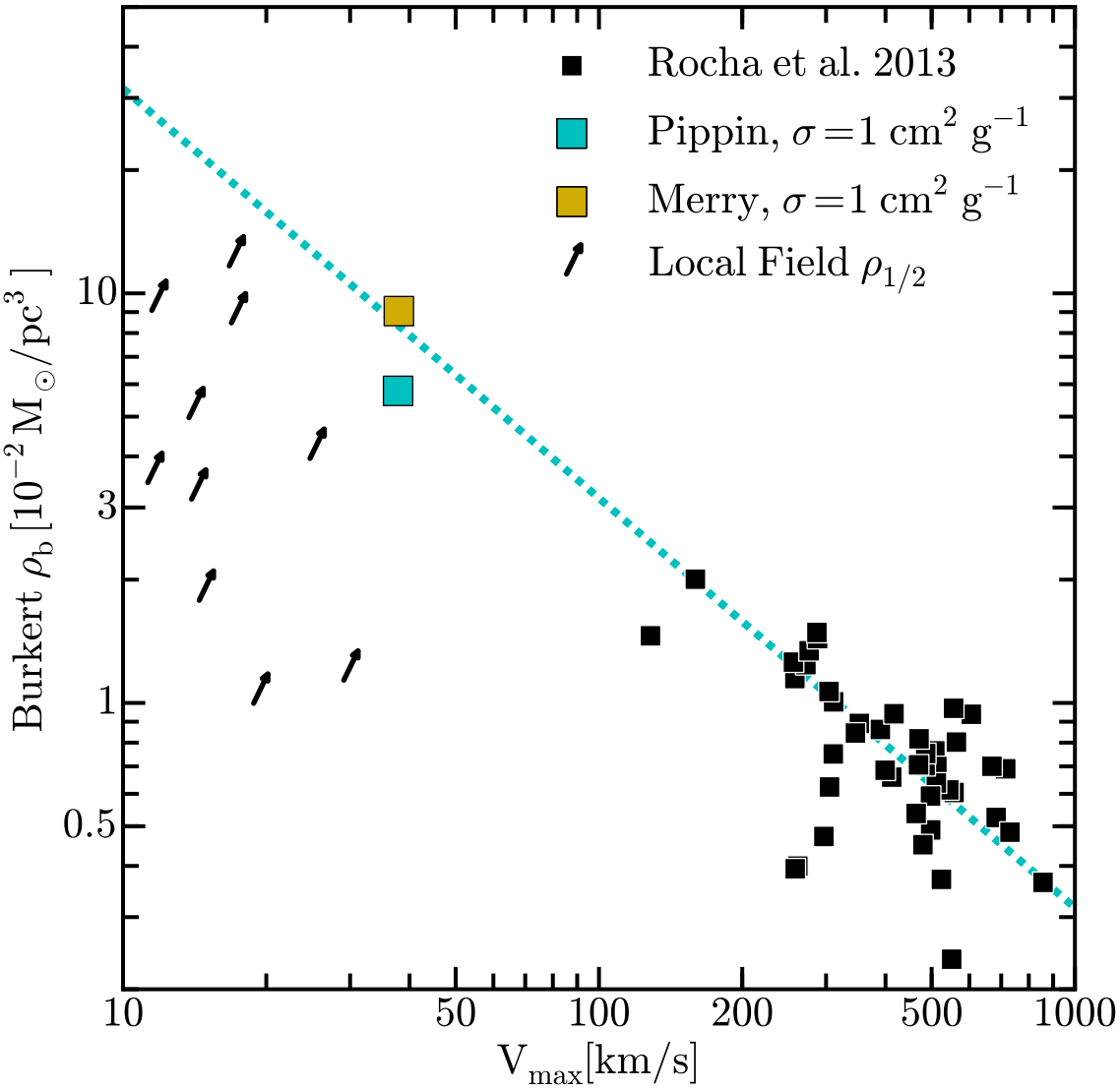

Figure 2.5: Central densities of SIDM haloes from fitted Burkert (1995) profiles are plotted versus the maximum circular velocities of the haloes. Black points are taken from Rocha et al. (2013) and the coloured points indicate Merry and Pippin with $\sigma/m = 1$ cm^2 g^{-1}. The dotted line corresponds to a $1/V_{\rm max}$ scaling. Though there is significant scatter at fixed mass, smaller haloes have higher central densities. The arrows represent the inferred half-light density and half-light velocity dispersions of the Local Field dwarfs plotted in Fig. 2.4, which serve as lower limits on the galaxies' central densities. Of note is the fact that all of these limits are consistent with the $\sigma = 1$ cm^2 g^{-1} scaling, save for Tucana, whose half-light density is so high (78×10^{-2} M$_\odot$/pc^3) as to lie above the limits of the plot.

The arrows show the densities of Local Field dwarfs at their half-light radii ($\rho_{1/2} = M_{1/2}/\frac{4}{3}\pi r_{1/2}^3$) plotted against their implied circular velocities ar $r_{1/2}$ ($V_{1/2} = \sqrt{GM_{1/2}/r_{1/2}}$). If these dwarfs have constant density cores then $\rho_{1/2}$ represents a lower limit on the density of that core: if the core radius is smaller than the half-light radius then the true core density will be higher than the implied average density at $r_{1/2}$; if, on the other hand, $r_{1/2} > r_{\rm core}$, then the average density at $r_{1/2}$ is the core density. We also assume a rising rotation curve at $r_{1/2}$, and this allows us to treat the observed $V_{1/2}$ as lower limits on $V_{\rm max}$. Dwarfs lying above the relation implied by our simulations and those of Rocha et al. (2013) are therefore too dense within their half-light radius to reside in an SIDM halo with a given cross-section. We note that Tucana's half-light density is so high (78×10^{-2} $\mathrm{M_\odot/pc^3}$ with a half-light velocity of 33 km $\mathrm{s^{-1}}$) that it lies above the plotted region. As discussed in Section 2.4.2, this central density places Tucana not only in tension with SIDM models, but also with CDM, so we discount it in our analysis. It is clear from Fig. 2.5, however, that none of the other dwarfs are in conflict with $\sigma/m = 1$ $\mathrm{cm^2\ g^{-1}}$. If the same $\rho_{\rm b} \propto V_{\rm max}^{-1}$ behaviour holds for core densities in $\sigma/m = 10$ $\mathrm{cm^2\ g^{-1}}$ models, then presumably the lower normalization of the $\rho_{\rm b}$-$V_{\rm max}$ relation could place it in tension with the denser field dwarfs, though the large scatter in simulated haloes makes this a loose constraint.[2] Such a model then remains viable in the face of current constraints.

Thus it appears difficult to rule out any cross-sections based on the observed densities of isolated field dwarfs in the Local Group. The same conclusion holds for Milky Way satellites if one considers fig. 8 of Vogelsberger et al. (2012): SIDM with $\sigma/m = 10$ $\mathrm{cm^2\ g^{-1}}$ (on the velocity scale of dwarf galaxies) can match the spread of local densities seen for the classical satellites of the MW. A larger simulation suite that includes a range of halo masses and more precise observational mass measurements may eventually allow such a constraint to be derived.

[2]This assumes a constant SIDM cross-section. If the cross-section is instead velocity dependent this will change, most likely resulting in a shallower power law fit.

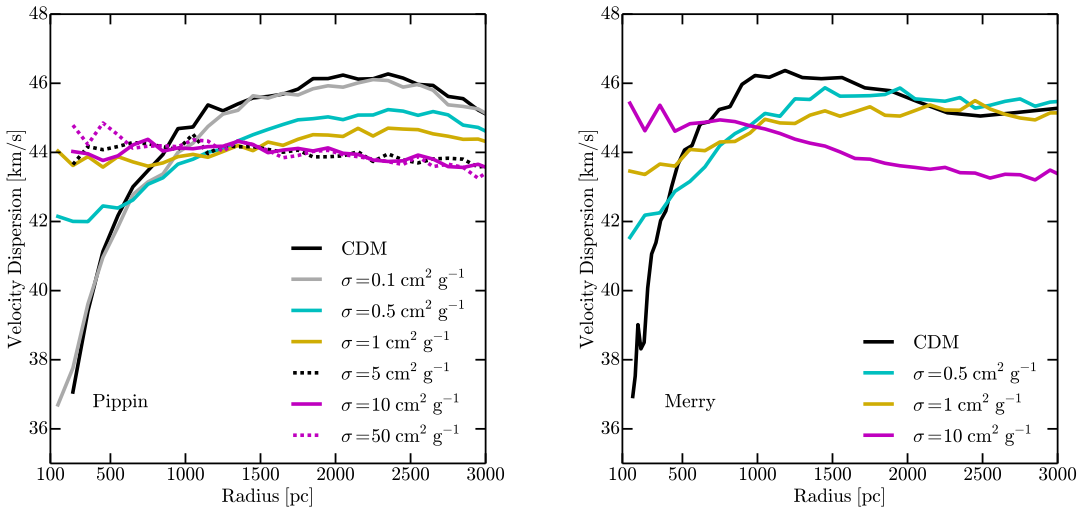

Figure 2.6: Velocity dispersion profiles of Pippin (left) and Merry (right) in collisionless CDM and with a variety of SIDM cross-sections (see legend). As the cross-section increases to $\sigma/m = 10$ cm^2 g^{-1}, the cores become increasingly hotter and the profiles become more isothermal as kinetic energy is transported to the center of the halo. Very high cross-sections $\sigma/m \geq 10$ cm^2 g^{-1} lead to a negative radial gradient, resulting in energy transport from the center of the halo to the outer parts, resulting in mild core collapse and higher central densities, as in the 50 cm^2 g^{-1} run plotted in Figure 2.3.

Overall, we emphasize that the puzzling 'common mass' relation inferred from collisionless CDM simulations, where luminous galaxies are no more dense, and potentially less dense, than galaxies 1000 times dimmer (as is seen in the Local Group, e.g. Strigari et al., 2008; Boylan-Kolchin et al., 2012; Garrison-Kimmel et al., 2014b), is a natural consequence of SIDM, where halo core densities generally increase with decreasing halo mass.

2.4.5 Velocity dispersion profiles

The velocity dispersion profiles of SIDM haloes provide insight into the origin and nature of their cored density structures. Figure 2.6 plots the velocity dispersion profiles of our haloes both in collisionless CDM and in SIDM, in direct analogy to the density profiles shown in Figure 2.3. As the SIDM cross-section is increased from $\sigma/m = 0.1 \rightarrow 5 - 10$ cm^2 g^{-1}, the cores become steadily hotter and more isothermal as kinetic energy is transported from the

outside in (resulting in increasingly lowered central densities relative to the cold cusp that forms in CDM). However, the run with a cross-section larger than $\sigma/m \sim 10$ cm^2 g^{-1} begins to display a negative radial gradient – i.e., a core that is hotter than the outer regions. This is precisely the situation where core collapse behavior is expected in SIDM: heat is transferred out of the halo center, resulting in decreased pressure support and ultimately a density enhancement (and further heating). This core collapse behavior is seen explicitly in the left panel of Figure 2.3, where the Pippin run with $\sigma/m = 50$ cm^2 g^{-1} is much denser than the $\sigma/m = 5, 10$ cm^2 g^{-1} cases.

2.4.6 Comparisons to Classical Milky Way Satellites

While Pippin and Merry are isolated dark matter haloes, rather than subhaloes, it is nonetheless interesting to compare their velocity profiles to the brightest Milky Way dwarf satellites. Figure 2.7 plots the same circular velocity profiles of Pippin as in Figure 2.4, but with the data points replaced by measurements of the circular velocities of the bright ($M_\star > 2 \times 10^5 M\odot$) Milky Way satellites used to define TBTF in Boylan-Kolchin et al. (2011, 2012). The points are taken from Wolf et al. (2010), who used data from Muñoz et al. (2005), Koch et al. (2007), Simon & Geha (2007), Mateo et al. (2008), and Walker et al. (2009). As in the field (Figure 2.4), SIDM runs with $\sigma/m \geq 0.5$ cm^2 g^{-1} alleviate TBTF significantly. Because the simulated haloes have not been tidally stripped by a larger host halo, however, a quantitative comparison is impossible and we instead present these results for illustrative purposes only.

2.5 Conclusions

In this work, we have used very high resolution cosmological simulations of $V_{\rm max} = 40$ km s^{-1} haloes to investigate the effect of SIDM on their density structure. By simulating a range of

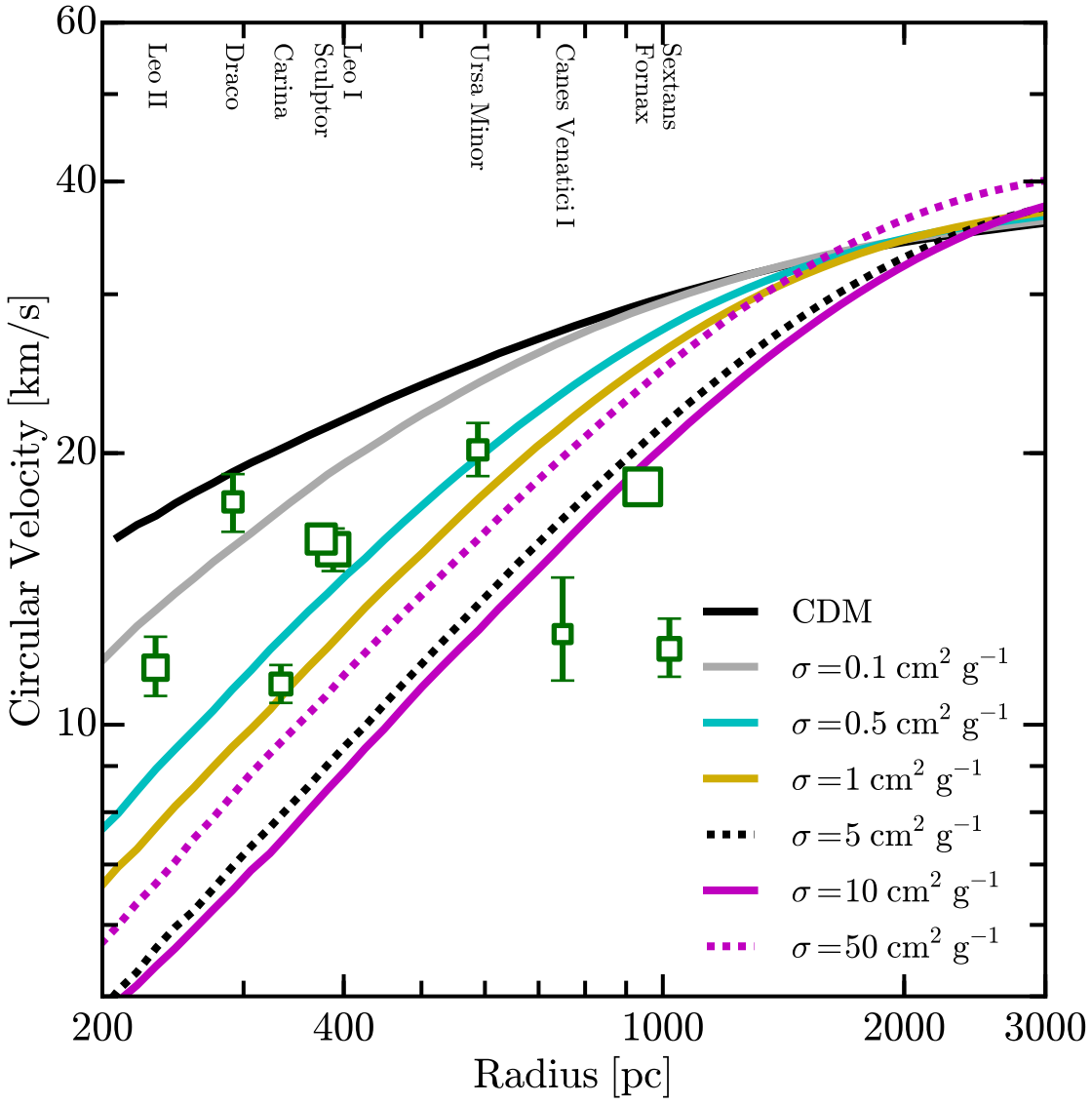

Figure 2.7: Circular velocity profiles of Pippin as in Figure 2.4, but with constraints on the circular velocities of the bright Milky Way satellites, from Wolf et al. (2010). SIDM simulations with $\sigma/m \geq 0.5$ cm^2 g^{-1} resolve TBTF, as in the field. However, the simulated haloes have not undergone the environmental processes typical of subhaloes and satellite galaxies; a quantitative comparison is therefore impossible.

SIDM cross-sections and comparing our simulations to the observed masses of Local Field dwarfs we have reached the following conclusions:

- SIDM models with $\sigma/m \simeq 0.5\text{-}50$ cm^2 g^{-1} on the velocity scale of dwarf galaxies ($v_{\rm rms} \simeq 40$ km s^{-1}) alleviate TBTF and produce constant-density core profiles comparable in size to the half-light radii of Local Field dwarfs. It is possible that cross-sections even larger than 50 cm^2 g^{-1} will alleviate the problem without producing catastrophic core collapse.

- The largest (~ 1 kpc), lowest density ($\sim 0.03\ M\odot$ pc^{-3}) cores occur for models with $\sigma/m \simeq 5 - 10$ cm^2 g^{-1}. Our single run with $\sigma/m = 50$ cm^2 g^{-1} produces a slightly denser core owing to a mild degree of core collapse, yet it retains a constant-density profile at small radii and remains significantly less dense than the CDM case.

- SIDM halo core densities increase inversely with halo circular velocity, roughly as $\rho_{\rm core} \propto 1/V_{\rm max}$ (Fig. 5). This fact may help explain the unusual trend for less luminous dwarf galaxies to be denser or as dense as galaxies 1000 times brighter (Strigari et al., 2008). However, this behaviour also makes it difficult to rule out SIDM models by requiring haloes to be at least as dense as the densest known dwarfs (e.g. And XVIII or Draco) since the host $V_{\rm max}$ is not well constrained.

A much larger number of simulations, coupled with more precise measurements of dwarf galaxy densities, are required to place tight constraints on σ/m at these velocity scales. Further research, which is currently underway (Vogelsberger et al., 2014; Elbert et al., in preparation; Robles et al., in preparation), is also needed to investigate the effects of baryons on density profiles in an SIDM universe. Overall, however, our results suggest that a wide range of SIDM cross-sections remain viable on the velocity scales of dwarf galaxies, and that the range of cross-sections that can alleviate TBTF spans at least two orders of magnitude.

Chapter Acknowledgments

We thank Manoj Kaplinghat for helpful discussions. Support for this work was provided by NASA through *Hubble Space Telescope* grants HST-GO-12966.003-A and HST-GO-13343.009-A. This work used the Extreme Science and Engineering Discovery Environment (XSEDE), which is supported by National Science Foundation grant number ACI-1053575. We also acknowledge the computational support of the *Greenplanet* cluster at UCI, upon which much of the secondary analysis was performed.

Chapter 3

A Testable Conspiracy: Simulating Baryonic Effects on Self-Interacting Dark Matter Halos

3.1 Chapter Abstract

We investigate the response of self-interacting dark matter (SIDM) halos to the growth of galaxy potentials using idealized simulations, each run in tandem with standard collisionless Cold Dark Matter (CDM). We find a greater diversity in the SIDM halo profiles compared to the CDM halo profiles. If the stellar gravitational potential strongly dominates in the central parts of a galaxy, then SIDM halos can be as dense as CDM halos on observable scales. For extreme cases with highly compact disks core collapse can occur, leading to SIDM halos that are denser and cuspier than their CDM counterparts. If the stellar potential is not dominant, then SIDM halos retain constant density cores with densities far below CDM predictions. When a disk potential is present, the inner SIDM halo becomes *more flattened* in the disk

plane than the CDM halo These results are in excellent quantitative agreement with the predictions of Kaplinghat et al. (2014a). We also simulated a galaxy cluster halo with a central stellar distribution similar to the brightest central galaxy of the cluster A2667. A SIDM halo simulated with cross section over mass $\sigma/m = 0.1$ cm^2 g^{-1} provides a good match to the measured dark matter density profile of A2667, while an adiabatically-contracted CDM halo is denser and cuspier. The cored profile of the same halo simulated with $\sigma/m = 0.5$ cm^2 g^{-1} is not dense enough to match A2667. Our findings are in agreement with previous results that $\sigma/m \gtrsim 0.1\,\mathrm{cm}^2\ \mathrm{g}^{-1}$ is disfavored for dark matter collision velocities in excess of about 1500 km/s. More generally, the predictive cross-talk between baryonic potentials and SIDM density distributions offers new directions for constraining SIDM cross sections in massive galaxies where baryons are dynamically important.

3.2 Introduction

The dark matter (DM) paradigm has been tremendously successful in explaining the large-scale structure of our universe (see, e.g. Planck Collaboration et al., 2015; Rodríguez-Torres et al., 2016), though the precise nature of dark matter remains unknown. The simplest example of cold dark matter (CDM), consisting of a single, collisionless particle with negligible primordial thermal velocity dispersion, can match the large-scale data remarkably well. Alternatively, dark matter could be more complex, with nongravitational coupling to standard model particles (e.g. Boehm & Schaeffer, 2005; Escudero et al., 2015) and/or new dark sector particles (e.g. Feng et al., 2010b; Khlopov et al., 2010; Lesgourgues et al., 2016); many models of this kind produce observable signatures in astronomical data sets (Mangano et al., 2006; Feng et al., 2009; Cyr-Racine et al., 2015). In this paper we consider the possibility that dark matter has strong elastic self-scattering interactions and explore the implications of such interactions on the dark matter distributions within individual galaxies.

We specifically focus on the back-reaction associated with galaxy formation.

Collisional or Self-Interacting dark matter (SIDM) was first explored in the context of galaxy formation by Spergel & Steinhardt (2000), who argued that SIDM models with cross-section over mass $\sigma/m \sim 1$ cm^2 g^{-1} should lead to observable constant density cores in galaxies, in agreement with observations at that time. While early estimates suggested that SIDM models of this kind would significantly reduce substructure counts compared to CDM, more recent numerical investigations have shown that the substructure differences are minimal (Vogelsberger et al., 2012; Rocha et al., 2013). However, the original expectation that SIDM halos should have constant-density cores has been demonstrated robustly in cosmological simulations (Davé et al., 2001; Rocha et al., 2013; Zavala et al., 2013).

SIDM cores are generated by energy-exchange interactions, which heat the halo center until it becomes isothermal. The radial extent of this core is set by the requirement that a typical dark matter particle will experience at least one interaction per Hubble time (Rocha et al., 2013). This implies that larger SIDM cross sections produce larger isothermal cores. If the cross section is large enough, the isothermal region can extend beyond the peak in the halo's velocity dispersion profile; in this case, energy-exchange interactions could extract heat from the core leading to core-collapse, which increases the central density (Kochanek & White, 2000; Balberg et al., 2002; Colín et al., 2002; Koda & Shapiro, 2011; Vogelsberger et al., 2012). However, this effect is muted in cosmological simulations and Elbert et al. (2015) used dark matter (only) zoom cosmological simulations to show that core-collapse behavior sets in only for very large cross sections $\sigma/m \gtrsim 10$ cm^2 g^{-1}.

The tendency for SIDM models with $\sigma/m \lesssim 10$ cm^2 g^{-1} to produce constant-density cores with lower overall density is of special interest for comparisons to dwarf and low surface brightness (LSB) galaxies. This is because many of these galaxies are observed to have cores on roughly the scales expected in SIDM (Flores & Primack, 1994; Moore, 1994; de Blok et al., 1996; Salucci & Burkert, 2000; de Blok et al., 2001; Swaters et al., 2003; Gentile et al.,

Name	M_v ($10^{12} M\odot$)	c_v	N_p (10^6)	r_{cut} (kpc)	ϵ (kpc)	Convergence Radius (kpc)	Potential Shape	M_{gal} ($10^{10} M\odot$)	a (kpc)	b (kpc)	h (kpc)
MW	1.0	13	3	230	0.4	0.83	MN Disk	5.0	$1.5, 3.0, 6.0$	0.3	–
LSB	0.2	11.8	10	170	0.19	0.30	MN Disk	0.06	2.2	0.2	–
Elliptical	1.8	9.7	10	300	0.37	1.0	Hernquist Sphere	6.2	–	–	3.0
Cluster	10^3	3	50	500	2	3.4	Hernquist Sphere	210	–	–	28.5

Table 3.1: Summary of simulated halos. The first five columns list identifying names and general simulation properties: halo mass, NFW concentration, particle number, exponential cutoff radius and force softening. We define M_v following Bryan & Norman (1998) with a virial overdensity of $\Delta_v = 97$ with respect to the critical density. The sixth column lists the convergence radius for the SIDM runs, which we set to 0.6 times the Power et al. (2003) radius for CDM as found in Elbert et al. (2015). The last four columns summarize the properties of the galaxy potentials grown in each case, where M_{gal} is the final galaxy mass and the other shape parameters are defined in Equations 3.1 and 3.2. Note that there are three separate disks of varying scale length for the Milky Way runs. We refer to these in the text and figures as 'Compact', 'Fiducial', and 'Extended.'

2004; Simon et al., 2005; Spekkens et al., 2005; Kuzio de Naray et al., 2008; de Blok et al., 2008; Donato et al., 2009; Oh et al., 2011; Adams et al., 2014) as opposed to the cusps predicted in dissipationless CDM simulations (Dubinski & Carlberg, 1991; Navarro et al., 1997). SIDM cores also may provide a natural explanation for the unexpectedly low densities of local dwarf galaxies (Vogelsberger et al., 2012, 2014; Elbert et al., 2015), a problem known as "Too Big to Fail" (TBTF) (Boylan-Kolchin et al., 2011, 2012; Ferrero et al., 2012; Klypin et al., 2014; Papastergis et al., 2014; Garrison-Kimmel et al., 2014b; Tollerud et al., 2014). There are many in the galaxy formation community who believe these issues may be resolved by baryonic processes such as supernova feedback (Navarro et al., 1996; Read & Gilmore, 2005; Pontzen & Governato, 2012; Governato et al., 2012; Di Cintio et al., 2014; Oñorbe et al., 2015; Maxwell et al., 2015; Dutton et al., 2016; Katz et al., 2016; Read et al., 2016) though not all authors necessarily agree (Peñarrubia et al., 2012; Garrison-Kimmel et al., 2013; Pace, 2016). Tidal effects have been shown to solve TBTF in satellite galaxies (see e.g. Read et al., 2006; Zolotov et al., 2012; Brooks & Zolotov, 2014; Del Popolo et al., 2014; Arraki et al., 2014), but the evidence for TBTF in the local field (Kirby et al., 2014; Garrison-Kimmel et al., 2014b) necessitates another solution for these galaxies. This ongoing debate and the lack of DM detections in direct, indirect and collider searches motivates a thorough exploration of the SIDM hypothesis.

The goal of this paper is to investigate the late-time effects of galaxy formation on SIDM halos, specifically the contraction of these halos due to the gravitational potential of the galaxy. To this end we use a set of N-body simulations similar to those initially used to examine contraction in CDM halos. The work is organized as follows: in §3.3, we briefly describe the properties required of a viable SIDM model and in §3.4, we sketch the physics of contraction of SIDM halos and motivate our work in this paper. We describe our simulations and analysis in §3.5. We present our results in §3.6, discussing our Milky Way analogue halos in §3.6.1 and our elliptical and lsb simulations in §3.6.2, while in §3.6.3 we directly compare our simulations to the analytic model presented in Kaplinghat et al. (2015). §3.7 shows the

results of our cluster simulations, and compares these with the observations of Newman et al. (2013a). We summarize our results and conclude in §3.8.

3.3 Properties of viable SIDM models

Previous work has placed constraints on the SIDM cross section over mass across a range of halo masses. Generally, σ/m below 0.1 cm^2 g^{-1} have been found to be indistinguishable from CDM models (Rocha et al., 2013). In low mass galaxies with maximum circular velocity $V_{\rm max} \simeq 30$ km s^{-1}, σ/m values ranging from 0.5 to 10 cm^2 g^{-1} alleviate the core-cusp and TBTF (Vogelsberger et al., 2012; Zavala et al., 2013; Fry et al., 2015; Elbert et al., 2015). However, values significantly in excess of 1 cm^2 g^{-1} may lead to efficient tidal stripping of stars in the satellites of the MW and Andromeda (Gnedin & Ostriker, 2001; Peñarrubia et al., 2010; Dooley et al., 2016) , providing a possible avenue for an upper limit on the cross section in the future. Recent work by Kaplinghat et al. (2015) showed that SIDM models with cross sections around 2 cm^2 g^{-1} fit the rotation curves of the 12 analyzed dwarf and low surface brightness galaxies well. This work used an analytic model built on arguments discussed previously (Rocha et al., 2013; Kaplinghat et al., 2014a) and showed that the analytic model is a good match for the density profiles of halos in DM-only cosmological SIDM simulations. The summary of above constraints is that for collisional velocities of order 100 km/s or smaller, a σ/m values close to 1 cm^2 g^{-1} is favored and consistent with all existing constraints. A larger sample of rotation curves will reduce uncertainties in the determination of the cross section on galactic velocity scales.

The dark matter velocities in galaxy clusters are an order of magnitude larger than in dwarf galaxies, and many techniques have been used to constrain the DM self-interaction cross section at these velocities. Cluster mergers have been used by many studies to constrain SIDM (see e.g. Randall et al., 2008; Dawson et al., 2012; Kahlhoefer et al., 2014; Massey

et al., 2015; Schaller et al., 2015; Kim et al., 2016; Robertson et al., 2016), with typical limits of $\sigma/m \leq 1$ cm^2 g^{-1} on the self-interaction cross section. However, recent work by Kim et al. (2016) showed that constraints based on the displacement of the stellar and dark matter centroids are overly stringent, weakening previous constraints. They find that the displacement of the brightest cluster galaxy (BCG) relative to the halo center may be a better observable, possibly allowing σ/m values around 0.1 cm^2 g^{-1} to be tested. The Bullet cluster constraint based on the mass loss from the merging sub-cluster (Markevitch et al., 2004) also needs to be reevaluated using self-consistent SIDM merger simulations and taking into account cosmic variance in the initial conditions. In addition, we also need theoretical refinement to apply these constraints to velocity-dependent cross sections. Cluster shapes have provided an orthogonal method of investigating self-interaction cross section on these scales. Core formation in SIDM halos leads to more spherical inner density profiles, so measurements of the ellipticities of cluster halos have been used to constrain σ/m values to below 0.1 cm^2 g^{-1} (Miralda-Escudé, 2002). However, due to the large scatter in axis ratios, the ability of SIDM halos to retain some triaxiality, and the observational methods used to constrain halo shapes, the ellipticity constraints are unlikely to be better than about 1 cm^2 g^{-1} for cluster velocities (see Peter et al., 2013, for a detailed discussion).

The most stringent constraint on cluster velocity scale arises from the fact that the measured dark matter density profiles are in substantial agreement with CDM outside the half-light radii of the BCGs. Within about 10-50 kpc (range of BCG half-light radii), however, the dark matter density profile is shallower than the CDM expectations (Newman et al., 2013a), as we discuss later. Kaplinghat et al. (2015) used these measurements to show that the preferred cross section for relative velocities larger than 1000 km/s is about 0.1 cm^2 g^{-1}, consistent with earlier results from Yoshida et al. (2000). If the inferred shallowness of the density profile is due to AGN feedback or some other baryonic process (Martizzi et al., 2013, e.g.), then this value of 0.1 cm^2 g^{-1} provides a stringent upper limit on the self-interaction cross section for velocities in excess of 1000 km/s. This result and the large difference in DM

velocities in dwarf galaxies and galaxy clusters demand that viable SIDM models must have a velocity dependent self-interaction cross section. The required velocity dependence – from 1 $\mathrm{cm}^2\ \mathrm{g}^{-1}$ for velocities below about 100 km/s to 0.1 $\mathrm{cm}^2\ \mathrm{g}^{-1}$ for velocities above 1000 km/s – can be easily accommodated in a variety of particle physics models (Feng et al., 2010a; Loeb & Weiner, 2011; Tulin et al., 2013b; Cline et al., 2014; Boddy et al., 2014b, 2016).

3.4 Motivation: contraction of SIDM halos

Our work on simulating SIDM halos including a baryonic component is important for two specific reasons. First, in galaxies dominated by baryons there is no systematic evidence for large cores or lowered dark matter density profiles (e.g. Cappellari et al., 2015). Second, in galaxy clusters the stars dominate the total mass budget within their half-light radii, yet the dark matter tends to be under-dense compared to predictions. There is a simple analytic model (which we discuss later) that can explain both these observations but it has not been tested against simulations including a stellar component. By testing the accuracy of the analytic model we are able to bolster the case for a velocity dependent self-interaction cross section. We also test the possibility of core collapse in systems that have extremely dense baryonic distributions.

In this work, our aim is to test and further elucidate the general physics of how SIDM halos become isothermal in the potential well of the baryons. Because of this, we have chosen to run idealized simulations with disks grown adiabatically. This is complementary to the approach of running full-fledged hydrodynamic simulations that include self-interactions between dark matter particles. Vogelsberger et al. (2014) and Fry et al. (2015) examine dwarf galaxies ($M_{\mathrm{v}} \sim 10^{10}\ M\odot$) using fully self-consistent hydrodynamic simulations and find that observable cores are still formed in these dwarfs in SIDM. Fry et al. (2015) find that the cores in their simulated dwarfs are not substantially different from those formed

purely via feedback in their CDM simulations. It is not clear how these results generalize to larger halo masses, where feedback is expected to be less important in driving core formation in CDM halos and halo contraction effects are expected to dominate (e.g. Di Cintio et al., 2014; Dutton et al., 2016; Fiacconi et al., 2016).

The fact that growing baryonic potentials can cause contraction of CDM halos was first investigated analytically by Blumenthal et al. (1986) and Ryden & Gunn (1987), who used an adiabatic invariant approach. They demonstrated that if a baryonic potential grew to dominate the central potential, the entire dark halo would contract, increasing the central dark matter density by more than an order of magnitude in plausible cases. Other studies (e.g. Jesseit et al., 2002) ran numerical simulations of isolated DM halos with disk potentials and found the DM density in these halos reproduced analytical predictions. Gnedin et al. (2004) studied baryonic contraction in hydrodynamic cosmological simulations and found that both adiabatic model predictions and isolated simulations produced central densities that were roughly 50% too high in halos where baryons dominate and proposed an alternative model to encapsulate the adiabatic contraction effect.

Though previous work on halo contraction explored collisionless DM, the general results should apply to SIDM as well. The adiabatic contraction occurs at early times when the disk or bulge of a galaxy is forming. These timescales are much shorter than the typical timescale for self-interactions in galaxies, assuming a cross section around 1 $\mathrm{cm}^2\ \mathrm{g}^{-1}$. At later times, the self-interaction process will allow the halo to become isothermal, and this process can make the dark matter density profile shallower, retain the steep density profiles created by adiabatic contraction, or steepen it further in the case of core-collapse. As we show later, the outcome depends on the cross section, the gravitational potential of the baryons and the outer (CDM) dark matter halo profile.

Feedback could change the density profile of dark matter for dwarf galaxies but it is not expected to be important for the baryon dominated systems we simulate, which are Milky

Way size or larger (Di Cintio et al., 2014; Dutton et al., 2016). It is important to note that when the equilibration time scale is short, changes due to feedback need to happen very late in order to prevent the dark matter from moving towards the equilibrium solution.

Kaplinghat et al. (2014a) discussed the response of SIDM halos to the formation of a stellar disk or bulge using analytic equilibrium models. They found that the resultant SIDM core radius and density should be linked closely to the underlying baryonic potential in systems where the baryons are important dynamically. In the limit where the stars dominate the gravitational potential, the dark matter density profile (in the region where it is isothermal) scales as $\exp(-\Phi_\star(r)/\sigma_{v0}^2)$ (Amorisco & Bertin, 2010; Kaplinghat et al., 2014a) where $\Phi_\star$ is the gravitational potential of the stars and σ_{v0} is the 1-d central velocity dispersion of dark matter. Thus, stars and dark matter are tied together in terms of the density profile and the shape of the dark matter halo must follow the contours of the stellar gravitational potential. This result emphasizes the need to account for the baryons when exploring SIDM phenomenology in galaxies with significant gas or stellar components.

The goal of this paper is to numerically investigate the effects of baryonic contraction on SIDM halos using a set of isolated N-body dark matter simulations of Milky Way, Elliptical, LSB, and Cluster analogue halos. These simulations are similar in spirit to those first used to test and confirm analytic contraction models in the context of CDM. All of our halos were simulated with fixed SIDM cross sections of $\sigma/m = 0.5$ cm^2 g^{-1}, but we show below that our simulations reproduce the model of Kaplinghat et al. (2015), indicating we can use their model to extend our results to a wide range of cross sections.

3.5 Simulations

Because we are primarily interested in isolating the effects of baryonic contraction on SIDM halos as opposed to modeling a fully realistic treatment of galaxy formation in an SIDM universe, we ignore the effects of halo growth and baryonic feedback in our simulations. To model halos after rapid early accretion has finished, we choose a spherical Navarro, Frenk, & White (1997) density profile for our initial conditions because it describes the equilibrium state of DM halos well. We may then add the galaxy potential in order to simulate a system without violent starbursts or major mergers. These assumptions and approximations work well for galaxies with quiescent periods greater than SIDM thermalization times ($\lesssim 1$ Gyr).

Our code is a modified version of `GADGET-2` (Springel, 2005) that allows for the inclusion of hard-sphere scattering between dark matter particles (Rocha et al., 2013). The simulations consist of a series of 3 to 50 million particle dark matter halos, initialized as Navarro, Frenk, & White (1997) profiles, and run in isolation with and without an analytic galaxy potential. The potentials are grown linearly in time from a mass of zero to a final mass $M_{\rm gal}$ in 1 Gyr at the start of our simulations. We also simulated our Milky Way halo forming the fiducial disk after the SIDM core stabilized and found no difference in the DM distribution. The particle initial conditions were generated by the public code `SPHERIC` [1], which was first introduced in Garrison-Kimmel et al. (2013). To increase our effective resolution we exponentially truncate the outer regions of our initial NFW halos. These truncation radii lie far outside the halo scale radius except in the case of the Cluster, which we truncate exponentially at 500 kpc in order to resolve the central few kpc of the halo. We have compared our idealized, dark-matter-only halos to analogous cosmological halos presented in Rocha et al. (2013) and found their radial profiles to be in good agreement. This demonstrates that the rapid merging process that forms halos in cosmological simulations does not cause significant deviation from NFW or isothermal profile.

[1] `https://bitbucket.org/migroch/spheric`

Table 3.1 summarizes our simulations, which consist of four characteristic halo/galaxy mass [2] combinations:

1. Milky Way: $M_{\rm v} = 10^{12} M\odot$ with disks $M_{\rm gal} = 5 \times 10^{10} M\odot$;
2. LSB: $M_{\rm v} = 2 \times 10^{11} M\odot$ with disk $M_{\rm gal} = 6 \times 10^{8} M\odot$;
3. Elliptical: $M_{\rm v} = 1.8 \times 10^{12} M\odot$ with $M_{\rm gal} = 6.2 \times 10^{10} M\odot$; and
4. Cluster: $M_{\rm v} = 1 \times 10^{15} M\odot$ with $M_{\rm gal} = 2.1 \times 10^{12} M\odot$.

Each of these simulations are run with CDM and SIDM and also with and without the galaxy potentials for comparison. The Milky Way halo mass simulations include three separate galaxy disk potential runs, each of which has a fixed galaxy mass but variable scale length (see below). We present 22 simulations in all. All SIDM halos were run with $\sigma/m = 0.5$ cm^2 g^{-1} and used a self-interaction smoothing factor of 25 % of the force softening length (Rocha et al., 2013). We also resimulated our cluster halo with $\sigma/m = 0.1$ cm^2 g^{-1}. The force softening and convergence radius (Power et al., 2003; Elbert et al., 2015) of each run are indicated in columns five and six.

For the disk potentials in the LSB and Milky Way runs we adopt the form of Miyamoto & Nagai (1975):

$$\Phi_{\rm MN}(R, z) = \frac{-GM_{\rm gal}}{\sqrt{R^2 + (a + \sqrt{b^2 + z^2})^2}}, \tag{3.1}$$

where a defines a scale length and b sets a scale height.

Each Milky Way simulation has a fixed scale height $b = 0.3$ kpc. We explore three scale lengths: $a = 1.5$, 3.0, and 6.0 kpc, which we refer to as 'Compact Disk', 'Fiducial Disk',

[2] Our virial mass definition follows Bryan & Norman (1998) for a flat LCDM cosmology with $\Omega_{\rm m} = 0.27$.

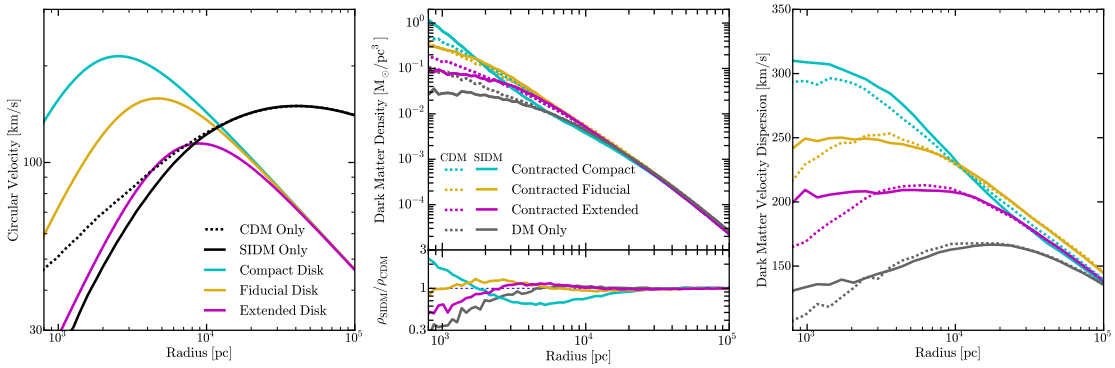

Figure 3.1: *Left:* The black lines show circular velocity profiles for dark-matter only Milky Way size halos (SIDM, solid; CDM, dashed). The colored lines show the circular velocity profiles of three imposed baryonic potentials: Fiducial Disk (yellow), Extended Disk (magenta), and Compact Disk (cyan). *Middle:* Dark matter density profiles without (grey) and with (colored) response to the grown disk potentials. The lower panel shows the ratio of the SIDM run to CDM run as a function of radius for each set of simulations. *Right:* Velocity dispersion profiles of the same halos, which demonstrate isothermal cores for the SIDM runs, as expected. Note that the relative effect of baryonic contraction is much more substantial in SIDM: the central densities at 600 pc increase by a factor of ~ 70 from the non-contracted case to the Compact Disk case in SIDM, compared to only a factor of ~ 5 in the CDM case. Interestingly, the Fiducial Disk runs in SIDM and CDM have very similar normalizations, though the SIDM simulation does show a small core developing within ~ 800 pc. The Compact Disk, on the other hand, has led to core-collapse in the SIDM halo, resulting in a much higher central density than even the contracted CDM halo. Core collapse is expected when the velocity dispersion has a negative gradient within the scattering radius, as is clearly the case for the Compact Disk in the right panel.

and 'Extended Disk', respectively. These values [3] roughly span the lower two-sigma to upper one-sigma of disk sizes for $M_{\rm gal} = 5 \times 10^{10}\ M\odot$ galaxies (Reyes et al., 2011). In particular, the compact disk is extremely dense and was chosen to investigate whether core collapse occurs. Our LSB disk mimics a typical LSB from Kuzio de Naray et al. (2008), with $M_{\rm gal} = 6.3 \times 10^{8}\ M\odot$, $a = 2.2$ kpc, and $b = 0.2$ kpc.

We use spherical Hernquist (1990) distributions for the Elliptical and Cluster galaxy runs:

$$\Phi_{\rm H}(r) = \frac{-GM_{\rm gal}}{(r+h)}. \tag{3.2}$$

For the Elliptical, we adopt $h = 3.0$ kpc and $M_{\rm gal} = 6.2 \times 10^{10} M\odot$ motivated by matching themedian of bin 28 in Graves et al. (2009). We relate the typical effective radius for galaxies of this size by demanding that the 3D half-light radii are equal: $h = R_{\rm e}/1 + \sqrt{2}$. For the central cluster galaxy we match the results for A2667 as quoted in Newman et al. (2013b) by fitting a Hernquist profile with the same half-light radius to the best-fit dPIE profile, which yields $M_{\rm gal} = 2.1 \times 10^{12} M\odot$ and $h = 28.5$ kpc.

Because we do not directly model rapid galaxy formation and feedback in our simulations, we restrict our analysis to the late-time results of contraction, after most of these effects have subsided in massive galaxies. Each simulation was analyzed after reaching dynamical equilibrium, such that the density profile was no longer evolving. This occurred within ~ 5 Gyr for all cases except the "compact" SIDM Milky Way, which underwent core collapse and showed a slowly increasing core density until we stopped the simulation after 10 Gyr.

[3] We map the MN disk parameter to quoted exponential disk scale lengths R_d by requiring that the half-mass radii are equal. This implies $a \simeq 1.25 R_d$ for the range of parameters we explore.

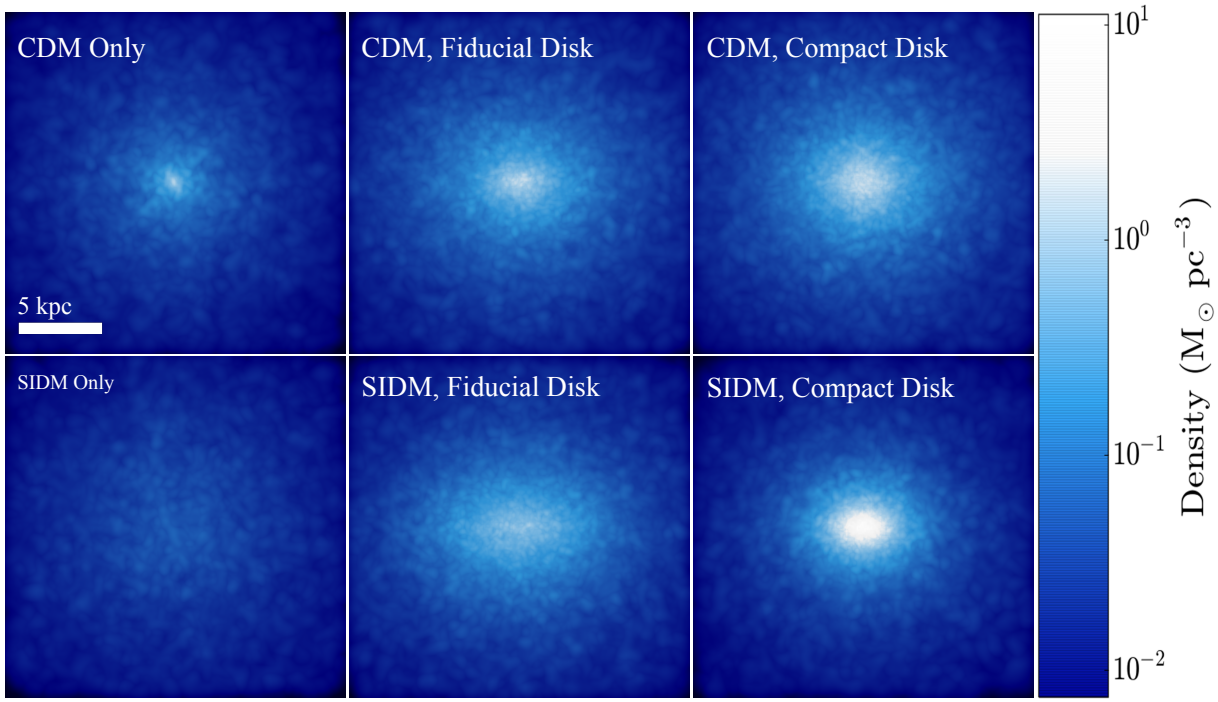

Figure 3.2: Edge-on vizualizations of the dark matter density of an idealized Milky Way sized halo formed with CDM (top) and SIDM (bottom). Images along the left edge are dark-matter only runs. The middle panels show the dark matter after the growth of a disk like the Milky Way. The far right panel shows the dark matter after the growth of a compact disk (see Table 1). As expected, the SIDM-only simulation has a much lower central density than the CDM-only case. When a Milky Way-like disk is imposed, both CDM and SIDM halos contract to similar overall central densities, but the SIDM halo tracks the shape of the disk potential more closely than CDM owing to its isothermal velocity distribution. The compact disk case drives core-collapse in the SIDM simulation, and thus results in an even higher core density than in the contracted CDM run.

3.6 Results

3.6.1 Milky Way Halos

The setup for the Milky Way analogue simulations is shown in the left column of Figure 3.1. The black dotted line shows the circular velocity curve ($V_{\rm c}(r) = \sqrt{GM(<r)/r}$) for our CDM-only run (equivalent to the initial conditions) and the solid black line shows $V_{\rm c}(r)$ for SIDM-only run, which is noticeably less dense in the center owing to SIDM core formation (e.g., Rocha et al., 2013). The colored lines show the implied in-plane circular velocities

($\sqrt{\mathrm{r}\frac{\mathrm{d}\Phi}{\mathrm{dr}}|_{\mathrm{z}=0}}$) for the imposed Extended, Fiducial, and Compact Disk potentials. These show that the disk potential is dominant in our compact and fiducial runs. Our goal is to explore the halo back-reaction to the growth of each of these components.

The middle column of Figure 3.1 shows the dark matter density profiles for all simulations. The solid lines correspond to the SIDM model and dotted lines to the CDM model. The gray curves are the dark-matter only runs while the colored lines show what happens after the potentials are grown. For reference, the bottom panel plots the ratio of dark matter density in SIDM to CDM as a function of radius for each set of runs.

As expected, both CDM and SIDM halos contract in response to galaxy potential growth [4]. The relative differences are enlightening. While the dark-matter-only simulations are quite distinct between the cuspy CDM run and the cored SIDM within ~ 3 kpc, the dark matter profiles in the Fiducial Disk runs are almost identical down to the resolving limit. Specifically, the SIDM halo has responded more to the imposed potential than the CDM halo and this has driven the two profiles to a very similar end state. We only begin to see the formation of an SIDM core within ~ 1 kpc, which is similar to the Milky Way core size measured in Portail et al. (2016). The Extended Disk runs, which impose a less severe potential, have maintained something closer to the original differences, with SIDM beginning to roll off towards a core within ~ 3 kpc, but the differences between the SIDM and CDM are less severe than in the DM-only case (which disagree at 5 kpc). Finally, the Compact Disk has produced a dramatic change: the SIDM halo is now *more dense* than CDM at small radii, with a very cuspy distribution $\rho \sim r^{-2.5}$ at $r \sim 2$ kpc. This is a result of core-collapse: the compact disk potential has heated the dark matter to such an extent that it is now hotter in the core than in the outer part. The SIDM particles are conducting heat outwards, resulting in a loss of core pressure and subsequent mass inflow.

[4]We have confirmed that our CDM runs generally adhere to the expectations of standard Blumenthal et al. (1986) contraction

The SIDM phenomenology is clarified in the right panel of Figure 3.1, which shows the velocity dispersion profile of the dark matter in each run. The two SIDM simulations with clear constant-density core behavior (DM-only and Extended Disk) are seen to have well-established isothermal velocity distributions at small radii. In these cases, the SIDM halos are hotter in their cores and colder in their outer regions than their CDM counterparts. This is exactly the situation that leads to heat transfer from the outside in. The same effect is seen, though much more mildly, in the Fiducial Disk case. In the Compact Disk runs, even the CDM halo is hotter in the core than in the outer part. Such a declining velocity dispersion profile is subject to outward heat flow in the SIDM simulation, and this drives core collapse.

We show in Section 3.6.3 that the resultant density profiles are well explained by the analytical predictions presented in Kaplinghat et al. (2014a, 2015), with the exception of the Compact Disk. However this is to be expected, given the gravothermal core collapse occurring in the Compact Disk, which violates the assumption of isothermality the model is based on.

Figure 3.2 displays visualizations of the dark matter in three pairs of our simulations, with CDM runs shown along the top and SIDM along the bottom. The left row shows the dark-matter only versions of each simulation. The middle and right rows show resultant dark matter distributions after the growth of our Fiducial and Compact disks, oriented such that the disks are seen edge-on. These results emphasize that the shapes of the SIDM halos have been altered substantially by the formation of the disk, mirroring the baryonic potential much more closely than the CDM cases within 10 kpc.

3.6.2 LSB and Elliptical Halos

Figure 3.3 shows the density profiles and initial rotation curves of our elliptical and LSB halos. In the upper-left panel, we see that the elliptical halo is baryon-dominated within ~ 5 kpc, and consequently the density profiles (lower-left panel) show significant contraction. Again we see minimal difference between the final SIDM and CDM halos, with no SIDM core resolved. This is not surprising given our results from 3.6.1; denser galaxies will have greater impacts on their host halos and inhibit SIDM core formation. We also display the total (DM + baryons) density profiles in the lower-left panel of Figure 3.3, as well as an r^{-2} power-law for comparison. As a result of contraction, both simulations have power-law slopes of $\alpha = -2$ around 3 kpc, and slightly steeper outside this region. This places our simulations in agreement with observations of elliptical galaxies (Gavazzi et al., 2007; Auger et al., 2010). In short, because they are centrally baryon dominated, predictions for SIDM halos are largely the same as the CDM case for elliptical galaxies.

Our LSB-analogue simulations, however, do exhibit differences between CDM and SIDM runs. The right panel of Figure 3.3 demonstrates that the LSB disk has very little effect on our dark matter halos: the CDM halo undergoes barely any contraction, and the SIDM halo still displays a central core. This makes sense in light of our previous results that massive and centrally concentrated baryon densities generate the largest impacts on both SIDM and CDM halos. The diffuse nature of low-surface-brightness galaxies implies that their baryons have little effect on the host dark matter halos. Thus, these systems are the best laboratories to investigate dark matter self-interaction possibilities.

3.6.3 Analytic Model

In this section, we compare the results of our simulations to the analytic model presented in Kaplinghat et al. (2015). In this model, the dark matter is assumed to behave as an

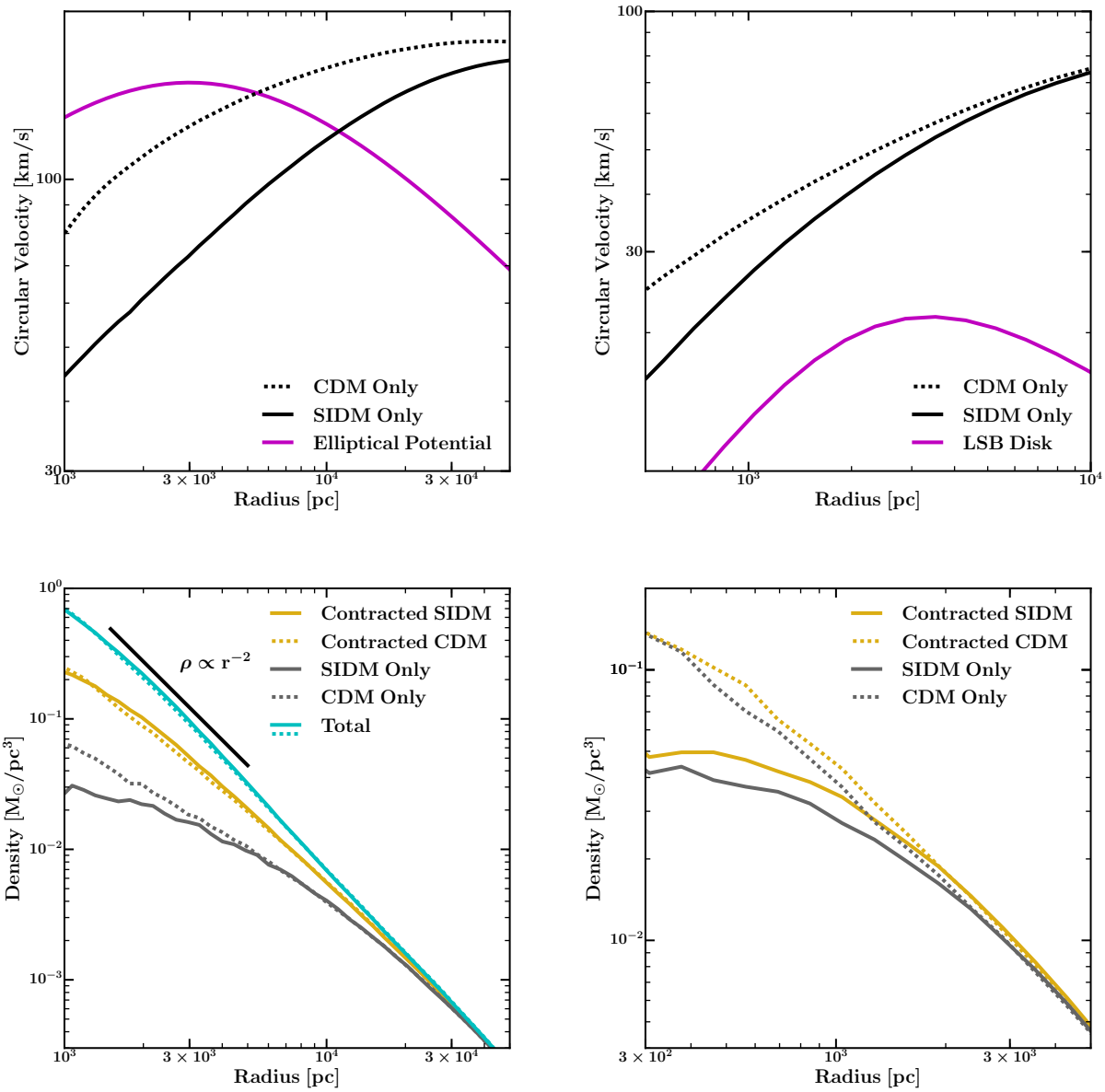

Figure 3.3: Initial rotation curves and final DM differential density profiles for our elliptical and LSB galaxy simulation simulated in both CDM and SIDM. *Left:* Elliptical Simulations. The top panel shows the rotation curves for our CDM and SIDM halos as well as for the added Hernquist potential, displaying how the halo becomes baryon-dominated within 5 kpc. The bottom panel shows the response of the halos to the added potential; as in the MW disk above, there is very little difference between the two contracted halos. We also include the total (DM plus galaxy potential) density profiles in cyan, and an r^{-2} power-law for comparison. *Right:* LSB simulations. The top panel shows the rotation curves for the initial CDM and SIDM halos along with the central disk potential, which contributes far less to the central mass and density of these halos. The lower panel shows that this relatively shallow baryonic potential has a much smaller impact on the host halo; there is very little difference between the initial and contracted CDM halos. The SIDM halo contracts slightly more, but still retains a core of lower density than the initial CDM halo.

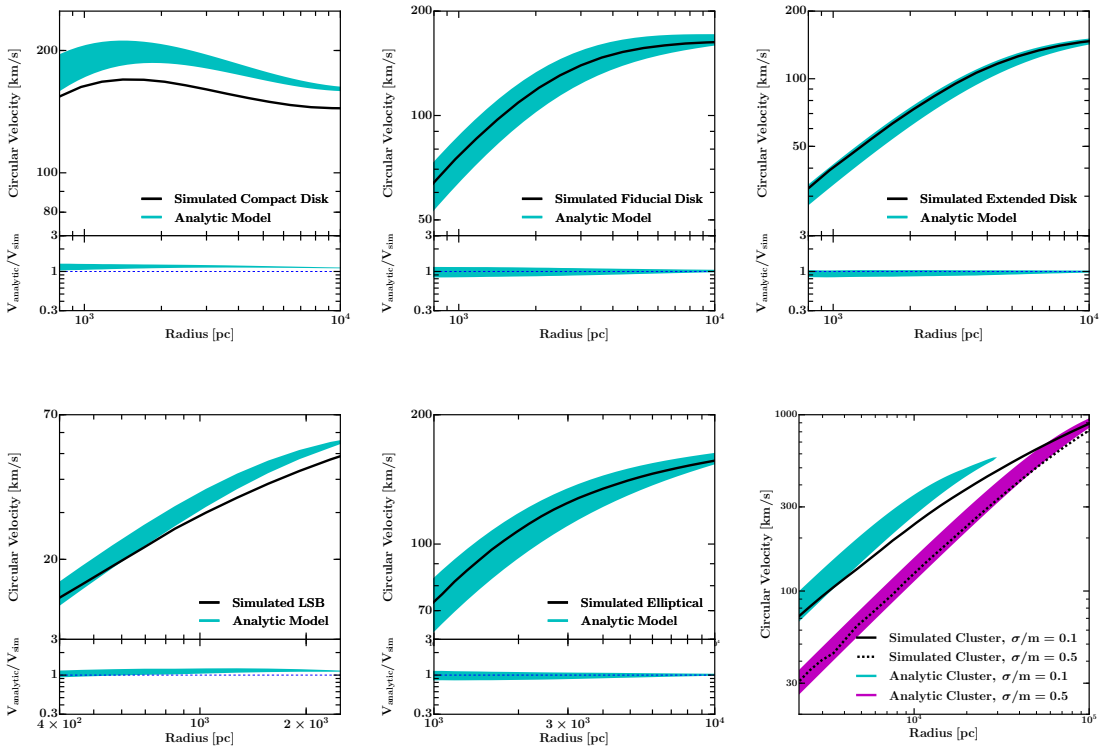

Figure 3.4: Comparison between circular velocities of our analytic model and simulations. Generally the analytic model is in agreement with simulations, with the notable exception of the Compact Disk. This is because of the core-collapse occurring in the Compact Disk simulation, causing greater central densities than predicted by our model, leading to higher circular velocities in the halo center.

isothermal gas within a radius r_1, defined as the radius where particles interact at least once in the age of the system: $\Gamma(r_1)\, t_{\rm age} = 1$ or

$$\rho(r_1)\ (\sigma/m)\ (4/\sqrt{\pi})\sigma_{v0}\, t_{\rm age} = 1. \tag{3.3}$$

Here σ/m is the SIDM cross-section per unit mass, σ_{v0} is the radial velocity dispersion in the core and the factor of $4/\sqrt{\pi}$ accounts for the average relative velocity for Maxwellian distribution. $t_{\rm age}$ is the time period over which the self-interactions have been operating. We take this to be the time after the stellar component is fully in place to be consistent with the boundary conditions imposed.

The analytic model we use is spherically symmetric. To apply it to our simulated galaxies, we follow the procedure of Kaplinghat et al. (2014a) and construct a new *spherical* mass profile for the baryons $M_{\rm baryon}(r)$ by including all the mass in all the stars within a sphere of radius r. Inside r_1 the SIDM density is set by hydrostatic equilibrium, giving

$$\nabla^2 \ln \rho_{\rm DM}(r) = -\frac{4\pi}{\sigma_{v0}^2} {\rm G}\left[\rho_{\rm DM}(r) + \rho_{\rm baryon}(r)\right], \tag{3.4}$$

where $\rho_{\rm baryon}$ is the density profile corresponding to the mass profile $M_{\rm baryon}$. At r_1, as boundary conditions, the isothermal mass and density profiles (from solving the hydrostatic equation above) are required to match the CDM halo profile after adiabatic contraction (essentially the $z = 0$ CDM profile in our simulations).

In all cases, we find two islands of solutions in the central density−−dispersion plane, for the same boundary condition Kaplinghat et al. (2014a). We choose the lower density island because it matches the simulated profiles well; the higher density (with smaller cores) island could be the analog of core collapsed solutions. Typically, the 1-d central dispersion σ_{v0} values picked out by the two solutions are very close. The value of σ_{v0} value is set by the matching and it recovers the correct inner dispersion seen in the simulations.

Figure 3.4 shows circular velocity profiles for our contracted SIDM halos along with the analytic predictions for rotation curves. Here the cyan bands indicate the range of solutions which match $\rho(r_1)$ and $M(r_1)$ within 5%. We chose 5% for two reasons. One, it shows the sensitivity of the inner density profile of SIDM profiles to the matching (boundary) conditions. Two, the simulated SIDM only and CDM only halos are not identical and allowing for a small slop in the matching makes us less sensitive to their differences.

The analytic solutions and the simulated halo profiles generally agree well, with the notable exception of the Compact Disk "Milky Way" case. The analytic mass profile for this case is systematically higher, even though the non-trivial shape of the mass profile (see Figure 3.1) is captured well by the analytic profile. The analytic profile is very sensitive to the value of σ_{v0}. For the Fiducial and Extended disks, the matching correctly infers the SIDM central velocity disperison $\sqrt{3}\sigma_{v0}$ to be 250 km/s and 210 km/s (see Figure 3.1) and the analytic solution does a good job of describing the simulated mass profiles. For the Compact disk case, the inferred velocity dispersion is close to 290 km/s. However, in the Compact disk simulation, the velocity dispersion rises this high only within about 2 kpc, while r_1 is about 14 kpc. As Figure 3.1 shows, the dispersion profile for the Compact disk case is increasing toward the center due to core collapse (see Section 3.6.1), so the mismatch between the simulated profile and the analytic model is not surprising.

Given the overall consistency of the analytic model (equilibrium) predictions with our simulated halo profiles when core collapse is not seen, we are confident that the Kaplinghat et al. (2015) model predicts the SIDM halos in realistic galaxies and clusters well.

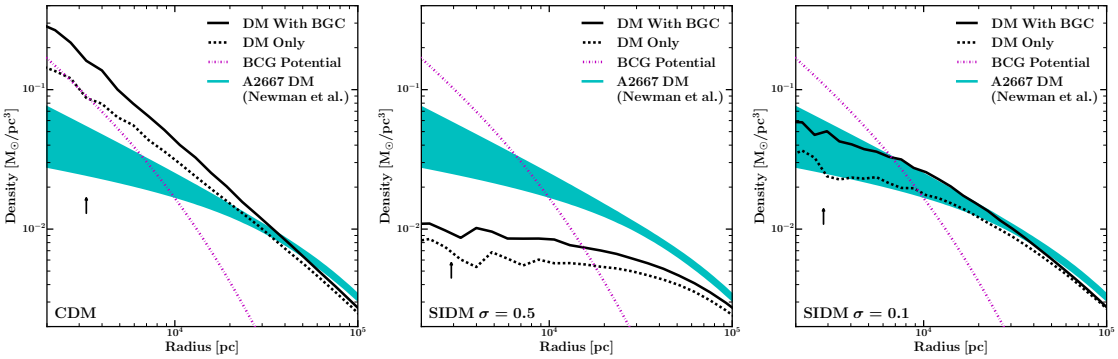

Figure 3.5: Density profiles for our simulations of cluster Abell 2667 along with the inferred dark matter density profile from Newman et al. (2013a). Even before contraction, our CDM halo (left) is too dense and the contracted SIDM profile with $\sigma/m = 0.5$ cm^2 g^{-1} (center) is not dense enough to reproduce the observed density profile. Our contracted SIDM halo with $\sigma/m = 0.1$ cm^2 g^{-1} (right), however, matches the observed density of Abell 2667 well, in agreement with the predictions of Kaplinghat et al. (2015).

3.7 Cluster Limits

We also simulate an analog of Abell cluster 2667. Our setup is described in the bottom row of Table 3.1. The virial mass and concentration of the initial NFW halo match the observations of Newman et al. (2013b), however they model the density of the BCG as a dual psuedo-isothermal elliptical profile (dPIE):

$$\rho = \frac{\rho_0}{1 + r^2/(r_{\rm core}^2)(1 + r^2/r_{\rm cut}^2)}$$

In order to model this in our simulations we use a Hernquist (1990) sphere with the same half-mass radius as the measured profile, and use a least-squares fitting method to obtain a best-fit total mass. This is necessary because dPIE profiles exhibit central cores, while Hernquist profiles have central $1/r$ cusps, so a Hernquist distribution with the same mass and half-mass radius as a dPIE distribution will be less dense at all radii outside of the core radius, significantly reducing the contraction effect we wish to investigate. We grow the

central potential over the course of 2 Gyr, and allow the halo to evolve for 3 Gyr after this, running for 5 Gyr total.

Figure 3.5 shows the density profiles of our simulations; uncontracted densities are plotted as black dashed lines, while the contracted halos are solid black. We also include a vertical arrow to indicate the smallest converged radius of our simulations, as defined in Elbert et al. (2015). We plot the inferred Cored NFW dark matter density profile measured by Newman et al. (2013a) as a cyan band, though we note that the generalized NFW fits Newman et al. (2013a) reported are not significantly different. Finally, the effective density of the BCG Hernquist profile is shown in magenta. The leftmost figure displays our CDM simulations. Even before contraction, the initial NFW profile is too centrally dense to match observations by a factor of ~ 1.5 at the limits of our resolution. Adiabatic contraction increases the density by another factor of 1.5, further worsening this discrepancy. If instead we assume the dark matter is self interacting with a cross section of 0.5 cm^2 g^{-1} we obtain the densities in the center plot. In this case, we see that such a cross-section results in a halo that is underdense by more than a factor of 3 in its center, and still below the observed limits at 100 kpc in our SIDM-only simulation. While baryonic contraction does increase the DM density, it is not nearly strong enough to completely alleviate the problem. Indeed, over most of our resolved region the contracted halo is only $20-30\%$ higher than the SIDM-only simulation.

This result may seem surprising at first given that the baryons are important in the center in terms of their dynamical mass. However, the key point is that the DM halo is so massive that its velocity dispersion dwarfs the stellar potential. In this respect, the contraction of the SIDM halo is different from the adiabatic contraction of CDM halos; applying the Blumenthal et al. (1986) adiabatic contraction formula would result in a halo profile much denser than the simulated result. The isothermal equilibrium solution, on the other hand, is a good match to the simulated halo profile.

We also simulate Abell 2667 with a cross-section of 0.1 $\mathrm{cm}^2\ \mathrm{g}^{-1}$; our results are plotted in the right-panel of Figure 3.5. In the SIDM only case, the density is near the lower-limits of the Newman et al. (2013a) data. After contraction has been accounted for, however, 0.1 $\mathrm{cm}^2\ \mathrm{g}^{-1}$ is consistent with observations, bordering the upper limits of the Newman et al. (2013a) measurement, and we estimate that a cross section of 0.2 $\mathrm{cm}^2\ \mathrm{g}^{-1}$ will border the lower limits. Our estimates are in agreement with the results of Kaplinghat et al. (2015), who find cross sections of $0.1 - 0.2\ \mathrm{cm}^2\ \mathrm{g}^{-1}$ (assuming $t_{\mathrm{age}} = 5$ Gyr) by fitting to the Newman et al. (2013a) data using the analytic model (described previously). This implies that a SIDM model with a cross section that falls from about 1 $\mathrm{cm}^2\ \mathrm{g}^{-1}$ on dwarf galaxy scales to about 0.1 $\mathrm{cm}^2\ \mathrm{g}^{-1}$ on cluster scales can resolve the small-scale puzzles (Kaplinghat et al., 2015; Elbert et al., 2015; Vogelsberger et al., 2014; Zavala et al., 2013), while also matching density profile constraints in clusters.

3.8 Conclusions

In this work we have investigated the combined effects of baryonic gravitational potentials and dark matter self-interactions on dark matter halos using idealized simulations of dark matter halos with galactic potentials. By simulating halos of various sizes with many different potentials we have found:

- SIDM halo shapes are not inherently more resilient to effects from baryons than their CDM counterparts. For a Milky Way halo hosting a Milky Way analogue disk, the SIDM halo is more compact along the disk axis than its CDM equivalent in agreement with the prediction of Kaplinghat et al. (2014a). For an elliptical galaxy, whose stellar potential is markedly more spherical, we expect the SIDM halo to be correspondingly more spherical.

- Halos that host substantial baryonic populations display few differences in spherically-averaged density profiles between CDM and SIDM models on observable scales. Even extended baryon populations can contract halos with respect to SIDM-only simulations, though these systems retain potentially observable constant-density cores and are less dense than CDM. In extreme cases, we find that potentials from dense baryonic structure can cause SIDM halos to core-collapse and become denser than their CDM counterparts.

- Halos that host concentrated stellar populations may display few differences in spherically-averaged density profiles between CDM and SIDM models on observable scales. Even extended stellar populations can contract halos with respect to SIDM-only simulations, though these systems retain potentially observable constant-density cores and are less dense than CDM. In extreme cases, we find that potentials from dense baryonic structure can cause SIDM halos to core-collapse and become denser than their CDM counterparts.

- The densities of our contracted halos are in good agreement with the analytical predictions in Kaplinghat et al. (2014a, 2015), with the exception of the core-collapsing Compact Disk because it no longer obeys the isothermal assumption of the model. In particular, we show that the spherically-averaged density profiles are well approximated by the simple model in Kaplinghat et al. (2015), which has an isothermal core and an undisturbed CDM outer profile.

- We simulated a cluster halo for 3 Gyr after the brightest cluster galaxy was fully in place to test against the mass measurements for A2667 Newman et al. (2013a). Our simulated CDM halo was denser than the observed central profile for A2667. On the other hand, SIDM with $\sigma/m \simeq 0.5$ cm^2 g^{-1} was too low in density compared to the measurements. The choice of $\sigma/m \simeq 0.1$ cm^2 g^{-1} was in much better agreement with the measured normalization (and inner slope) of the A2667 density profile. Larger

values like $\sigma/m \simeq 0.5$ cm^2 g^{-1} are ruled out, even allowing for a factor of 2 uncertainty in the age of the halo. These conclusions are in substantial agreement with the detailed analysis of seven clusters (Newman et al., 2013a) by Kaplinghat et al. (2015), which found a average value of $\sigma/m \simeq 0.1$ cm^2 g^{-1} on cluster velocity scales for an assumed age of 5 Gyr.

Based on these results, an ideal scale to investigate possible DM self-interactions appears to be the dwarf galaxy scale with halo masses 10^{10-11} $M\odot$ scale, as they will have the largest interaction cross sections and the least contracted halos. However, these are precisely the halos expected to be most vulnerable to stellar feedback (Pontzen & Governato, 2012; Governato et al., 2012; Di Cintio et al., 2014; Oñorbe et al., 2015). Ongoing work (Vogelsberger et al., 2014; Fry et al., 2015; Robles et al., in prep) is investigating the effects of feedback on the SIDM halos and their results suggest that dwarfs with stellar masses $M_\star \lesssim 10^6 M\odot$ will have density profiles indistinguishable from the predictions of the dark matter-only simulations. This suggests that the faintest dwarf spheroidals provide excellent laboratories constraining SIDM models.

For halo masses much larger than 10^{11} $M\odot$ that host a large stellar disk or bulge, as the inner halo becomes isothermal the SIDM halo retains the high densities created by adiabatic contraction following the formation of the disk. Thus, in Milky Way sized halos the CDM and SIDM halos densities are very similar beyond about a kpc, in marked contrast to the dark-matter-only predictions. As predicted by Kaplinghat et al. (2014a), the self-interactions also force the SIDM halo to be more compact along the stellar disk axis. We find that the SIDM halo in the inner region of Milky Way analogs is more compact along the galactic disk axis than the CDM halo. Thus, it may be possible to use the shape of the dark matter halo in the inner regions of large spiral galaxies to provide a sharp test of the SIDM paradigm.

The predictive cross-talk between the dark matter and baryons in the SIDM models leads to a large diversity of halo profiles and halo shapes. This cross-talk is purely gravitational and the result of the dark matter becoming isothermal in the inner parts of the halos. This is fully explained by simple equilibrium models. The prospects for using these concrete predictions of the SIDM paradigm to rule in or rule out SIDM in the near future are excellent.

Chapter Acknowledgments

The authors thank Michael Boylan-Kolchin and Hai-Bo Yu for valuable discussions. ODE, ASG, and JSB were supported by the National Science Foundation (grants PHY-1520921, AST-1518291, and AST-1009973) and by NASA through HST (GO-13343) awarded by the Space Telescope Science Institute (STScI), which is operated by the Association of Universities for Research in Astronomy (AURA), Inc., under NASA contract NAS5-26555. MK is supported by NSF grant PHY-1620638. Support for SGK was provided by NASA through Einstein Postdoctoral Fellowship grant number PF5-160136 awarded by the Chandra X-ray Center, which is operated by the Smithsonian Astrophysical Observatory for NASA under contract NAS8-03060.

This work also made use of `Astropy`, a community-developed core Python package for Astronomy (Astropy Collaboration et al., 2013), `matplotlib` (Hunter, 2007), `numpy` (van der Walt et al., 2011), `scipy` (Jones et al., 2001–), `ipython` (Perez & Granger, 2007), and NASA's Astrophysics Data System.

Chapter 4

Counting Black Holes: The Cosmic Stellar Remnant Population and Implications for LIGO

4.1 Chapter Abstract

We present an empirical approach for interpreting gravitational wave signals of binary black hole mergers under the assumption that the underlying black hole population is sourced by remnants of stellar evolution. Using the observed relationship between galaxy mass and stellar metallicity, we predict the black hole count as a function of galaxy stellar mass. We show, for example, that a galaxy like the Milky Way should host millions of $\sim 30\ M\odot$ black holes and dwarf satellite galaxies like Draco should host ~ 100 such remnants, with weak dependence on the assumed IMF and stellar evolution model. Most low-mass black holes ($\sim 10M\odot$) typically reside within massive galaxies ($M_\star \simeq 10^{11} M\odot$) while massive black holes ($\sim 50\ M\odot$) typically reside within dwarf galaxies ($M_\star \simeq 10^9 M\odot$) today. If roughly 1% of black

holes are involved in a binary black hole merger, then the reported merger rate densities from Advanced LIGO can be accommodated for a range of merger timescales, and the detection of mergers with $> 50\ M\odot$ black holes should be expected within the next decade. Identifying the host galaxy population of the mergers provides a way to constrain both the binary neutron star or black hole formation efficiencies and the merger timescale distributions; these events would be primarily localized in dwarf galaxies if the merger timescale is short compared to the age of the universe and in massive galaxies otherwise. As more mergers are detected, the prospect of identifying the host galaxy population, either directly through the detection of electromagnetic counterparts of binary neutron star mergers or indirectly through the anisotropy of the events, will become a realistic possibility.

4.2 Introduction

With the first detection of gravitational waves, the Laser Interferometer Gravitational-Wave Observatory (LIGO) simultaneously confirmed a fundamental prediction of General Relativity and discovered the first known binary black hole (BBH) merger (Abbott et al., 2016d). This first gravitational wave event, GW150914, appears to have been caused by the merger to two fairly massive ($\sim 30M\odot$) black holes. Subsequent detections of a BBH mergers (GW151226 and GW170104, Abbott et al., 2016c, 2017) and a candidate BBH event (LVT151012, Abbott et al., 2016a) have allowed more robust estimates of the local BBH merger rate density and have confirmed the existence of black holes involved in these mergers with masses that range from 7.5 to 36 $M\odot$.

As the field now pivots from gravitational wave discovery to gravitational wave astronomy, there are number of questions we hope to explore in more detail. One basic question is the origin of these massive black holes. Heavy ($\gtrsim$ 30 $M\odot$) black holes are expected to exist as the result of stellar evolution (e.g. Spera et al., 2015; Belczynski et al., 2010, and

references therein), and have been predicted to dominate the LIGO signal (e.g. Belczynski et al., 2016b). However, the possibility that the GW150914 event was due to primordial black holes (that would constitute some part of the dark matter) has also been advanced (Bird et al., 2016; Cholis et al., 2016; Carr et al., 2016; Inomata et al., 2016).

Ab initio computation of the BBH merger rate (of stellar remnants) is currently not possible. This calculation requires inputs from multiple fields including galaxy formation and numerical relativity. In this work, we outline a simple way to compute the BBH merger rate for stellar remnant black holes that allows one to assess the uncertainties in the various required ingredients in a transparent manner. The key idea is that we have a good empirical understanding of the overall galaxy number density, stellar ages and metallicities as a function of galaxy mass, and estimates of the initial mass function of stars that formed in these galaxies. Using these ingredients, together with the current generation of stellar evolution codes, we can provide a grounded estimate of the global distribution of black holes as a function of black hole mass and galaxy stellar mass. With this as a starting point, we are able to quantify the astrophysical parameters needed to produce the observed BBH merger signals observed. For example, the LIGO collaboration has reported a global "event-based" merger rate of $\mathcal{R} = 55^{+185}_{-46}$ Gpc^{-3} yr^{-1} for binaries more massive than $5\,M\odot$ each (Abbott et al., 2016b,f), and the detection of GW170104 has reduced the range to $12 \leq \mathcal{R} \leq 213$ (Abbott et al., 2017). Below we will demonstrate that such a rate is reasonable with the population of stellar black holes we expect to exist within galaxies in the local universe and we discuss how the host mass of mergers will be a valuable diagnostic for testing scenarios going forward.

Our work is complementary to past work by Belczynski et al. (2016b) and Lamberts et al. (2016), who focus their efforts on understanding the formation of binaries and the details of binary black hole evolution. Both of these papers explicitly focused on the first GW150914 event. Lamberts et al. (2016) concluded that the black holes involved in GW150914 likely

formed in a massive galaxy at $z \sim 1$, but that formation in a dwarf galaxy was also likely possible. Belczynski et al. (2016b) suggested that the black holes likely form in low-metallicity systems. Chatterjee et al. (2017) explored the formation of BBH systems specifically in globular clusters and came to qualitatively similar conclusions.

Important to all of these investigations is the realization that massive black hole formation is suppressed in stellar populations with higher metallicites (Spera et al., 2015; Belczynski et al., 2008). For example, according to the calculations of Spera et al. (2015), a star of mass $\mathcal{M} \simeq 90 M\odot$ will be required to produce a remnant of mass $m_{\rm bh} = 30 M\odot$ if its metallicity is $Z/Z_\odot = -0.5$. A more metal poor star (-1.5) will need to be only $\mathcal{M} \simeq 33 M\odot$ to produce a $30 M\odot$ BH remnant. These expectations, combined with the long merger times often predicted for isolated BBH systems (see Postnov & Yungelson, 2014, and references therein), have led many authors to conclude that the detected BBH merger signals observed by LIGO will be dominated by the mergers of black holes formed in the early universe. However, processes such as the Kozai-Lidov mechanism (Kozai, 1962; Lidov, 1962) may accelerate the merger timescale both in galaxy centers(VanLandingham et al., 2016) and star clusters (Silsbee & Tremaine, 2016; Kimpson et al., 2016) and low-metallicity star formation is ongoing at low-redshifts, especially in low mass galaxies (Ellison et al., 2008; Mannucci et al., 2010; Lara-López et al., 2010), allowing massive BBH systems to form locally and potentially merge quickly enough to detect. We note that spin constraints limit the merging time of GW150914 to be greater than 100 Myr (Kushnir et al., 2016). Given the large uncertainties, we treat the merging time of BBH systems as a free parameter in our analysis, and explore observational means to constrain the timescale.

Our work is organized as follows: In §4.3 we describe our approach. In §4.4 we estimate the local number density of black holes as a function of black hole mass using the local mass-metallicity relation and stellar mass function. We examine how these black holes are distributed among galaxies of a given mass in §4.4.1 and work out the global number density

in §4.4.2. We move from the total number density to merger rate densities in §4.5 and discuss how by localizing event rates by host galaxy masses we can begin to constrain more details of BBH merger scenarios in §4.5.1. We summarize and conclude in §4.6.

4.3 Our Approach

Before detailing our predictions in the next section, we here provide an overview of our basic approach.

Our calculation proceeds in two steps. First we determine the cosmic number density of stellar remnants, $n_{\rm bh}$, using empirical measurements of the galaxy population (§3). Next, with this empirically-grounded number density in hand, we calculate binary black hole merger rate densities using two simple parameters that quantify our ignorance of binary formation and binary evolution (§4). Specifically, we introduce a dimensionless parameter $\epsilon \leq 1$ that captures the complicated physics of binary system formation and binary remnant survival. We also introduce a characteristic merger timescale, τ, that parameterizes our uncertainty in binary black hole evolution and the distribution of times it takes for a binary pair to merge after formation. In principle, any merger timescale distribution can be mapped to this characteristic timescale τ.

As we show below, $n_{\rm bh}$ is fairly robust to uncertainties. The larger uncertainties are in the physics of binary formation and evolution encapsulated in ϵ and τ. We show that the observed LIGO signals can be readily explained with reasonable values for both of these parameters and make predictions for future observations of black hole and neutron star merger rates that provide a means to constrain the physics they encapsulate. We also explore and quantify the degeneracies between ϵ and τ and describe how determining the galaxy host mass distribution for mergers could be a way to break these degeneracies.

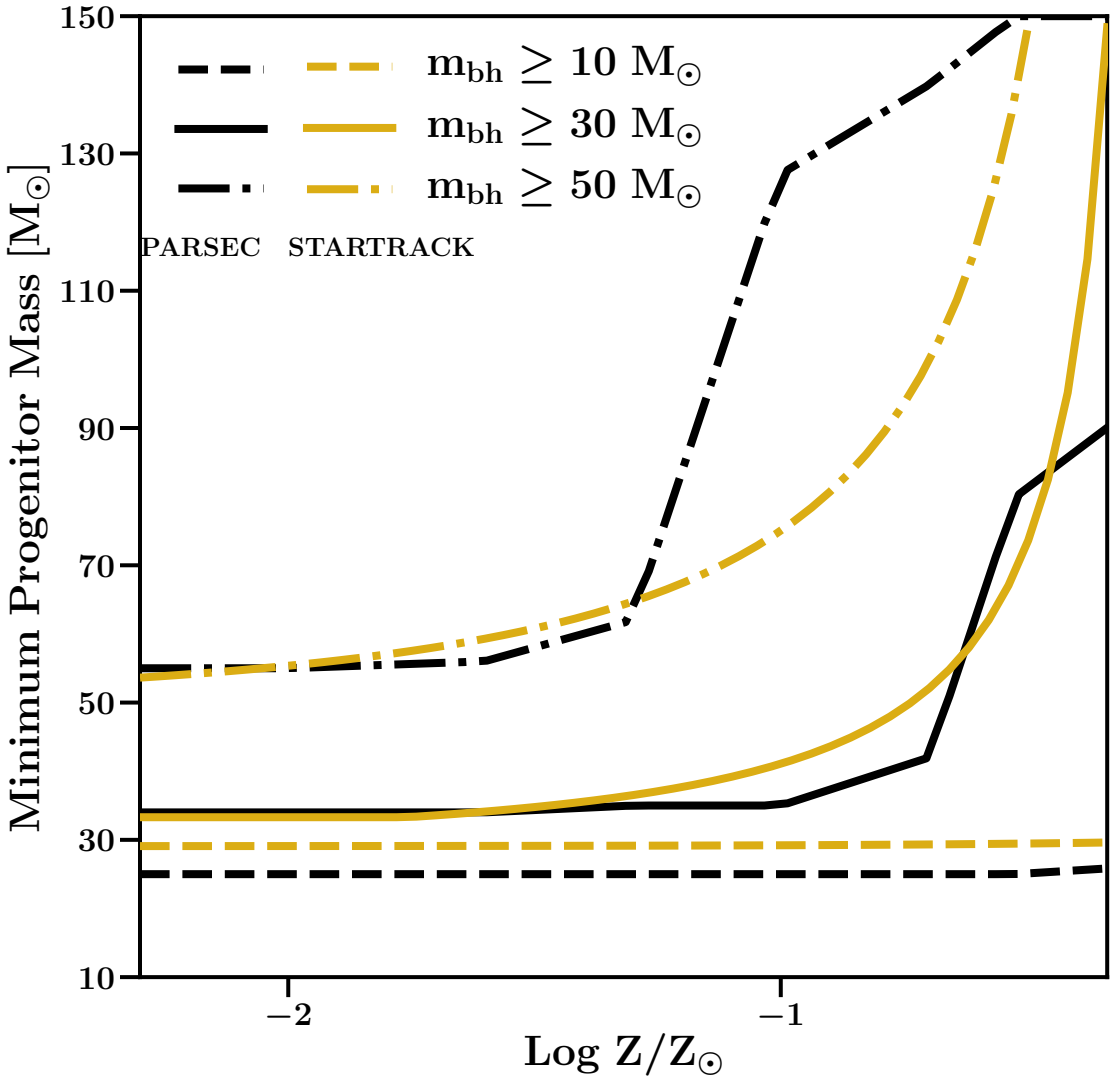

Figure 4.1: The minimum stellar masses to produce a remnant black hole more massive than $m_{\rm bh} = 10, 30$, and $50 M\odot$ are shown as a function of the star's metallicity Z for two different stellar evolution tracks.: `PARSEC` (Spera et al., 2015, shown in bold black) and `StarTrack` (Fryer et al., 2012, shown in cyan). Both estimates are in reasonable agreement, though we note that the Fryer et al. (2012) model fits are extrapolated to 50 solar masses.

4.4 Black hole number density predictions

In this section, we discuss the global number density of black holes at the present time and their distribution as a function of the galaxy stellar mass. In §4.4.1 we work out the expected specific black hole frequency as a function of black hole mass and galaxy mass. In §4.4.2 explore the implied cosmic density of black holes. These determinations will ground us as we move forward to estimate merger rates.

4.4.1 Black Hole Populations Within Galaxies

The number of black holes more massive than $m_{\rm bh}$ that exist within a galaxy will depend on the number of massive stars previously formed in that galaxy with an initial mass larger than some minimum value, $\mathcal{M}_{\rm min}(m_{\rm bh}, Z)$. The minimum mass of a star required to produce a remnant black hole of some mass $m_{\rm bh}$ is expected to be a strong function of stellar metallicity Z owing to mass loss from stellar winds. Figure 4.1 plots $\mathcal{M}_{\rm min}$ as a function of Z for three example black hole remnant masses $m_{\rm bh} > 10, 30$,and $50M\odot$, as determined by stellar evolution codes `PARSEC` (Spera et al., 2015, black) and `StarTrack` (Fryer et al., 2012, blue). Both calculations give similar results, especially at low metallicities[1]. We see that for high metallicities ($Z \gtrsim -1.5$), a very large stellar progenitor ($\mathcal{M} \gtrsim 90M\odot$) will be required to produce the massive black holes of the type that have been observed in mergers by LIGO. Lower metallicity populations require less extreme progenitors. We will adopt the `PARSEC` results as our fiducial choice below.

With $\mathcal{M}_{\rm min}$ in hand, we can determine the total number of black holes more massive than $m_{\rm bh}$ that have ever formed, $N_{\rm bh}(> m_{\rm bh})$, within a galaxy of mass $M_\star$ and a total number of stars $N_\star(M_\star)$ by integrating over the stellar IMF $\xi(\mathcal{M})$ and the metallicity distribution

[1]The largest discrepancy between the models is at $m_{\rm bh} > 50M\odot$, which is perhaps not unexpected since the fits from Fryer et al. (2012) are extrapolations at this mass range.

function (MDF) of stars expected for a galaxy of that mass $\mathcal{P}(Z, M_\star)$:

$$N_{\rm bh}(> m_{\rm bh}, M_\star) \\ = N_\star(M_\star) \int \mathcal{P}(Z, M_\star) \int_{\mathcal{M}_{\rm min}(m_{\rm bh}, Z)}^{\mathcal{M}_{\rm u}} \xi(\mathcal{M}')\ d\mathcal{M}' dZ. \tag{4.1}$$

We set the upper limit on the IMF integral at $\mathcal{M}_{\rm u} = 150\ M\odot$, though our results are not strongly sensitive to this choice.[2] The black hole count is normalized by $N_\star(M_\star) = M_\star/\bar{\mathcal{M}}(M_\star)$, where

$$\bar{\mathcal{M}}(M_\star) = \int_{0.08\ M\odot}^{\mathcal{M}_l(M_\star)} \mathcal{M}'\ \xi(\mathcal{M}')\ d\mathcal{M}'. \tag{4.2}$$

For the upper limit $\mathcal{M}_l(M_\star)$, we chose the stellar mass with main sequence lifetime equal to the average stellar age of galaxies of mass $M_\star$ (from Behroozi et al., 2013a, see their Fig. 13). For $\mathcal{P}(Z, M_\star)$ assume that galaxies more massive than $M_\star = 10^9 M\odot$ follow a log-normal distribution in Z, with mean and standard deviation given by Gallazzi et al. (2005). For smaller galaxies, we use the results of Kirby et al. (2013), who measured resolved-star MDFs for 15 individual local dwarf galaxies with stellar masses $M_\star \simeq 10^3 - 10^8 M\odot$. We assume that these individually observed MDFs are representative for galaxies in the dwarf mass range throughout the universe. Finally, for $\xi(\mathcal{M})$ we adopt a Kroupa (2002) IMF for our fiducial calculations. We have also explore the effects of metallicity-dependent IMF (specifically adopting the IMF of Geha et al., 2013) and find that our results are sensitive at the factor of ~ 2 level to this level of variation in the IMF.

Figure 4.2 shows $N_{\rm bh}(M_\star)$ as derived from Equation 1 for three choices of black hole mass: $m_{\rm bh} > 10$, 30, $50 M\odot$. The $m_{\rm bh} > 30 M\odot$ results are shown as squares, color coded according the median metallicity of galaxies at each $M_\star$. Boxes at $M_\star < 10^9 M\odot$ are placed at the

[2]Setting the upper limit to ∞ in the subsequent analysis changes our results by $< 10\%$.

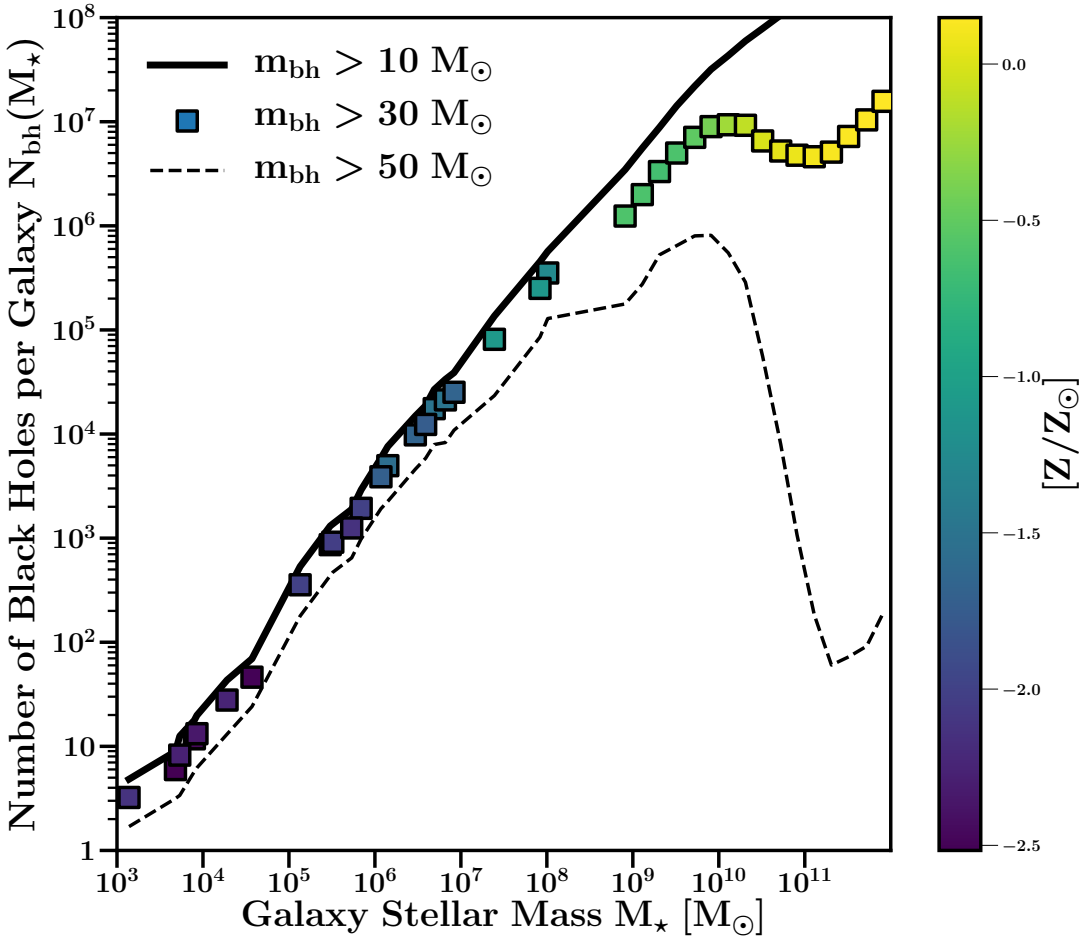

Figure 4.2: The number of remnant black holes per galaxy as a function of galaxy stellar mass, $N_{\rm bh}(M_\star)$, for black holes of mass mass $m_{\rm bh} > 10, 30$, or $50 M\odot$. The squares (corresponding to $30 M\odot$ black holes) are color coded by the median galaxy metallicity. We see that for low metallicities, $N_{\rm bh} \propto M_\star$ in all cases. For the most massive black holes (30, 50 $M\odot$), the relation breaks when galaxies become too metal rich to produce remnants in proportion to their total stellar mass – these black holes form only in the low-Z tail of the distribution. At the highest stellar masses, the relations begin to rise again, when the relation between $M_\star$ and Z becomes flat.

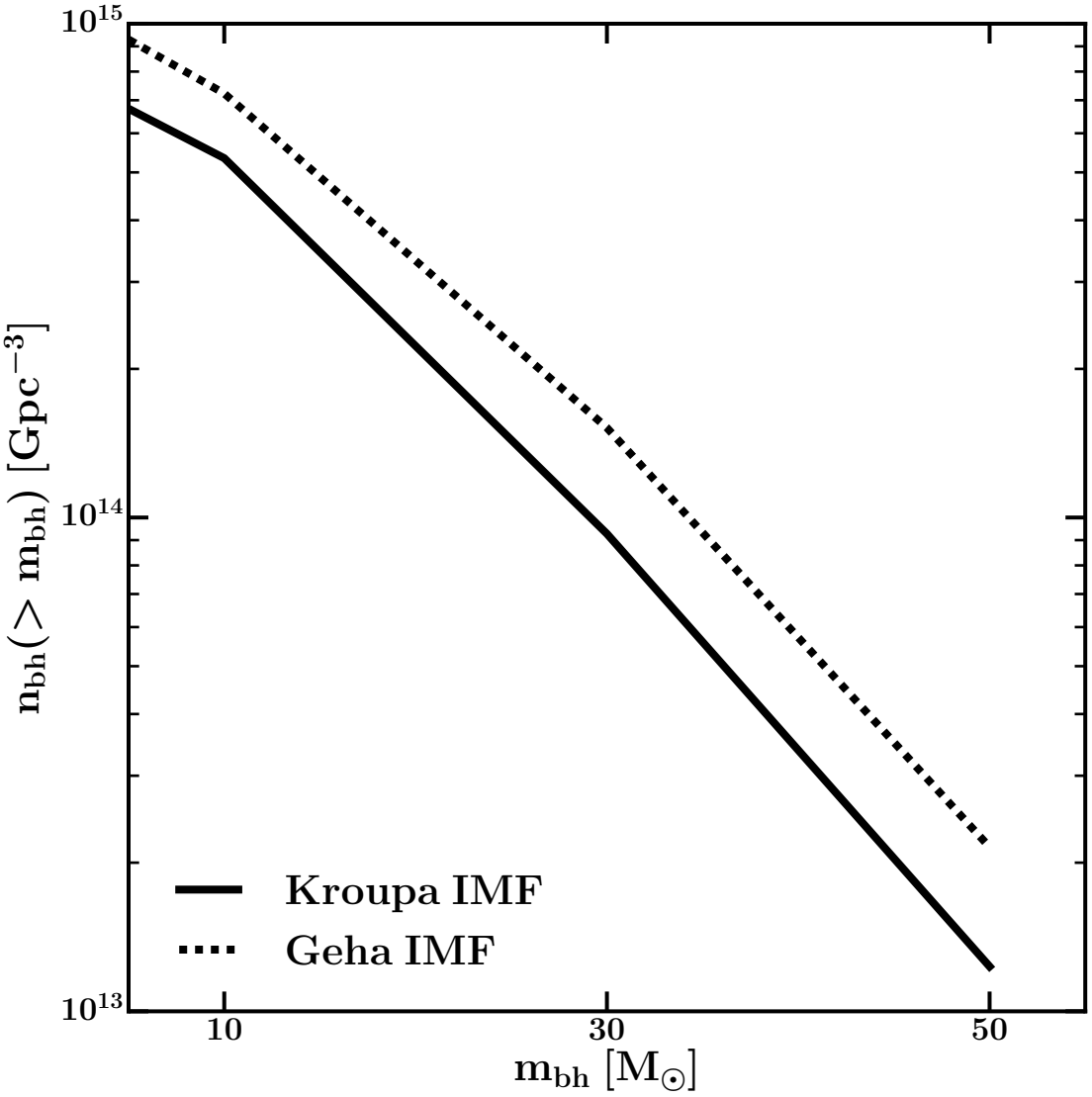

Figure 4.3: Number density of black holes versus black hole mass assuming a Kroupa (2002) or metallicity dependent (Geha et al., 2013) IMF.

stellar masses of the individual galaxies in the Kirby et al. (2013) MDF sample. We see that for galaxies less massive than $M_\star \simeq 10^{10} M\odot$, the number of black holes of all masses scales linearly with galaxy mass, $N_{\rm bh} \propto M_\star$. For example, we find that there should be roughly one $30 M\odot$ black hole per $1000 M\odot$ of stars in a galaxy, at least for smaller galaxies. For the $m_{\rm bh} > 30$ and $50 M\odot$ populations, the linear scaling with $M_\star$ breaks down when galaxies become so metal rich that only the low-metallicity tail of the population can be associated with massive black hole formation. But the black hole counts recover and begin increasing monotonically with stellar mass again once galaxies become massive enough that there is no longer a strong trend between $M_\star$ and Z (at $M_\star \gtrsim 10^{11} M\odot$). Note for the smallest black holes, $N_{\rm bh} \propto M_\star$ for all galaxy masses, as there is very little trend between progenitor mass and remnant mass for $m_{\rm bh} \lesssim 10 M\odot$ (see Figure 1).

4.4.2 Cosmic Black Hole Number Density

In order to obtain the global number density of black holes, $n_{\rm bh}(> m_{\rm bh})$, we integrate $N_{\rm bh}(M_\star)$ over the galactic stellar mass function $\phi(M_\star)$:

$$n_{\rm bh}(> m_{\rm bh}) = \int_{M_{\rm min}}^{\infty} \phi(M_\star)\, N_{\rm bh}(> m_{\rm bh}, M_\star)\; dM_\star. \tag{4.3}$$

We adopt the results of Baldry et al. (2012) for $\phi(M_\star)$ though we have checked that using the stellar mass function from Bernardi et al. (2013) does not change our results significantly. For the minimum mass in the $M_\star$ integral we use $\rm M_{min} = 10^3 M\odot$ and find the number density of black holes is convergent below this galaxy mass.

The solid black line in Figure 4.3 shows the results of this calculation of $n_{\rm bh}$ for our fiducial Kroupa IMF assumption. For comparison, the dotted line shows the result for the Geha metallicity-dependent IMF (Geha et al., 2013). Though the Geha IMF yields slightly more black holes, the factor of ~ 2 offset is not large given the other uncertainties in this calcu-

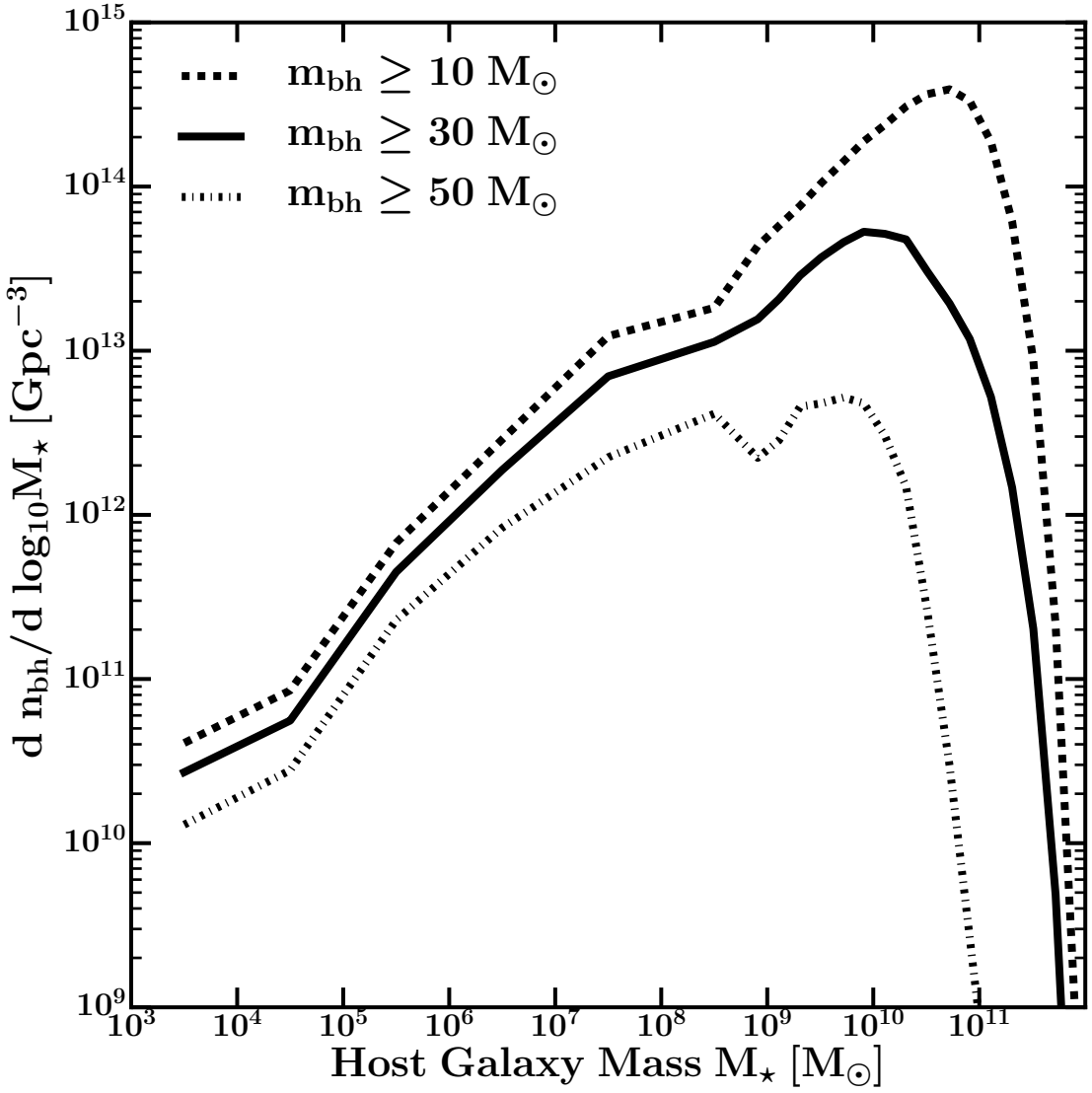

Figure 4.4: The differential number density of black holes per dex in host galaxy mass. Lower mass black holes, $m_{\rm bh} > 10M\odot$, tend to reside primarily in the most massive galaxies, while higher mass black holes reside primarily in dwarf galaxies.

lation. We will adopt the Kroupa IMF in all the results to follow. In that case, we see, for example, that number density of 30 $M\odot$ black holes is $n_{\rm bh} \sim 10^{14}$ Gpc^{-3}. If $\sim 0.1\%$ of these black holes merge over a Hubble time ($t_H \sim 10^{10}$ yrs) then we might expect a local rate of $\mathcal{R} \sim 0.001\, n_{\rm bh}/t_H \sim 10$ Gpc^{-3} yr^{-1}, which is comparable to the LIGO estimate for massive black holes based on the $\sim 30\ M\odot$ pair seen in the GW150914 event ($\mathcal{R}_{30} = 3.4^{+8.6}_{-2.8}$ Gpc^{-3} yr^{-1} Abbott et al., 2016b). In Section 4.5 we will present a more careful comparison to the inferred LIGO rates.

Figure 4.3 clearly shows that the overall black hole number density in the universe is fairly high. Whether this provides a consistent and reasonable explanation of the LIGO observations depends largely on the expected fraction of merging BBH and the merger time scale. One question of interest is how is this cosmic abundance of black holes distributed among galaxies? Figure 4.4 shows the results for various cuts on $m_{\rm bh}$. We see that most low-mass lack holes in the universe reside within massive galaxies, while higher mass black holes tend to reside in dwarfs. This general trend is expected since low-mass black holes tend to track stellar mass, and most of the stellar mass in the local universe is in massive galaxies. Massive black holes tend to reside in $M_\star \sim 10^{8-10} M\odot$ galaxies. The most likely host for a single $\sim 30 M\odot$ black hole chosen at random in the universe is a galaxy of stellar mass $M_\star \sim 10^{10} M\odot$. Of course, just because most black holes live in massive galaxies this does not necessarily imply that most black hole *mergers* will occur in massive galaxies. We will return to this question in §4.5.1.

4.4.3 Comparison to Core Collapse Supernova Rates

A useful test of our methodology is to compare the observed density of core collapse supernova (CCS) remnants to that predicted in our model. If we change the mass limits in Equation 4.1, we can calculate the global density of CCS remnants using Equation 3. For the minimum

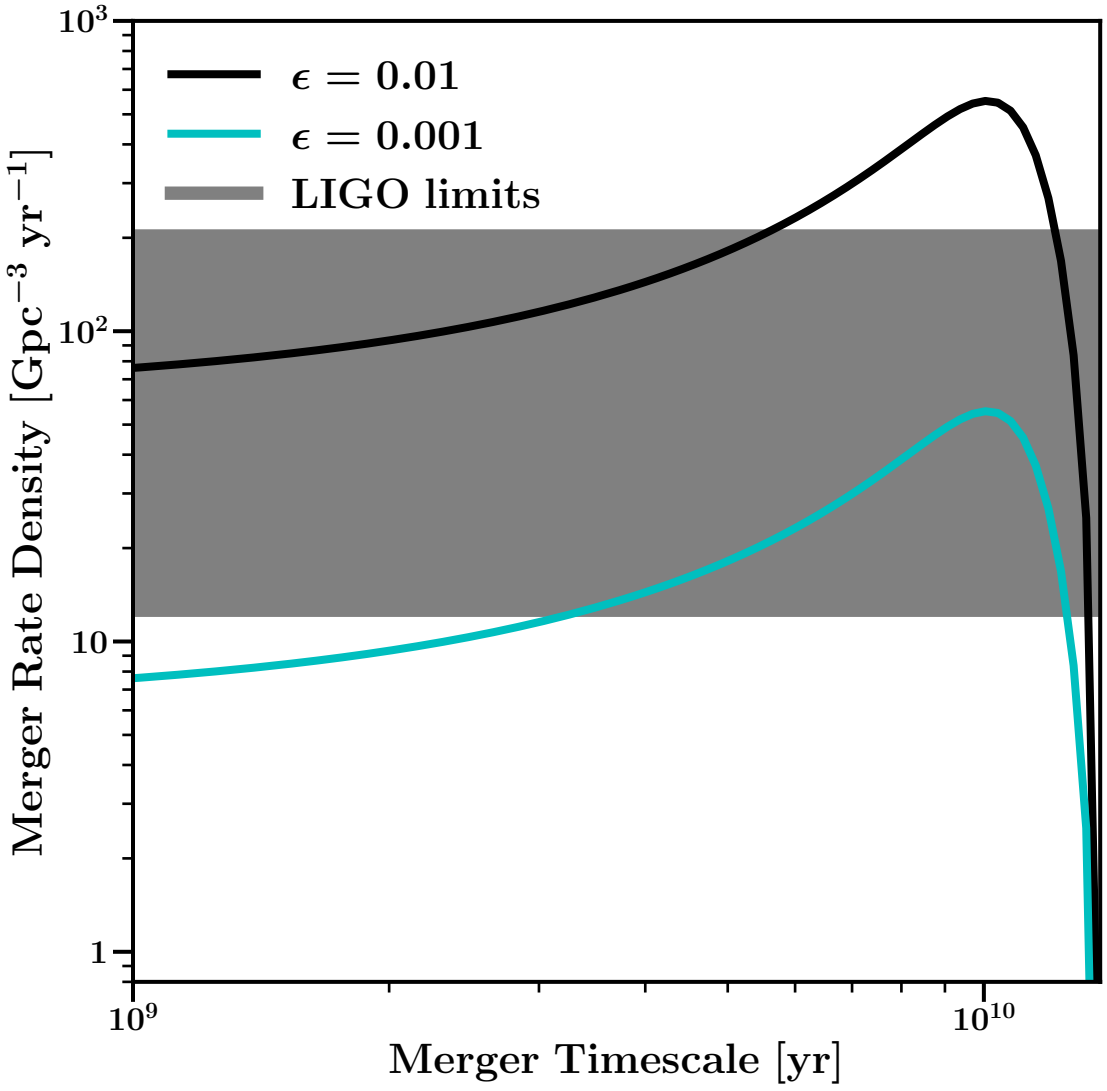

Figure 4.5: Predicted merger rate density of black holes more massive than $5M\odot$ as a function of merger timescale for various choices of binary merger efficiency fractions ϵ (see the discussion of ϵ below Equation 4). The gray band displays the measurement from (Abbott et al., 2017) for all $m_{\rm bh} > 5M\odot$ merging pairs. In order to lie within these LIGO limits, either a long ($\tau \sim 10$ Gyr) merger timescale and low $\epsilon \sim 10^{-3}$ merging fraction, or a short merger timescale and slightly larger $\epsilon \sim 10^{-2}$ merging fraction are required.

stellar mass we use 8 $M\odot$ and for the upper limit we use 18 $M\odot$, which assumes that most stars above this mass collapse to form black holes with no visible supernovae (Smartt, 2015). Doing this gives a value of roughly one CCS for every 100 solar masses of stars formed, and integrating over the stellar mass function yields a remnant density of $n_r = 2.5 \times 10^6$ Mpc^{-3}. Current measurements place the local CCS rate density at 0.7×10^{-4} yr^{-1} Mpc^{-3} (Strolger et al., 2015). If we assume the CCS rate closely tracks the star formation rate, we can normalize the evolution of the cosmic star formation rate density from Madau & Dickinson (2014) to this value and integrate over the age of the universe to find the total density of CCS remnants. This gives a density of $n_r = 3.8 \times 10^6$ Mpc^{-3}, which is within a factor of ~ 1.5 of our estimated remnant density.

4.5 Black Hole Merger Rates

In what follows we will assume that black hole mergers occur among binary pairs and that these mergers occur after the birth of the binary pair over a timescale τ. For simplicity, we will focus on merger rates for pairs of black holes each with masses above the same threshold value of $m_{\rm bh}$. The merger timescale τ is subject to several assumptions and therefore difficult to calculate from first principles (Lipunov et al., 1997; Sipior & Sigurdsson, 2002; Dominik et al., 2013; Belczynski et al., 2016a; Lamberts et al., 2016). Our approach is to treat τ as a parameter to be constrained.

At any given epoch, the number density of black hole pairs available to merge before $z = 0$ can be written in terms of the black hole number density at that time. Specifically for pairs of mass $m_1, m_2 > m_{\rm bh}$ we have

$$n_{\rm bh}^{\rm pair}(> m_{\rm bh}) = \frac{1}{2}\,\epsilon\, n_{\rm bh}(> m_{\rm bh}). \tag{4.4}$$

Here we have introduced a new parameter that we refer to as the "binary black hole efficiency": $\epsilon \equiv f_{\rm b\star} \times f_{\rm m_1/m_2} \times f_{\rm surv} \times f_{\rm t} < 1$. This dimensionless quantity parameterizes our ignorance of merging black holes from massive stars. The value $f_{\rm b\star}$ is the massive star binary fraction ($f_{\rm b\star} \sim 0.5$; e.g. Sana et al., 2012; Kobulnicky & Fryer, 2007; Pfalzner & Olczak, 2007) and $f_{\rm m_1/m_2}$ is the fraction of massive binary systems with mass ratios near unity. Current models predict $f_{\rm m_1/m_2} \sim 0.1$ for $\rm m_1/m_2 = 0.9$ (Sana et al., 2012). The fraction of those massive star binaries that survive as black hole pairs after stellar evolution is $f_{\rm surv} \sim 0.1$ (Belczynski et al., 2016a; Lamberts et al., 2016). Finally, $f_{\rm t}$ represents the fraction of binary black holes with orbital configurations that make them available to merge before the present day ($f_{\rm t} < 1$). In this work we assume ϵ is independent of mass $\rm m_1, m_2$. If it varied significantly in the $10 - 50 M\odot$ mass range, then our predictions for BBH mergers not yet observed by LIGO would be inaccurate. With these assumptions, we find below that the binary efficiency parameter values $\epsilon \simeq 0.01 - 0.001$ can reproduce the reported black hole merger rate density from LIGO using only stellar remnant black holes.

The formation rate density of black hole pairs that can merge will depend on the birthrate density of black holes: $\dot{n}_{\rm bh}^{\rm pair} = 0.5\,\epsilon\,\dot{n}_{\rm bh}$. Here, the over-dot implies differentiation with respect to time. We will assume that the black hole formation rate density tracks the observed shape of the global star formation rate (SFR) density $\psi(t)$ (with $t = t_0 = 13.7$ Gyr corresponding to the present day) such that

$$\dot{n}_{\rm bh}(> m_{\rm bh}, t) = n_{\rm bh}(> m_{\rm bh})\,\frac{\psi(t)}{\int_0^{t_0} \psi(t'){\rm d}t'}\,. \tag{4.5}$$

For $\psi(t)$ we used the parameterization of Madau & Dickinson (2014). The SFR density peaks at $z \sim 2$, corresponding to $t \simeq 3.4$ Gyr after the Big Bang and a lookback time of 10.3 Gyr.

Now let us assume that for every binary black hole pair that is born that there is an dis-

tribution of times $\mathrm{P}(\tau')$ for them to merge. In this case, the cosmic black hole merger rate density today ($t = t_0$) can be written as an integral over the black hole birth rate density:

$$\mathcal{R} = \frac{1}{2}\,\epsilon \int_0^{t_0} \dot{n}_{\rm bh}(t_0 - \tau')\,\mathrm{P}(\tau')\,\mathrm{d}\tau'\,, \tag{4.6}$$

where $\dot{n}_{\rm bh}$ is evaluated at the black hole mass of relevance for the merger rate. We note that $\mathrm{P}(\tau')$ is the *average* distribution of merger times; the full distribution depends on many other underlying factors such as the orbit of the binary system and the environment it is in.

For simplicity, we treat $\mathrm{P}(\tau')$ as a delta function centered on a characteristic timescale: $\mathrm{P}(\tau') = \delta(\tau' - \tau)$. This allows for our results to be cast in terms of two effective parameters: the merging efficiency ϵ and the characteristic timescale τ, and results in a present day BBH merger rate density given by:

$$\mathcal{R} = \frac{1}{2}\,\epsilon\,\dot{n}_{\rm bh}(t_0 - \tau)\,. \tag{4.7}$$

Note that Equations 7 and 5 imply that for a fixed value of ϵ, a merger timescale that matches the lookback time to the peak in cosmic star formation ($\tau \sim 10$ Gyr) will produce the largest local merger rate. Thus, in order to match the observed local merger rate, a case with $\tau \sim 10$ Gyr will require the smallest values of ϵ.

The rationale for this simple single-timescale approach is that it allows us to readily explore the relationships between merger timescales, the unknown binary merger efficiency, and the host galaxies of merging events. Though the assumption is clearly a major simplification, any physically-motivated τ' distribution can in principle be mapped to a delay time τ. For example, one well-motivated assumption for the merger time distribution is $\mathrm{P}(\tau') \propto 1/\tau'$ (Dominik et al., 2013). Using $\tau = 1$ Gyr yields roughly the same density, with nearly the same constraints on ϵ, as assuming $\mathrm{P}(\tau') \propto 1/\tau'$ in Equation 6. Even if underlying merger timescale distribution is multi-modal, a combination of delta-function models can be

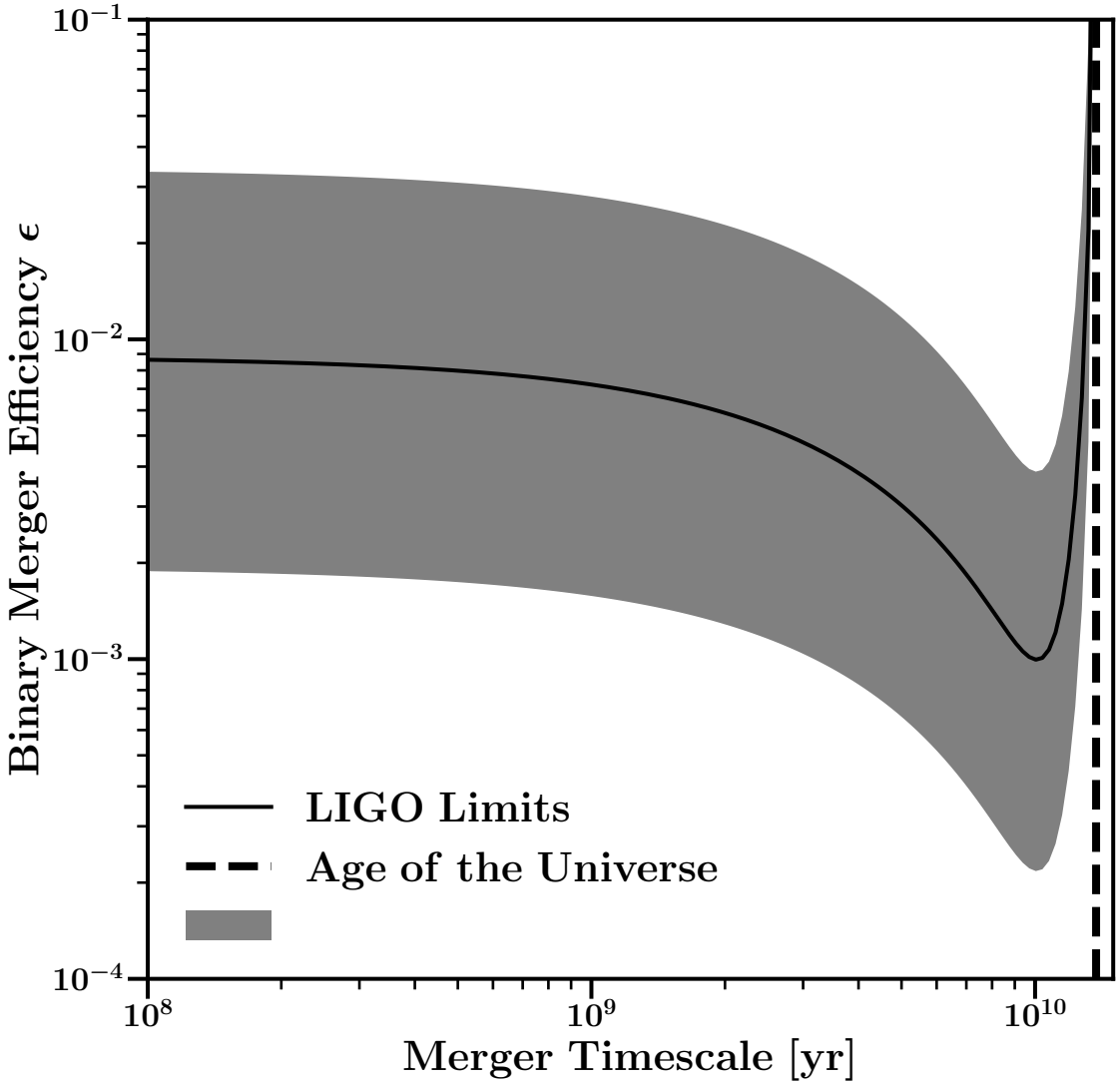

Figure 4.6: The shaded band shows the joint region of parameter space in binary efficiency ϵ and merger timescale τ that reproduces the merger rate density of black holes reported by Abbott et al. (2017) for all black hole pairs more massive than $5M\odot$.

used. For example, Belczynski et al. (2016a) and Lamberts et al. (2016), predict a bimodal distribution in birth times of massive BBH merger progenitors, with one peak at redshifts $z \sim 2$ and the other at much lower redshift, $z \sim 0.2$. In this case, a combination of delta functions, one with $\tau \sim 1$ and another with $\tau \sim 10$ Gyr reproduces such a model.

Figure 4.5 shows the predicted local merger rate of $m_{\rm bh} > 5M\odot$ black holes as a function of merger timescale τ for two choices of our binary efficiency parameter $\epsilon = 0.01$ and 0.001. The shaded band shows the total observed range from Abbott et al. (2017): $12 \leq \mathcal{R} \leq 213$. We see that for shorter timescales ($\tau \lesssim 2$ Gyr), $\epsilon = 0.01$ matches the data better. For longer timescales (close to the peak of cosmic star formation, $\tau \simeq 10$ Gyr) the lower efficiency of 0.1% is more consistent with the measurement. Note that Abbott et al. (2016b) also quote a event-based rate for binary $m_{\rm bh} \simeq 30M\odot$ mergers like GW150914 of $\mathcal{R}_{30} = 3.4^{+8.6}_{-2.8}$ Gpc^{-3} yr^{-1}. Our predicted binary merger rates for $m_{\rm bh} > 30M\odot$ black holes also agree well with their $\mathcal{R}_{30}$ range, producing curves like those in Figure 4.5 shifted down by approximately an order of magnitude, with $\epsilon = 0.01$ working better for $\tau \lesssim 2$ Gyr and $\epsilon = 0.001$ consistent for $\tau \simeq 10$ Gyr (just as in the $m_{\rm bh} > 5M\odot$ rate case).

The degeneracy between τ and ϵ values is clearer in Figure 4.6. The band shows the range of parameter values that are consistent with the reported LIGO rates for merging pairs with $m_{\rm bh} > 5M\odot$. For $\tau \lesssim 2$ Gyr, efficiencies of $\epsilon \simeq 0.002 - 0.03$ are required. The efficiencies need to be smaller if the typical merger timescale approaches the lookback time of peak star formation $\tau \simeq 10$ Gyr, $\epsilon \simeq 0.0002 - 0.004$. The sharp uptick in required efficiency as $\tau \to t_0 = 13.7$ Gyr is driven by the fact that the star formation rate drops to zero as we approach the big bang. As the merger timescale approaches age of the Universe, reproducing the observed rates requires virtually every black hole that is present in the early universe to end up merging today.

Figure 4.7 displays our predicted merger rates for black holes of various masses ($\rm m_{bh} \geq 5$, 30, and 50 $M\odot$) as a function of τ for $\epsilon = 0.01$. As previously discussed, for $\tau < 4$ Gyr, this

choice of ϵ is consistent with the reported merger rate for $> 5M\odot$ BBH mergers, though the overall amplitude of the lines is linearly proportional to ϵ. The aim of this figure is to illustrate how the rates vary with compact object mass. The $m_{\rm bh} > 30M\odot$ BBH merger rate density, for example, is lower by a factor of ~ 8 at fixed τ. The the $2-\sigma$ limit from Abbott et al. (2016b) for massive black holes of this kind is $\mathcal{R}_{30} = 0.6 - 12.4$ Gpc^{-3}yr^{-1}, which matches our predictions for this choice of ϵ as long as $\tau < 3$ Gyr (with larger τ requiring smaller ϵ as in Figure 6).

Figure 4.7 also includes neutron star-neutron star (NS-NS) merger rates, which were computed in a similar manner as our BBH merger rates. Specifically, we calculate the neutron star density assuming a minimum stellar mass for producing a NS of 8 $M\odot$ (as we did in the CCS estimate in §4.4.3), and a maximum stellar mass equal to the minimum needed to form a black hole. The upper limit on the NS-NS binary merger rate density reported in Abbott et al. (2016g) is $\mathcal{R}_{NS} < 12,600$ Gpc^{-3}yr^{-1}. The $\epsilon = 0.01$ case plotted is clearly well below this observational limit, which provides a weak constraint $\epsilon \lesssim 0.1$ for large τ and $\epsilon \lesssim 1$ for small τ. We may further check our model using the Milky Way's binary NS population and the short gamma ray burst (GRB) density. Kim et al. (2006) and Enrico Petrillo et al. (2013) estimate the binary NS merger rate should be $\mathcal{R}_{NS} \simeq 10^2 - 10^3$ Gpc^{-3}yr^{-1}, which is consistent with the predictions shown in Figure 7 for $\tau \lesssim 5$ Gyr.

Having confirmed the consistency of our model with previous theoretical explorations and observational constraints, we now predict the merger rate density for even more massive compact objects – a regime that has not yet been probed observationally. Our expected rate density for black hole binary mergers each with $m_{\rm bh} > 50M\odot$ is $\mathcal{R}_{50} \gtrsim 1\,(\epsilon/0.01)$ Gpc^{-3}yr^{-1}. With a rate density this high, we expect that a massive merger of this kind should be detected within the next decade. Mergers involving at least one black hole of this high mass should be more common.

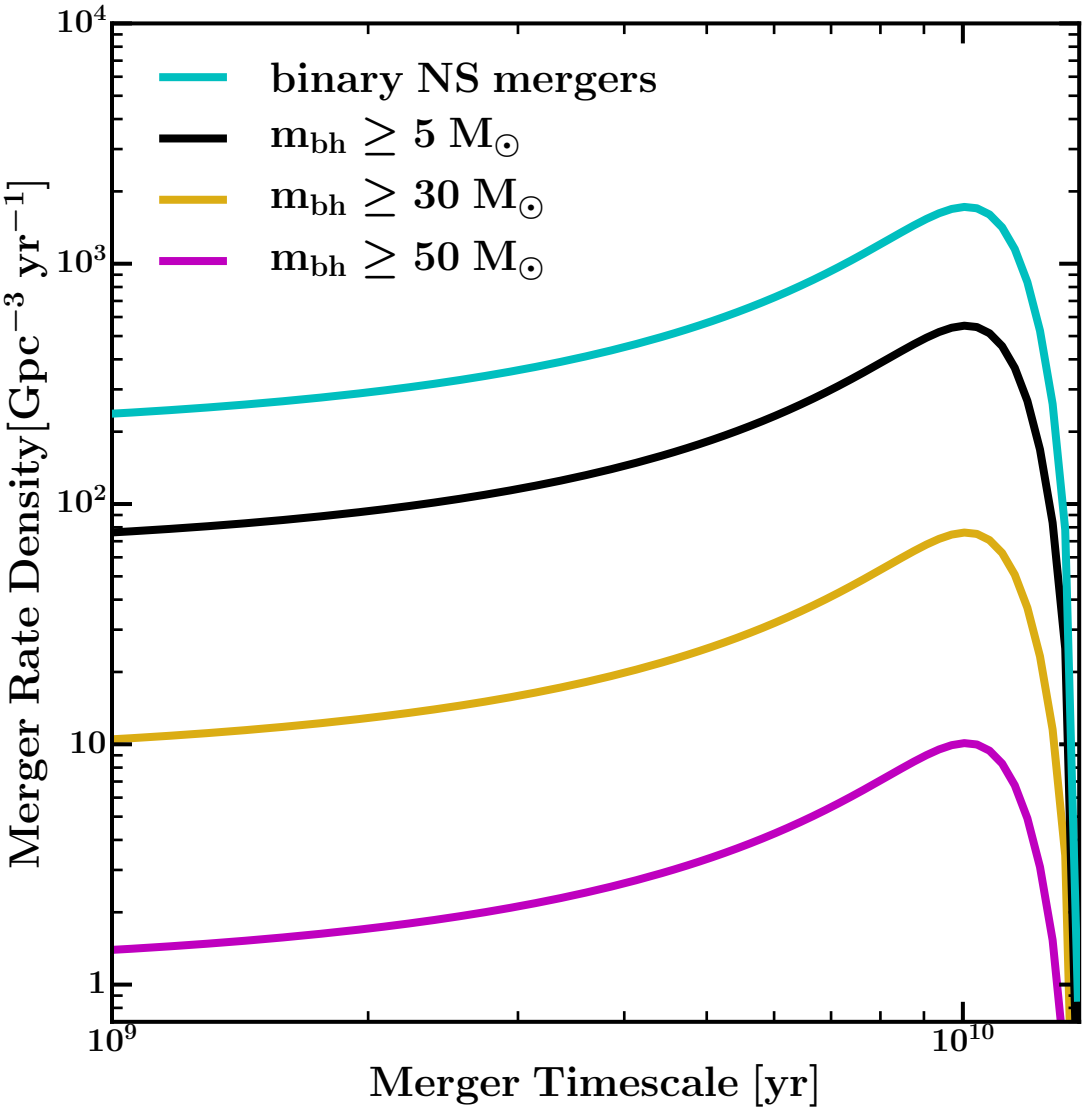

Figure 4.7: Merger rate densities for NS-NS mergers (cyan), all black hole binaries (black), black hole binaries each more massive than 30 $M\odot$ (yellow), and black hole binaries more massive than 50 $M\odot$ (magenta) as a function of characteristic merger timescale τ, assuming a binary black hole efficiency of $\epsilon = 0.01$. This value gives a binary neutron star merger rate in good agreement with other observational and theoretical constraints (Kim et al., 2006; Enrico Petrillo et al., 2013; Dominik et al., 2013) and is consistent with the BBH merger rate densities reported by Abbott et al. (2016b) for $\tau < 4$ Gyr. Note that all rates scale linearly with ϵ.

4.5.1 Breaking degeneracies with host galaxy masses

One of the goals of gravitational wave astronomy is to constrain the astrophysics that underlies black hole merger detections, including 1) the physics of black hole binary formation and 2) the processes that drive subsequent mergers. We have parameterized these two global uncertainties using two simplifying parameters: the merger timescale τ and the binary black hole efficiency ϵ. As demonstrated in Figure 4.6, current constraints on the merger rate provide only degenerate constraint on these parameters, and in particular allow a vast range of characteristic merger timescales, from fairly prompt mergers, $\tau \simeq 100$ Myr, to mergers that have taken a Hubble time to occur.

One possible way to break this degeneracy is to identify the host galaxy mass distribution for observed merger events. Small galaxies today have ongoing star formation, while larger galaxies tend to be quenched (e.g. Mannucci et al., 2010). Thus, binary mergers that occur soon after formation will more likely be seen in small galaxies. Mergers over timescales comparable to the age of the universe, however, will more closely track the overall stellar mass distribution. Most stars are in massive galaxies today (Baldry et al., 2012; Bernardi et al., 2013). Thus mergers detected locally that have take a long time to occur will be biased to reside within large galaxies.

An expanded network of gravitational wave detectors, including Advanced Virgo and the planned LIGO-India project, should be able to localize gravitational wave sources within a few square degrees (Nissanke et al., 2013; Abbott et al., 2016e). With enough detections, cross-correlating merger locations with galaxy counts on degree scales could enable constraints on the host mass for BBH mergers, as massive galaxies cluster more strongly with other galaxies than do lower mass sytems (e.g. Zehavi et al., 2012; Raccanelli et al., 2016). More precise determinations of host mass distributions would be enabled if there are electromagnetic counterparts to mergers. Unfortunately, BBH mergers are not expected

to produce significant EM radiation except in extreme cases (Loeb, 2016, e.g.), though see Perna et al. (2016) for a more plausible scenario. On the other hand, NS-NS mergers *are* expected to produce short gamma-ray bursts (e.g. Narayan et al., 1992; Rosswog et al., 2003; Nakar & Piran, 2011). The Advanced LIGO/Virgo detector network should detect tens of NS-NS mergers per year (Abadie et al., 2010), which could enable a promising avenue for mapping out the host distributions for these mergers with some precision.

In order to provide some quantitative insight into how well host masses can help discriminate models with different timescales, we consider two extreme examples: one prompt ($\tau \sim 100$ Myr) and another comparable to the Hubble time ($\tau \sim 10$ Gyr). The rate of prompt mergers will be governed by the compact object birthrate in the low-z universe, $\dot{n}_{\rm co,0} \equiv \dot{n}_{\rm co}(t \simeq t_0)$. Specifically, the merger rate for prompt mergers will be

$$\mathcal{R}_{\rm prompt} = \frac{1}{2}\,\epsilon\,\dot{n}_{\rm co,0}. \tag{4.8}$$

While Equation 4.5 can be used to provide a good estimate for $\dot{n}_{\rm co,0}$, it cannot be used to determine the host mass distribution for newly formed black holes or neutron stars. This is because Equation 4.5 is normalized by the total remnant density and contains no information on when and where those remnants were born – only where they are today.

In order to accurately determine the host mass distribution for compact objects being born recently, we can perform an analysis similar to the one we used in calculating $n_{\rm bh}$ (Equations 4.1 and 4.3). Starting with neutron star birthrates, we assume that they track massive star formation at a given gas-phase metallicity Z_g. Specifically, we need the minimum ($\mathcal{M}^{\rm ns}_{\rm min} = 8M\odot$) and maximum stellar progenitor mass that will produce a neutron star: $\mathcal{M}^{\rm ns}_{\rm max}(Z_g) = \mathcal{M}_{\rm min}(m_{\rm co}, Z)$ with $m_{\rm co} = 5M\odot$ is the same progenitor mass limit discussed in § 4.4.1. The observed mass-metallicity-SFR relation $\dot{M}_\star(M_\star, Z_g)$ (Mannucci et al., 2010; Lara-López et al., 2010) then provides a means to estimate the birth rate density by integrating over

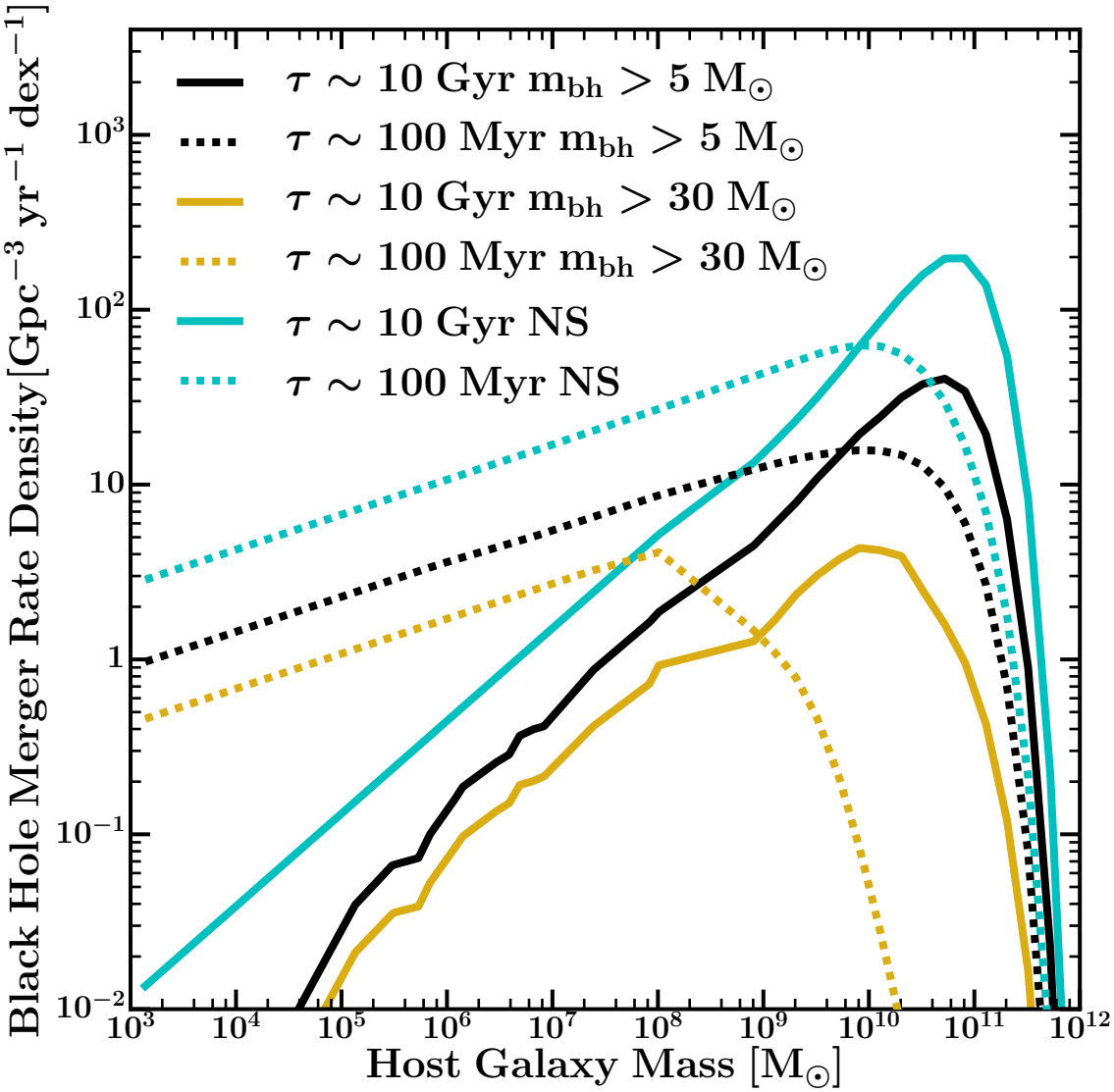

Figure 4.8: Merger rate density per dex in host galaxy stellar mass as a function of host stellar mass for NS-NS mergers (cyan), all BBH mergers (black), and for BBHs mergers of two > 30 $M\odot$ black holes (yellow). Solid lines show predictions for long merger timescales $\tau = 10$ Gyr while dotted lines show the host distribution for prompt mergers $\tau \sim 100$ Myr. Merging efficiencies have been set to $\epsilon = 0.007$ for prompt mergers and $\epsilon = 0.001$ for delayed mergers to produce the same global rate for the $m_{\rm bh} > 30M\odot$ mergers. Prompt mergers are more likely to occur in smaller galaxies because this is where the star formation is occurring today. This is especially true for the most massive BBHs owing to the fact that recent massive black hole formation is limited to galaxies with lower gas-phase metallicities.

metallicity distribution function and stellar mass function:

$$\dot{n}_{\rm ns,0} = \int_{M_{\rm min}}^{\infty} \phi(M_\star) \int \frac{\dot{M}_\star(M_\star, Z_g)}{\bar{\mathcal{M}}} \mathcal{P}(Z_g, M_\star) \int_{\mathcal{M}_{\rm min}^{\rm ns}}^{\mathcal{M}_{\rm max}^{\rm ns}} \xi(\mathcal{M}')\ d\mathcal{M}'\, {\rm d}Z_g\, {\rm dM}_\star. \tag{4.9}$$

Note that the observed gas-phase metallicity relation provides results for the oxygen abundance and we are interested in the overall metallicity. We account for this following Peeples & Somerville (2013) and use the [α/Fe]-mass relation from Thomas et al. (2005) to determine Z_g from the gas-phase oxygen abundance.

The birthrate calculation for black holes is the same as the above calculation for neutron stars except for the limits of the integral over the IMF. For black holes of mass $> m_{\rm bh}$ the lower limit is $\mathcal{M}_{\rm min}(m_{\rm bh}, Z)$ and the upper limit is $\mathcal{M}_{\rm u}$ (as defined for Equation 1).

We emphasize that both Equations 4.5 and 4.9 give almost identical answers for the global compact object birthrate rate today when Equation 4.5 is evaluated at $t = t_0$. This must be the case if $\psi(t)$ is normalized self-consistently. However, Equation 4.9 now allows us to determine the host mass distribution for newly formed objects. That is, we can differentiate Equation 4.8 with respect to galaxy stellar mass to derive the black hole merger rate density per host mass in the case that black hole mergers occur promptly after black hole binary formation.

Figure 4.8 shows the results of these calculations for binary NS-NS mergers in cyan, all BBH mergers in black, and BBH mergers with $\rm m_{bh} > 30$ M$\odot$ in yellow. Dashed lines indicate prompt mergers of compact objects formed recently ($\tau \sim 100$ Myr), derived by differentiating Equation 4.8. Solid lines indicate long-timescale mergers of objects formed at redshift $z = 2$ ($\tau \sim 10$ Gyr), derived by differentiating Equation 4.5 (and thus Equation 4.3) with respect to

stellar mass. For this figure, we have used merging efficiencies of $\epsilon = 0.007$ for prompt mergers and $\epsilon = 0.001$ for delayed mergers in order that they both produce the same global rates, specifically the mean reported LIGO rate for the overall and massive black hole populations.

The median host galaxy mass for prompt NS-NS mergers is $M_\star = 1.4 \times 10^9\ M\odot$ while for delayed mergers it is $M_\star = 3.9 \times 10^{10}\ M\odot$. The main difference between the distributions is in the low-mass tail, where prompt BBH merger rate density varies slowly with host mass as $M_\star^{1/7}$ while long timescale BBH merger rate density increases more sharply with host mass as $M_\star^{1/2}$. This is caused by the shape of the mass-metallicity-SFR relation; while the total number of black holes formed in a galaxy is largely independent of its mean stellar metallicity (4.2) below a certain threshold, the number *forming* locally depends on the specific star formation rates of the host galaxies, which changes only moderately with stellar mass at these scales (Leitner, 2012; Tomczak et al., 2016, e.g.). In the prompt scenario, this implies 47% of NS-NS mergers occur in dwarf galaxies with $M_\star < 10^9\ M\odot$ while in the delayed-merging scenario only 6% are hosted by dwarfs. Given the expected binary NS-NS detection rate for the Advanced LIGO/VIRGO network (Abadie et al., 2010) and the likelihood for electromagnetic counterpart signals, it should be possible to map out the host galaxy population in coming decade and to explore the question of whether these mergers have occurred long after formation (thus tracing stellar mass and the most massive galaxies) or promptly after formation (tracing star formation and dwarf galaxies). The LIGO India detector will only enhance the ability to perform this experiment.

The dependence of host mass distribution on merger timescale also exists for BBH mergers. For all $> 5M\odot$ BBH mergers, the median host galaxy masses are $9.5 \times 10^8\ M\odot$ and $2.6 \times 10^{10}\ M\odot$ for the short and long merger timescales, respectively. The fraction of mergers hosted by $M_\star < 10^9\ M\odot$ dwarf galaxies is 51% and 9% in the two cases. For the more massive $> 30M\odot$ "GW150914-like" mergers, 95% occur in dwarfs for the prompt case while just 24% are hosted by dwarfs in the long-timescale case.

To assess the feasibility of discriminating between the prompt and the long-timescale scenarios for BBH mergers, we can draw an analogy with the ultra-high energy cosmic rays. The origin of the ultra-high energy cosmic rays (UHECRs) with measured energies in excess of 10^{19} GeV is a mystery. The strong energy losses at these energies due to interactions with the Cosmic Microwave Background imply that the sources must lie within a Gpc. At energies above 5×10^{19} GeV, the abrupt (Greisen-Zatsepin-Kuzmin or GZK) cutoff due to the Δ^+ resonance leads to a dramatic decrease in the implied distance to the sources. The angular resolution of the measurements and the smearing due to bending in magnetic fields imply that the actual direction of the UHECR events can be reconstructed to only about 5 degrees, a situation similar to that for gravitational wave detections.

The BBH mergers are detectable to distances of a Gpc and unlike the case with the UHECRs, we expect some constraint on the source distance from the gravitational wave detections. For the UHECR case, it seems like the 69 events from the Pierre Auger Observatory is a large enough set of events to test for correlation with putative local sources (Abreu et al., 2010). No clear consensus has been reached on the origin of these UHECR events. In particular, only a fraction of the UHECRs can be attributed to the local catalogs of AGNs or 2MASS galaxies that have been cross correlated (Khanin & Mortlock, 2016). While the origin of UHECR has not been clarified by these analyses, they have demonstrated the feasibility of testing various hypotheses for the origin of UHECRs with upwards of about 50 events.

If the origin of the BBH mergers is related to stellar mass remnants, then our analogy with UHECR correlation studies suggests that looking for correlation large, clustered galaxies could be a fruitful way forward. Because the galaxy clustering bias begins to increase around masses of $M_\star \gtrsim 10^{10.7}$ at $z < 0.3$ (e.g. Zu & Mandelbaum, 2015) we use this as our mass threshold. For the long timescale scenario, our prediction is that 30% of BBH mergers with masses $> 5M\odot$ and 42% of NS mergers occur in $M_\star \gtrsim 10^{10.7}$ hosts, while the corresponding numbers for the prompt scenario are 5.4% and 4.6%. Thus, we would expect

a cross correlation with these highly biased galaxies only in the long timescale scenario (the situation for the most massive $> 30M\odot$ BBH mergers is even more stark, though less observable: 6.4% and 1.0×10^{-3}%, respectively). Testing a model that includes templates for both the red and dwarf galaxies, it may be possible to infer the relative contributions of each to the observed mergers. Given our correlated predictions for the NS-NS mergers and their possibile EM counterparts, nailing down the timescale for the mergers seems a likely possibility.

Note that in calculating our host mass distributions for long-timescale mergers we have assumed that black hole pairs that formed near the peak in cosmic star formation rate density ($z = 2$) have distributed themselves like the bulk of the black holes in the Universe today. This assumption is conservative in the sense that it biases mergers to occur in *lower mass* hosts than they otherwise would. In reality, black holes that formed at $z = 2$ will reside in slightly higher mass galaxies than the bulk of the black hole population (since half the stars formed after this time, and later star formation occurs in smaller galaxies). Given this, it is possible that the dichotomy in host mass populations for prompt and long merger timescale populations is sharper than that in Figure 4.8.

4.6 Conclusions

In this paper we have worked through empirically-derived expectations for the stellar remnant black hole population in the Universe and used these as a basis for interpreting gravitational wave signals such as those being detected by Advanced LIGO and eventually Advanced Virgo (LIGO Scientific Collaboration et al., 2015; Acernese et al., 2015). We have quantified our uncertainties using two parameters: the binary black hole efficiency ϵ (Equation 4), and the typical merger timescale τ (Equations 6 and 7).

Stellar-remnant black holes should be abundant in the local universe. For example, $m_{\rm bh} > 30M\odot$ black holes should have a local number density of $0.9 - 2 \times 10^{14}$ Gpc^{-3} with the range reflecting variations between our fiducial Kroupa (2002) and metallicity dependent (Geha et al., 2013) IMFs. This corresponds to an occupation rate of ~ 1 per 1000 $M\odot$ of stars formed in galaxies with $M_\star \lesssim 10^{10}M\odot$ (see Figures 4.2 and 4.3). Such an abundant black hole population provides an ample source for binary systems that eventually merge for reasonable choices of parameters that characterize the merger process.

If $\epsilon \simeq 1\%$ of stellar remnant black holes end up in a binary configuration that eventually merges, then the current LIGO merger rate constraints can be accommodated as long as the typical merger timescale is $\tau \lesssim 5$ Gyr (See Figure 6). If mergers tend to occur over a timescale that coincides with the peak in cosmic star formation rate density ($\tau \simeq 10$ Gyr) then the efficiency of binary mergers would need to be smaller ($\epsilon \simeq 0.1\%$) in order to be consistent with the observed rates.

Though our approach is not well suited for ab initio calculations, it does provide fairly robust scalings because the uncertain/unknown parameters are reasonably constant for all compact objects in our calculations. For example, for any ϵ or τ, 50 $M\odot$ black holes should have merger rate densities that are a factor of 7 ± 1 smaller than merger rates of binary 30 $M\odot$ black holes (see Fig. 4.7). This range accounts for uncertainties in the faint end of the stellar mass function (taken from Geller et al., 2012; Baldry et al., 2012; Lan et al., 2016). Scaling from the event-based rate derived for GW150914, we would therefore predict the rate for 50 $M\odot$ black holes binary mergers to be $\mathcal{R}_{50} = 8^{+27}_{-6}$ Gpc^{3}yr^{-1}. This places 50 $M\odot$ black hole binary mergers at the limit where detection by LIGO within the next decade should be expected. In principle, the mass specturm of detected compact objects will provide information on the galaxy SMF, as few massive detections would imply a shallow faint-end slope of $\alpha \sim -1.3$, while a large number would support slopes closer to$\alpha \sim -1.7$.

Given the degeneracy between merger timescale and binary efficiency in producing the ob-

served range of merger rates, we have explored one possible avenue for breaking this degeneracy. In Figure 8, we showed that for very short timescale "prompt" mergers, which occur soon after black hole formation, the host galaxy population is expected to track the local star formation, and therefore be skewed towards smaller galaxies. For example, about half of the BBH mergers with $m_{\rm bh} > 5M\odot$ should occur in hosts with stellar masses $< 10^9 M\odot$ in the prompt merger scenario, while only 10% of such events should be hosted by these dwarf galaxies in the long timescale scenario.

As we move towards an era where a global network of gravitational wave detectors is likely, we can expect source localization to provide a means towards discriminating scenarios of this kind. For BBH mergers with no electromagnetic counterparts, the host distribution may in principle be inferred by searching for correlation of these events with background galaxy population, in much the same way as has been attemped with ultra-high energy cosmic rays measured by the Pierre Auger Observatory (§4.1). For NS-NS mergers, we expect electromagnetic counterparts, which would be more direct way to determine the host masses. If we are able to map out the source distribution for NS-NS and BBH mergers directly through electromagnetic counterparts or indirectly through the anisotropy of source distribution, then we will be able to constrain formation and evolution scenarios for binary black hole and neutron star merger events.

Chapter Acknowledgments

Support for this work was provided by NASA through *Hubble Space Telescope* grants HST-GO-12966.003-A and HST-GO-13343.009-A. We thank A. Lamberts, S. Garrison-Kimmel and our referee for useful discussions.

Chapter 5

Summary and Conclusions

In this work we have used numerical and analytic techniques to investigate the ability of Dark Matter self-interactions to resolve current problems in galaxy evolution and to estimate the population of stellar remnant objects in the universe.

In Chapter 2 we presented a set of high resolution n-body simulations of dwarf haloes with both collisionless and self-interacting dark matter. We found that SIDM cross sections greater than 0.1 $\mathrm{cm}^2\ \mathrm{g}^{-1}$ can solve the Too Big to Fail and Core-Cusp problems, though $\sigma/m > 1\ \mathrm{cm}^2\ \mathrm{g}^{-1}$ would generate cores too sparse to host local field dwarfs. However, if the SIDM cross section is around 50 $\mathrm{cm}^2\ \mathrm{g}^{-1}$, core collapse will begin and increase the central halo density enough to again match observations.

Chapter 3 detailed our analysis of adiabatic contraction in SIDM haloes. By embedding gravitational potentials into idealized simulations of Milky Way, Elliptical, Low Surface Brightness (LSB) and Cluster host haloes we are able to reproduce the adiabatic contraction first predicted by Blumenthal et al. (1986), and investigate this process in SIDM haloes. We found that the predictions of the Kaplinghat et al. (2014a) model accurately reflect our simulations, and that contraction is stronger in SIDM haloes than in CDM haloes. For

extremely baryon dominated systems core-collapse can cause high-density cusps to emerge in SIDM haloes. For a Milky Way halo hosting a Milky Way galaxy, the dark matter density profile is nearly identical under both CDM and SIDM, and the same is true for the typical elliptical galaxy. More dark matter dominated systems, such as LSBS, however, retain large SIDM cores. This implies that the strongest constraints on SIDM cross sections can come from galaxies with high mass to light ratios. In cluster systems, in particular, we find that cross sections of $0.1 - 0.2$ cm^2 g^{-1} are best able to reproduce the observations of Newman et al. (2013a).

In Chapter 4 we combined known statistics of galaxy populations with results of the latest stellar evolution models to study the universal population of stellar remnant black holes and neutron stars. We found that a galaxy should host roughly one 30 $M\odot$ black hole for every 1000 $M\odot$ of stars formed. This leads to a universal number density of $\sim 10^{14}$ Gpc$^{-}3$, and the overall remnant black hole density is an order of magnitude higher. We then calculated merger rate densities for binary black holes (BBHs) by assuming a merging efficiency and characteristic delay time and between star formation and remnant merger. Using the BBH rate densities measured by LIGO (Abbott et al., 2016b) we then constrained the efficiency and delay times, and found that most BBH mergers occur either at high redshift in massive hosts or at low redshift in dwarf galaxies. Because of this, if hosts for BBH gravitational waves are identified it can provide strong constraints on the properties of black hole mergers.

Bibliography

Abadie J. et al., 2010, Classical and Quantum Gravity, 27, 173001

Abbott B. P. et al., 2016a, Classical and Quantum Gravity, 33, 134001

Abbott B. P. et al., 2016b, Physical Review X, 6, 041015

Abbott B. P. et al., 2016c, Physical Review Letters, 116, 241103

Abbott B. P. et al., 2016d, Physical Review Letters, 116, 061102

Abbott B. P. et al., 2016e, Living Reviews in Relativity, 19, 1

Abbott B. P. et al., 2016f, ApJ, 833, L1

Abbott B. P. et al., 2016g, ApJ, 832, L21

Abbott B. P. et al., 2017, Physical Review Letters, 118, 221101

Abreu P. et al., 2010, Astroparticle Physics, 34, 314

Acernese F. et al., 2015, Classical and Quantum Gravity, 32, 024001

Ackermann M. et al., 2017, ApJ, 840, 43

Adams J. J. et al., 2014, ApJ, 789, 63

Amorisco N. C., Bertin G., 2010, A&A, 519, A47

Amorisco N. C., Zavala J., de Boer T. J. L., 2014, ApJ, 782, L39

Anderhalden D., Schneider A., Macciò A. V., Diemand J., Bertone G., 2013, J. Cosmology Astropart. Phys., 3, 14

Arraki K. S., Klypin A., More S., Trujillo-Gomez S., 2014, MNRAS, 438, 1466

Astropy Collaboration et al., 2013, A&A, 558, A33

Auger M. W., Treu T., Bolton A. S., Gavazzi R., Koopmans L. V. E., Marshall P. J., Moustakas L. A., Burles S., 2010, ApJ, 724, 511

Balberg S., Shapiro S. L., Inagaki S., 2002, ApJ, 568, 475

Baldry I. K. et al., 2012, MNRAS, 421, 621

Behroozi P. S., Wechsler R. H., Conroy C., 2013a, ApJ, 770, 57

Behroozi P. S., Wechsler R. H., Wu H.-Y., 2013b, ApJ, 762, 109

Belczynski K., Dominik M., Bulik T., O'Shaughnessy R., Fryer C., Holz D. E., 2010, ApJ, 715, L138

Belczynski K., Holz D. E., Bulik T., O'Shaughnessy R., 2016a, Nature, 534, 512

Belczynski K., Kalogera V., Rasio F. A., Taam R. E., Zezas A., Bulik T., Maccarone T. J., Ivanova N., 2008, ApJS, 174, 223

Belczynski K., Repetto S., Holz D. E., O'Shaughnessy R., Bulik T., Berti E., Fryer C., Dominik M., 2016b, ApJ, 819, 108

Bernardi M., Meert A., Sheth R. K., Vikram V., Huertas-Company M., Mei S., Shankar F., 2013, MNRAS, 436, 697

Bird S., Cholis I., Muñoz J. B., Ali-Haïmoud Y., Kamionkowski M., Kovetz E. D., Raccanelli A., Riess A. G., 2016, Physical Review Letters, 116, 201301

Blinnikov S. I., Khlopov M. Y., 1983, Soviet Ast., 27, 371

Blumenthal G. R., Faber S. M., Flores R., Primack J. R., 1986, ApJ, 301, 27

Boddy K. K., Feng J. L., Kaplinghat M., Shadmi Y., Tait T. M. P., 2014a, arXiv: 1408.6532 [hep-ph]

Boddy K. K., Feng J. L., Kaplinghat M., Tait T. M. P., 2014b, Phys. Rev. D, 89, 115017

Boddy K. K., Kaplinghat M., Kwa A., Peter A. H. G., 2016, ArXiv e-prints

Boehm C., Schaeffer R., 2005, A&A, 438, 419

Boyarsky A., Ruchayskiy O., Iakubovskyi D., Franse J., 2014, Physical Review Letters, 113, 251301

Boylan-Kolchin M., Bullock J. S., Kaplinghat M., 2011, MNRAS, 415, L40

Boylan-Kolchin M., Bullock J. S., Kaplinghat M., 2012, MNRAS, 422, 1203

Brooks A. M., Zolotov A., 2014, ApJ, 786, 87

Bryan G. L., Norman M. L., 1998, ApJ, 495, 80

Buckley M. R., Zavala J., Cyr-Racine F.-Y., Sigurdson K., Vogelsberger M., 2014, Phys. Rev. D, 90, 043524

Bulbul E., Markevitch M., Foster A., Smith R. K., Loewenstein M., Randall S. W., 2014, ApJ, 789, 13

Burkert A., 1995, ApJ, 447, L25

Burkert A., 2000, ApJ, 534, L143

Cappellari M. et al., 2015, ApJ, 804, L21

Carr B., Kühnel F., Sandstad M., 2016, Phys. Rev. D, 94, 083504

Cautun M., Frenk C. S., van de Weygaert R., Hellwing W. A., Jones B. J. T., 2014, MNRAS, 445, 2049

Chatterjee S., Rodriguez C. L., Kalogera V., Rasio F. A., 2017, ApJ, 836, L26

Cholis I., Kovetz E. D., Ali-Haïmoud Y., Bird S., Kamionkowski M., Muñoz J. B., Raccanelli A., 2016, Phys. Rev. D, 94, 084013

Cline J. M., Liu Z., Moore G. D., Xue W., 2014, Phys. Rev. D, 90, 015023

Colín P., Avila-Reese V., Valenzuela O., Firmani C., 2002, ApJ, 581, 777

Collins M. L. M. et al., 2013, ApJ, 768, 172

Cyr-Racine F.-Y., Sigurdson K., Zavala J., Bringmann T., Vogelsberger M., Pfrommer C., 2015, ArXiv e-prints

Davé R., Spergel D. N., Steinhardt P. J., Wandelt B. D., 2001, ApJ, 547, 574

Dawson W. A. et al., 2012, ApJ, 747, L42

de Blok W. J. G., McGaugh S. S., Bosma A., Rubin V. C., 2001, ApJ, 552, L23

de Blok W. J. G., McGaugh S. S., van der Hulst J. M., 1996, MNRAS, 283, 18

de Blok W. J. G., Walter F., Brinks E., Trachternach C., Oh S.-H., Kennicutt, Jr. R. C., 2008, AJ, 136, 2648

Del Popolo A., 2012, MNRAS, 419, 971

Del Popolo A., Lima J. A. S., Fabris J. C., Rodrigues D. C., 2014, J. Cosmology Astropart. Phys., 4, 21

Di Cintio A., Brook C. B., Dutton A. A., Macciò A. V., Stinson G. S., Knebe A., 2014, MNRAS, 441, 2986

Diemand J., Kuhlen M., Madau P., Zemp M., Moore B., Potter D., Stadel J., 2008, Nature, 454, 735

Dominik M., Belczynski K., Fryer C., Holz D. E., Berti E., Bulik T., Mandel I., O'Shaughnessy R., 2013, ApJ, 779, 72

Donato F. et al., 2009, MNRAS, 397, 1169

Dooley G. A., Peter A. H. G., Vogelsberger M., Zavala J., Frebel A., 2016, MNRAS, 461, 710

Dubinski J., Carlberg R. G., 1991, ApJ, 378, 496

Dutton A. A. et al., 2016, ArXiv e-prints

Einstein A., 1916, Sitzungsberichte der Königlich Preußischen Akademie der Wissenschaften (Berlin), Seite 688-696.

Elbert O. D., Bullock J. S., Garrison-Kimmel S., Rocha M., Oñorbe J., Peter A. H. G., 2015, MNRAS, 453, 29

Ellison S. L., Patton D. R., Simard L., McConnachie A. W., 2008, ApJ, 672, L107

Enrico Petrillo C., Dietz A., Cavaglià M., 2013, ApJ, 767, 140

Epinat B. et al., 2008, MNRAS, 388, 500

Escudero M., Mena O., Vincent A. C., Wilkinson R. J., Bœhm C., 2015, J. Cosmology Astropart. Phys., 9, 034

Feng J. L., Kaplinghat M., Tu H., Yu H.-B., 2009, J. Cosmology Astropart. Phys., 7, 4

Feng J. L., Kaplinghat M., Yu H.-B., 2010a, Physical Review Letters, 104, 151301

Feng J. L., Kaplinghat M., Yu H.-B., 2010b, Phys. Rev. D, 82, 083525

Ferrero I., Abadi M. G., Navarro J. F., Sales L. V., Gurovich S., 2012, MNRAS, 425, 2817

Fiacconi D., Madau P., Potter D., Stadel J., 2016, ApJ, 824, 144

Fitts A. et al., 2016, ArXiv e-prints

Flores R. A., Primack J. R., 1994, ApJ, 427, L1

Fraternali F., Tolstoy E., Irwin M. J., Cole A. A., 2009, A&A, 499, 121

Fry A. B. et al., 2015, MNRAS, 452, 1468

Fryer C. L., Belczynski K., Wiktorowicz G., Dominik M., Kalogera V., Holz D. E., 2012, ApJ, 749, 91

Gallazzi A., Charlot S., Brinchmann J., White S. D. M., Tremonti C. A., 2005, MNRAS, 362, 41

Garrison-Kimmel S., Boylan-Kolchin M., Bullock J. S., Kirby E. N., 2014b, MNRAS, 444, 222

Garrison-Kimmel S., Boylan-Kolchin M., Bullock J. S., Lee K., 2014a, MNRAS, 438, 2578

Garrison-Kimmel S., Horiuchi S., Abazajian K. N., Bullock J. S., Kaplinghat M., 2014c, MNRAS, 444, 961

Garrison-Kimmel S., Rocha M., Boylan-Kolchin M., Bullock J. S., Lally J., 2013, MNRAS, 433, 3539

Gavazzi R., Treu T., Rhodes J. D., Koopmans L. V. E., Bolton A. S., Burles S., Massey R. J., Moustakas L. A., 2007, ApJ, 667, 176

Geha M. et al., 2013, ApJ, 771, 29

Geller M. J., Diaferio A., Kurtz M. J., Dell'Antonio I. P., Fabricant D. G., 2012, AJ, 143, 102

Gentile G., Salucci P., Klein U., Vergani D., Kalberla P., 2004, MNRAS, 351, 903

Gnedin O. Y., Kravtsov A. V., Klypin A. A., Nagai D., 2004, ApJ, 616, 16

Gnedin O. Y., Ostriker J. P., 2001, ApJ, 561, 61

Governato F. et al., 2012, MNRAS, 422, 1231

Graves G. J., Faber S. M., Schiavon R. P., 2009, ApJ, 698, 1590

Griest K., 1988, Phys. Rev. D, 38, 2357

Gritschneder M., Lin D. N. C., 2013, ApJ, 765, 38

Hahn O., Abel T., 2011, MNRAS, 415, 2101

Hernquist L., 1990, ApJ, 356, 359

Hinshaw G. et al., 2013, ApJS, 208, 19

Hoffman G. L., Salpeter E. E., Farhat B., Roos T., Williams H., Helou G., 1996, ApJS, 105, 269

Horiuchi S., Humphrey P. J., Oñorbe J., Abazajian K. N., Kaplinghat M., Garrison-Kimmel S., 2014, Phys. Rev. D, 89, 025017

Hunter J. D., 2007, Computing In Science & Engineering, 9, 90

Inomata K., Kawasaki M., Mukaida K., Tada Y., Yanagida T. T., 2016, ArXiv e-prints

Jesseit R., Naab T., Burkert A., 2002, ApJ, 571, L89

Jones E., Oliphant T., Peterson P., et al., 2001–, SciPy: Open source scientific tools for Python. [Online; accessed 2016-05-19]

Jungman G., Kamionkowski M., Griest K., 1996, Phys. Rep., 267, 195

Kahlhoefer F., Schmidt-Hoberg K., Frandsen M. T., Sarkar S., 2014, MNRAS, 437, 2865

Kaplinghat M., Keeley R. E., Linden T., Yu H.-B., 2014a, Physical Review Letters, 113, 021302

Kaplinghat M., Tulin S., Yu H.-B., 2014b, Phys. Rev. D, 89, 035009

Kaplinghat M., Tulin S., Yu H.-B., 2015, ArXiv e-prints

Katz H., Lelli F., McGaugh S. S., Di Cintio A., Brook C. B., Schombert J. M., 2016, ArXiv e-prints

Katz N., White S. D. M., 1993, ApJ, 412, 455

Khanin A., Mortlock D. J., 2016, MNRAS, 460, 2765

Khlopov M. Y., Mayorov A. G., Soldatov E. Y., 2010, International Journal of Modern Physics D, 19, 1385

Kim C., Kalogera V., Lorimer D. R., 2006, ArXiv Astrophysics e-prints

Kim S. Y., Peter A. H. G., Wittman D., 2016, ArXiv e-prints

Kimpson T. O., Spera M., Mapelli M., Ziosi B. M., 2016, MNRAS

Kirby E. N., Bullock J. S., Boylan-Kolchin M., Kaplinghat M., Cohen J. G., 2014, MNRAS, 439, 1015

Kirby E. N., Cohen J. G., Guhathakurta P., Cheng L., Bullock J. S., Gallazzi A., 2013, ApJ, 779, 102

Klypin A., Karachentsev I., Makarov D., Nasonova O., 2014, arXiv: 1405.4523 [astro-ph]

Kobulnicky H. A., Fryer C. L., 2007, ApJ, 670, 747

Koch A., Kleyna J. T., Wilkinson M. I., Grebel E. K., Gilmore G. F., Evans N. W., Wyse R. F. G., Harbeck D. R., 2007, AJ, 134, 566

Kochanek C. S., White M., 2000, ApJ, 543, 514

Koda J., Shapiro P. R., 2011, MNRAS, 415, 1125

Komatsu E. et al., 2011, ApJS, 192, 18

Kozai Y., 1962, AJ, 67, 591

Kroupa P., 2002, Science, 295, 82

Kushnir D., Zaldarriaga M., Kollmeier J. A., Waldman R., 2016, MNRAS, 462, 844

Kuzio de Naray R., McGaugh S. S., de Blok W. J. G., 2008, ApJ, 676, 920

Lamberts A., Garrison-Kimmel S., Clausen D., Hopkins P., 2016, ArXiv e-prints

Lan T.-W., Ménard B., Mo H., 2016, MNRAS, 459, 3998

Lara-López M. A. et al., 2010, A&A, 521, L53

Leaman R. et al., 2012, ApJ, 750, 33

Leitner S. N., 2012, ApJ, 745, 149

Lesgourgues J., Marques-Tavares G., Schmaltz M., 2016, J. Cosmology Astropart. Phys., 2, 037

Lidov M. L., 1962, Planet. Space Sci., 9, 719

LIGO Scientific Collaboration et al., 2015, Classical and Quantum Gravity, 32, 074001

Lipunov V. M., Postnov K. A., Prokhorov M. E., 1997, MNRAS, 288, 245

Loeb A., 2016, ApJ, 819, L21

Loeb A., Weiner N., 2011, Physical Review Letters, 106, 171302

Lovell M. R., Frenk C. S., Eke V. R., Jenkins A., Gao L., Theuns T., 2014, MNRAS, 439, 300

Madau P., Dickinson M., 2014, ARA&A, 52, 415

Mangano G., Melchiorri A., Serra P., Cooray A., Kamionkowski M., 2006, Phys. Rev. D, 74, 043517

Mannucci F., Cresci G., Maiolino R., Marconi A., Gnerucci A., 2010, MNRAS, 408, 2115

Markevitch M., Gonzalez A. H., Clowe D., Vikhlinin A., Forman W., Jones C., Murray S., Tucker W., 2004, ApJ, 606, 819

Martizzi D., Teyssier R., Moore B., 2013, MNRAS, 432, 1947

Massey R. et al., 2015, MNRAS, 449, 3393

Mateo M., Olszewski E. W., Walker M. G., 2008, ApJ, 675, 201

Maxwell A. J., Wadsley J., Couchman H. M. P., 2015, ApJ, 806, 229

Mediavilla E., Jiménez-Vicente J., Muñoz J. A., Vives-Arias H., Calderón-Infante J., 2017, ApJ, 836, L18

Miralda-Escudé J., 2002, ApJ, 564, 60

Miyamoto M., Nagai R., 1975, PASJ, 27, 533

Moore B., 1994, Nature, 370, 629

Muñoz R. R. et al., 2005, ApJ, 631, L137

Nakar E., Piran T., 2011, Nature, 478, 82

Narayan R., Paczynski B., Piran T., 1992, ApJ, 395, L83

Navarro J. F., Eke V. R., Frenk C. S., 1996, MNRAS, 283, L72

Navarro J. F., Frenk C. S., White S. D. M., 1997, ApJ, 490, 493

Newman A. B., Treu T., Ellis R. S., Sand D. J., 2013a, ApJ, 765, 25

Newman A. B., Treu T., Ellis R. S., Sand D. J., Nipoti C., Richard J., Jullo E., 2013b, ApJ, 765, 24

Nissanke S., Kasliwal M., Georgieva A., 2013, ApJ, 767, 124

Oñorbe J., Boylan-Kolchin M., Bullock J. S., Hopkins P. F., Kereš D., Faucher-Giguère C.-A., Quataert E., Murray N., 2015, MNRAS, 454, 2092

Oñorbe J., Garrison-Kimmel S., Maller A. H., Bullock J. S., Rocha M., Hahn O., 2014, MNRAS, 437, 1894

Oh S.-H., de Blok W. J. G., Brinks E., Walter F., Kennicutt, Jr. R. C., 2011, AJ, 141, 193

Oh S.-H., de Blok W. J. G., Walter F., Brinks E., Kennicutt, Jr. R. C., 2008, AJ, 136, 2761

Pace A. B., 2016, ArXiv e-prints

Papastergis E., Giovanelli R., Haynes M. P., Shankar F., 2014, arXiv: 1407.4665 [astro-ph]

Peñarrubia J., Benson A. J., Walker M. G., Gilmore G., McConnachie A. W., Mayer L., 2010, MNRAS, 406, 1290

Peñarrubia J., Pontzen A., Walker M. G., Koposov S. E., 2012, ApJ, 759, L42

Peeples M. S., Somerville R. S., 2013, MNRAS, 428, 1766

Perez F., Granger B. E., 2007, Computing in Science Engineering, 9, 21

Perna R., Lazzati D., Giacomazzo B., 2016, ApJ, 821, L18

Peter A. H. G., Rocha M., Bullock J. S., Kaplinghat M., 2013, MNRAS, 430, 105

Pfalzner S., Olczak C., 2007, A&A, 475, 875

Planck Collaboration et al., 2014, A&A, 571, A16

Planck Collaboration et al., 2015, ArXiv e-prints

Polisensky E., Ricotti M., 2014, MNRAS, 437, 2922

Pontzen A., Governato F., 2012, MNRAS, 421, 3464

Portail M., Gerhard O., Wegg C., Ness M., 2016, ArXiv e-prints

Postnov K. A., Yungelson L. R., 2014, Living Reviews in Relativity, 17

Power C., Navarro J. F., Jenkins A., Frenk C. S., White S. D. M., Springel V., Stadel J., Quinn T., 2003, MNRAS, 338, 14

Purcell C. W., Zentner A. R., 2012, J. Cosmology Astropart. Phys., 12, 7

Raccanelli A., Kovetz E. D., Bird S., Cholis I., Muñoz J. B., 2016, Phys. Rev. D, 94, 023516

Randall S. W., Markevitch M., Clowe D., Gonzalez A. H., Bradač M., 2008, ApJ, 679, 1173

Read J. I., Agertz O., Collins M. L. M., 2016, MNRAS, 459, 2573

Read J. I., Gilmore G., 2005, MNRAS, 356, 107

Read J. I., Wilkinson M. I., Evans N. W., Gilmore G., Kleyna J. T., 2006, MNRAS, 367, 387

Reid B. A. et al., 2010, MNRAS, 404, 60

Reyes R., Mandelbaum R., Gunn J. E., Pizagno J., Lackner C. N., 2011, MNRAS, 417, 2347

Robertson A., Massey R., Eke V., 2016, ArXiv e-prints

Robles V., Bullock J. S., Garrison-Kimmel S., Elbert O., in prep

Rocha M., Peter A. H. G., Bullock J. S., Kaplinghat M., Garrison-Kimmel S., Oñorbe J., Moustakas L. A., 2013, MNRAS, 430, 81

Rodríguez-Puebla A., Avila-Reese V., Drory N., 2013, ApJ, 773, 172

Rodríguez-Torres S. A. et al., 2016, MNRAS, 460, 1173

Rosswog S., Ramirez-Ruiz E., Davies M. B., 2003, MNRAS, 345, 1077

Ryden B. S., Gunn J. E., 1987, ApJ, 318, 15

Salucci P., Burkert A., 2000, ApJ, 537, L9

Sana H. et al., 2012, Science, 337, 444

Schaller M., Robertson A., Massey R., Bower R. G., Eke V. R., 2015, MNRAS, 453, L58

Silsbee K., Tremaine S., 2016, ArXiv e-prints

Simon J. D., Bolatto A. D., Leroy A., Blitz L., Gates E. L., 2005, ApJ, 621, 757

Simon J. D., Geha M., 2007, ApJ, 670, 313

Sipior M. S., Sigurdsson S., 2002, ApJ, 572, 962

Smartt S. J., 2015, Publications of the Astronomical Society of Australia, 32, e016

Spekkens K., Giovanelli R., Haynes M. P., 2005, AJ, 129, 2119

Spera M., Mapelli M., Bressan A., 2015, MNRAS, 451, 4086

Spergel D. N., Steinhardt P. J., 2000, Physical Review Letters, 84, 3760

Springel V., 2005, MNRAS, 364, 1105

Springel V., Frenk C. S., White S. D. M., 2006, Nature, 440, 1137

Springel V. et al., 2008, MNRAS, 391, 1685

Steigman G., Turner M. S., 1985, Nuclear Physics B, 253, 375

Strigari L. E., Bullock J. S., Kaplinghat M., Simon J. D., Geha M., Willman B., Walker M. G., 2008, Nature, 454, 1096

Strigari L. E., Frenk C. S., White S. D. M., 2014, arXiv: 1406.6079 [astro-ph]

Strolger L.-G. et al., 2015, ApJ, 813, 93

Swaters R. A., Madore B. F., van den Bosch F. C., Balcells M., 2003, ApJ, 583, 732

Thomas D., Maraston C., Bender R., Mendes de Oliveira C., 2005, ApJ, 621, 673

Tisserand P. et al., 2007, A&A, 469, 387

Tollerud E. J., Boylan-Kolchin M., Bullock J. S., 2014, MNRAS, 440, 3511

Tomczak A. R. et al., 2016, ApJ, 817, 118

Tulin S., Yu H.-B., Zurek K. M., 2013a, Phys. Rev. D, 87, 115007

Tulin S., Yu H.-B., Zurek K. M., 2013b, Physical Review Letters, 110, 111301

van der Walt S., Colbert S. C., Varoquaux G., 2011, Computing in Science Engineering, 13, 22

VanLandingham J. H., Miller M. C., Hamilton D. P., Richardson D. C., 2016, ApJ, 828, 77

Vogelsberger M., Zavala J., 2013, MNRAS, 430, 1722

Vogelsberger M., Zavala J., Loeb A., 2012, MNRAS, 423, 3740

Vogelsberger M., Zavala J., Simpson C., Jenkins A., 2014, MNRAS, 444, 3684

Walker M. G., Mateo M., Olszewski E. W., 2009, AJ, 137, 3100

Walker M. G., Peñarrubia J., 2011, ApJ, 742, 20

Wang J., Frenk C. S., Navarro J. F., Gao L., Sawala T., 2012, MNRAS, 424, 2715

Weiner B. J. et al., 2006, ApJ, 653, 1027

White S. D. M., Rees M. J., 1978, MNRAS, 183, 341

Wolf J., Martinez G. D., Bullock J. S., Kaplinghat M., Geha M., Muñoz R. R., Simon J. D., Avedo F. F., 2010, MNRAS, 406, 1220

Yoshida N., Springel V., White S. D. M., Tormen G., 2000, ApJ, 544, L87

Zavala J., Vogelsberger M., Walker M. G., 2013, MNRAS, 431, L20

Zehavi I., Patiri S., Zheng Z., 2012, ApJ, 746, 145

Zentner A. R., Bullock J. S., 2002, Phys. Rev. D, 66, 043003

Zolotov A. et al., 2012, ApJ, 761, 71

Zu Y., Mandelbaum R., 2015, MNRAS, 454, 1161